



Design and fabrication of photonic crystal nanolasers

Mathiesen, Kristoffer Skaftved

Publication date:
2020

Document Version
Publisher's PDF, also known as Version of record

[Link back to DTU Orbit](#)

Citation (APA):
Mathiesen, K. S. (2020). *Design and fabrication of photonic crystal nanolasers*. Technical University of Denmark.

General rights

Copyright and moral rights for the publications made accessible in the public portal are retained by the authors and/or other copyright owners and it is a condition of accessing publications that users recognise and abide by the legal requirements associated with these rights.

- Users may download and print one copy of any publication from the public portal for the purpose of private study or research.
- You may not further distribute the material or use it for any profit-making activity or commercial gain
- You may freely distribute the URL identifying the publication in the public portal

If you believe that this document breaches copyright please contact us providing details, and we will remove access to the work immediately and investigate your claim.

TECHNICAL UNIVERSITY OF DENMARK

PHD THESIS

Design and fabrication of photonic crystal nanolasers

Author:

Kristoffer S. MATHIESEN

Supervisor:

Prof. Jesper MØRK
Prof. Kresten YVIND
Postdoc Yi YU

*A thesis submitted in fulfillment of the requirements
for the degree of Doctor of Philosophy
in the*

Quantum and Laser Photonics Group
DTU Fotonik

March 19, 2020

Abstract

This thesis focuses on the design and fabrication of photonic crystal lasers and passive photonic crystal cavities to improve their efficiency and enhance the understanding of such nanoscale devices. The photonic crystal cavities are fabricated in an InP membrane and the lasers have embedded InAs quantum dots or InGaAsP/ InAlGaAs quantum well gain materials. The laser threshold is investigated experimentally for devices with a systematic design variation to optimize the cavity quality factor. The penetration depth into the mirror and the mirror phase change at the photonic crystal cavity end is numerically investigated for devices with systematic design variations using an equivalent Fabry-Perot model. The mirror phase is found to primarily be dependent on the change in resonance wavelength due to the design variations, while the penetration depth is found to increase as the Q-factor is increased due to gentler confinement of the cavity fields.

Photonic crystal devices with a buried heterostructure gain medium are investigated experimentally for two different devices; a standard line defect laser and the Fano laser. In the Fano laser, one mirror is a standard termination of a line defect waveguide, while the other mirror is formed due to the interference between a discrete nanocavity mode and the continuum of modes in an open waveguide. Numerical FDTD investigations are also carried out on equivalent cavities and open photonic crystal waveguides with buried heterostructures of varying lengths. The addition of the buried heterostructure to the line defect laser cavity redshifts the cavity resonance above the bandgap of the surrounding photonic crystal. Initial investigations confirm that confining the gain material to the line defect and waveguide area of the Fano lasers eliminates the self-pulsing, previously observed in samples with active material in the nanocavity, thus enabling continuous-wave operation.

The photonic crystal nanolasers promise exciting future opportunities with experimental realizations of novel device designs of ultra-compact lasers with very low energy consumption enabling optical interconnects on the chip-scale.

Resume

Denne afhandling fokuserer på design og fabrikation af fotoniske krystallaser og kaviteter i passive fotoniske krystaller for at forbedre deres effektivitet samt for at forbedre forståelsen af disse nanoskala komponenter. De fotoniske krystaller fremstilles i en InP-membran, og laserne har InAs kvantepunkter eller InGaAsP/InAlGaAs kvantebrønde i membranen. Lasertærsklen undersøges eksperimentelt for komponenter med en systematisk designvariation for at optimere kavitets kvalitetsfaktor. Penetrationsdybden ind i spejlet og spejlfaseændringen ved den fotoniske krystalkavitets ender undersøges numerisk for komponenter med systematiske designvariationer ved anvendelse af en ækvivalent Fabry-Perot-model. Spejlfasen viser sig primært at være afhængig af ændringen i resonansbølgelængde på grund af designvariationerne, mens penetrationsdybden viser sig at stige efterhånden som Q-faktoren øges på grund af mildere indeslutning af kavitetsfelterne.

Fotoniske krystal komponenter med et nedgravet heterostrukturförstærkningsmedium undersøges eksperimentelt for to forskellige komponenter; en linjedefekt laser og Fano-laser. I Fano-laseren er det ene spejl en afslutning på en linjedefektbølgeleder, mens det andet spejl dannes ved interferensen mellem en diskret tilstand i nanokaviteten og kontinuummet i tilstande i en åben bølgeleder. Numeriske FDTD-undersøgelser udføres også på ækvivalente kaviteter og åbne fotoniske krystal bølgeledere med nedgravede heterostrukturer. Den nedgravede heterostruktur i linjedefekt laserne flytter kavitetsresonansen over den omgivende fotoniske krystals båndgab. Indledende undersøgelser med förstærkningsmaterialet begrænset til linjedefekt kaviteten og bølgelederområdet i Fano-laserne viser den selvpulsering, der tidligere blev observeret i prøver med aktivt materiale i nanokaviteten kan elimineres, hvilket muliggør kontinuerlig lasing.

Fotoniske krystal nanolasere har spændende fremtidsaspekter hvor eksperimentel realisering af nye designs af ultrakompakte lasere med meget lavt energiforbrug, kan muliggøre optiske inter-connects på chip-skala.

Publications

- J. Mørk, Y. Yu, D. A. Bekele, **K. S. Mathiesen**, T. S. Rasmussen, A. Rasoulzadeh., E. Semenova, L. Ottaviano, A. Sakanas, K. Yvind, *Lasers, switches and non-reciprocal elements based on photonic crystal Fano resonances*, Proceedings of the 17th International Conference on Numerical Simulation of Optoelectronic Devices (NUSOD), IEEE, 2017. pp. 1-2.
- J. Mørk, Y. Yu, D. A. Bekele, **K. S. Mathiesen**, T. S. Rasmussen, E. Semenova, L. Ottaviano, A. Sakanas, K. Yvind, *Photonic crystal Fano lasers and Fano switches*, Proceedings of the 22nd Microoptics Conference (MOC2017), IEEE, pp. 88-89. [E-1 (Invited)].
- **K. S. Mathiesen**, T. S. Rasmussen, Y. Yu, A. Sakanas, E. Semenova, K. Yvind, J. Mørk. *Optimization of the threshold pump power of a photonic crystal nanolaser, experiment and theory*, Proc. SPIE 11031, Integrated Optics: Design, Devices, Systems, and Applications V, 110310G (26 April 2019).
- A. Sakanas, **K. S. Mathiesen**, Y. Yu, E. Semenova, L. Ottaviano, J. Mørk, K. Yvind, *Threshold power investigations of optically-pumped photonic crystal lasers with buried heterostructure gain regions*, 2019 Conference on Lasers and Electro-Optics Europe, OSA Technical Digest (Optical Society of America, 2019), paper cb_1_2.
- **K. S. Mathiesen**, A. Sakanas, E. Semenova, K. Yvind, J. Mørk, *Systematically Varying the Active Material Volume in a Photonic Crystal Nanolaser*, 2019 Conference on Lasers and Electro-Optics Europe, OSA Technical Digest (Optical Society of America, 2019), paper cb_p_20.
- **K. S. Mathiesen**, T. S. Rasmussen, A. Sakanas, E. Dimopoulos, Y. Yu, E. Semenova, K. Yvind, J. Mørk, *Optimization of the laser threshold, mirror phase and penetration depth of a photonic crystal nanolaser*, In preparation.

- **K. S. Mathiesen**, A. Sakanas, Y. Yu, E. Semenova, K. Yvind, J. Mørk, *Experimental demonstration of a pure continuous wave photonic crystal Fano laser with a buried heterostructure*, In preparation.

Acknowledgements

Several people made this work possible and I wish to give thanks. First and foremost, I am grateful to my main supervisor Jesper Mørk, who entrusted me with the project and provided guidance throughout the project. It was immensely helpful that your door was always open. I would also like to thank you for keeping a high academic standard, which ultimately drove the success of the project. I would also like to express gratitude to my co-supervisors Kresten Yvind for the continual advice and discussion on all things fabrication and characterization related, and Yi Yu for teaching me the device process flow, assisting in device design and countless fruitful discussions. You were always ready to share your knowledge, and your support and encouragement are highly appreciated. I would also like to thank Thorsten Rasmussen for all your help with simulations, and the subsequent discussions on the results. It was very helpful to me! A big thanks go to Aurimas Sakanas for your assistance in the cleanroom and discussions whenever we encountered unexpected problems. Without Aurimas Sakanas and Elizaveta Semenova growing the gain material, the photonic crystal devices would remain very passive. I would also like to thank the rest of the NATEC Hero device team, Dagmawi Bekele, Andrey Marchevsky, and Evangelos Dimopoulos for your fruitful discussion on device design, and countless hours spent on the HERO mask and our HERO lunches. I look forward to the first electrically pumped photonic crystal laser demonstration from DTU Fotonik.

My thanks also go to office mates and the rest of the *Quantum and Laser Photonics group*, coworkers showing up for football early Friday mornings and everyone at DTU Fotonik I met along the way who all contributed to a great working environment, making my time at DTU memorable.

Finally, I am immensely grateful for the continuing support of my girlfriend, Alexandra. Your patience with me has been unending! You made me realize how there is more to life than physics, and could always cheer me up after long days in the lab or cleanroom.

This work was carried out at DTU Fotonik, financially supported by the Villum Fonden via the NATEC (Nanophotonics for Terabit Communications) Centre of Excellence.

Contents

Abstract	iii
Resume	v
Publications	vii
Acknowledgements	ix
1 Introduction	1
1.1 An energy perspective	1
1.2 Nanolasers for on-chip interconnects	4
1.3 Photonic crystal lasers	9
1.3.1 Photonic crystals	9
Line defect waveguide	12
Line defect cavity	12
Double heterostructure cavity	13
Fano cavity	14
1.3.2 Gain media	15
1.4 Overview of the thesis	16
2 Devices: their fabrication and basic characterization	19
2.1 Fabrication process overview	20
2.2 Hole sizes and shape	27
2.3 Buried oxide thickness and PL spectra	30
2.4 Laser characterization setup	34
2.4.1 Experimentally determining the threshold pump power	38
2.4.2 Radio frequency measurements of self-pulsing . .	39
2.5 Setup for measuring the Q-factor	41

3	Modelling photonic crystal nanolasers	45
3.1	A rate equation model	45
3.1.1	Linear or logarithmic gain model	47
	Steady state solutions	50
3.1.2	The threshold pump power	52
3.1.3	Bounding parameters to reasonable ranges	53
3.2	FDTD simulations of passive cavities	53
4	Lowering the laser threshold by optimising the Q-factor	61
4.1	Increasing the Q-factor by shifting holes	62
4.2	Device overview	63
4.3	Experimental Characterization	65
4.3.1	Threshold powers	65
4.3.2	Maximum output power	69
4.3.3	Measured Q-factors	74
4.4	Mirror phase calculations	75
4.5	Summary and outlook	80
5	Buried Heterostructure Line Defect Devices	85
5.1	Varying the active region in a photonic crystal cavity laser	86
5.2	Device overview	89
5.3	Experimental Characterization	91
5.4	Simulations of buried heterostructure devices	93
5.4.1	Effective medium theory for the buried heterostructure	94
5.4.2	Open photonic crystal waveguide	95
5.4.3	Line defect cavities	101
5.5	Summary and outlook	103
6	Buried Heterostructure Fano Devices	107
6.1	Confining the gain region to the waveguide of a Fano cavity	110
6.2	Device overview	111
6.3	Experimental Characterization	114
6.4	FDTD investigation of buried heterostructure devices	120
6.5	Summary and outlook	123
7	Conclusion and outlook	127

A Device fabrication process flow	135
B Automated analysis of hole sizes from SEM images	145
C Laser rate equations based automated fitting tool	149
D More simulation results on photonic crystals with embedded BH	157
D.1 Transmission through a waveguide with embedded BD .	157
D.2 BH in a waveguide excited with dipoles	159
D.3 L7 cavity with embedded BH	161
Bibliography	167

CHAPTER 1

INTRODUCTION

Since the very first message was sent on the predecessor to the internet, ARPANET, on October 29, 1969¹ many incredible advancements have enabled the internet we know and use today. The importance of micro-electronic advancement cannot be overstated. Without the continuing miniaturization of the logic components, computers might still occupy entire rooms. Equally important is the ability to transmit the data between individual computers, often over incredible distances. The switch from transmission using electrons through electric wires to photons through optical fibers has already taken place for medium and long distances, and in the near future is expected to also happen on the inter-chip, and on-chip communication scale [1–3]. To do this, an appropriate light source on the size scale of the chips must first be technologically mature. This work is about the light sources for such on-chip applications; this work is about nanophotonics!

1.1 An energy perspective

To understand the need for optical interconnects, first consider the energy consumption in individual processors. Famously, Gordon Moore predicted in 1965 [4] how the number of transistors doubles every 18 to 24 months². Until recently, the name of the game, when increasing the speeds of all devices and systems in communication was down

¹The message "LOGIN" crashed the network, and only the first two letters were received. An hour and a reboot later, the full message was successfully received.

²Moore's original prediction was based on how "*complexity for minimum component cost*" [4] followed a doubling of the integrated density of components every year. Thus cost optimization is always the deciding factor.

to shrinking component sizes and increasing clock speeds. Shrinking the components in size decrease the energy consumption per bit for logic operations [5], and allowed denser integration of transistors. The increase in transistor count is continuing to this day. However, the future scaling in silicon is eventually restrained as quantum effects come into play for the smaller technologies [6]. Furthermore, increasing the clock speed also increases the generated heat, which became a limiting factor in the early 2000s. As a result, clock speeds of the central processing units, CPUs, has not significantly increased since 2004³. Instead, the increase in complexity comes from using multiple cores.

Essentially, as the components decrease in size, the energy consumption and heat generated in the transmission of bits through electrical wires increase. Thus, shrinking the components further shifts the primary source of energy dissipation from the logic operations to the electrical interconnects. One estimate by Magen et al. [7] finds the energy consumption of electrical interconnects at more than 50% of the dynamic power consumption in a power-efficient microprocessor at the 130 nm technology node. The technology nodes are industry standards that were scheduled by the International Technology for Semiconductor Roadmap, ITRS, all the way up to the 2 nm node scheduled for commercial use in 2030 [8]. This international collaboration between semiconductor manufacturers is what has primarily made Moores' law a self-fulfilling prophecy [9]. Even so, the ITRS realized the fundamental limitations of the current semiconductor technology, and that continuous shrinking could not solve future challenges. This realization led to a reorganization into the International Roadmap for Devices and Systems, ITRD, in recognition that to overcome the future challenges would require a broader approach. The ITRD continues the proposal of future technological nodes up to the 1 nm node in 2033, though the actual half pitches of the gates no longer follow the naming nomenclature [10]. A more recent investigation of interconnect power consumption by Adhinarayanan et al. [11] highlights how the first estimate includes the power usage for data access, and the pure interconnect power consumption in an AMD GPU in the 28 nm technology node is estimated at 14%. Furthermore, a prediction of the energy consumption of GPUs in

³See, e.g. Figure 1 in <http://www.gotw.ca/publications/concurrency-ddj.htm>

the 7 nm technology node is made at 22%. The 7 nm technology node is the current industry standard and is expected to be replaced by the 5 nm technology node in the early 2020s, for which the interconnect power consumption can be assumed to be even higher. Using light through waveguides essentially makes the interconnects passive, and heat generation only occurs locally at the light source, and not along the entire interconnect length.

To further emphasize the need for optical interconnects, consider how the arrival of cloud computing has brought with it the need for data centres. By one estimate, for every bit transmitted out of a data centre, more than a million bits have been transmitted inside the data centre [2]. Furthermore, a single search in Google will initiate searches in multiple data centres. Video streaming alone was responsible for 58% of the total downstream volume of traffic in 2018, with Netflix being responsible for 15% [12]. Downstream volume from video streaming is expected to increase up to 80% as the consumer demand increases. To put this streaming into perspective, Professor Leif Oxenløwe from DTU Fotonik found, using data provided by Greenpeace [13], that an hour of Netflix streaming is equivalent to boiling eight litres of water [14]. In a more global example, the mass hit of 2017, *Despacito*, was streamed and downloaded more than 5 billion times in the first half-year of its release, which was estimated by Dr Rabih Bashroush from the University of East London, to have consumed as much electricity as the combined countries of Chad, Guinea-Bissau, Somalia, Sierra Leone and the Central African Republic consume in a single year [15]. In a recent study on the power consumption within a data centre [16], 50% of the total power usage is due to the cooling infrastructure. Furthermore, the global electricity consumption by data centres is expected to grow from 1.1% to 1.5% in 2010 and up to 3% to 13% in 2030⁴ [17]. Data centres are just one part of the big puzzle that is Information Communication Technology (ICT), and the global IP traffic is expected to increase threefold from 2017 to 2022, as predicted by Cisco [18]. In 2012 ICT consumed as much as 4.7% of the global electrical energy [19, 20]. Relating the electrical energy consumed to the CO₂-emissions, this figure corresponds to around 1.7%,

⁴The considerable uncertainty is due to uncertainties in the future demands, future global production of energy as well as the efficiency of future data centres.

which is on the same order as the global aviation industry [21].

In the face of this rising energy consumption by ICT, it is necessary to investigate opportunities for reductions in all areas. One specific area is to adopt a new interconnect technology for shorter distances. An entirely different interconnect, an optical one that may overcome the fundamental limitations of current interconnects while also bringing additional benefits [22].

1.2 Nanolasers for on-chip interconnects

As optics already replaced the electrical connections for long-distance communication, it is not a far fetched idea to consider replacing the short distance interconnects as well. The replacement has successfully taken place as soon as the aggregated bandwidth-distance product exceeds $100 \text{ Gb/s} \cdot \text{m}$ [23], as the energy/bit/distance becomes lower for the optical interconnects. The idea of using optics for short interconnects has even been around for more than 35 years [24, 25]. Already back in 1987, Hutcheson [26] recognized the need for the development of a low threshold laser. Due to the fast-paced advancements of complimentary metal-oxide-semiconductor (CMOS) technology, however, the required threshold of the laser has continuously decreased, and up until recently, when the energy/bit in transistors has stagnated [8], the integrated laser technology has not been able to keep up. There have also been many suggestions for all-optical chips through the previous decades, and the research is on-going, see, e.g. [27] for a recent roadmap. The simplest and perhaps most efficient path forward to combine electronic logical operations with photonic data transmission in a shorter time frame is to implement a photonic Network-on-Chip (NoC), that simply transmits and receives data generated by the existing CMOS processors in different layers. Two such visions can be seen in figure 1.1 [28, 29]. The bottom of figure 1.1a shows the vision by Notomi et al. of NTT [28] where initially a simple combination of an electronic and photonic layer enables optical interconnects between many cores. Further down the line, the additional multiplexing possibilities of photonics can be utilized. Figure 1.1b top, shows a similar vision by Bergman et al. of Columbia University [29] where three layers (Bottom: Electronic processing layer,

middle: Electronic control layer and top: photonic data layer) combine the electronics with photonic interconnects. Figure 1.1b bottom, shows the three different dimensions, space, time and wavelength, that can be utilized to increase data rates when using photonics for interconnects.

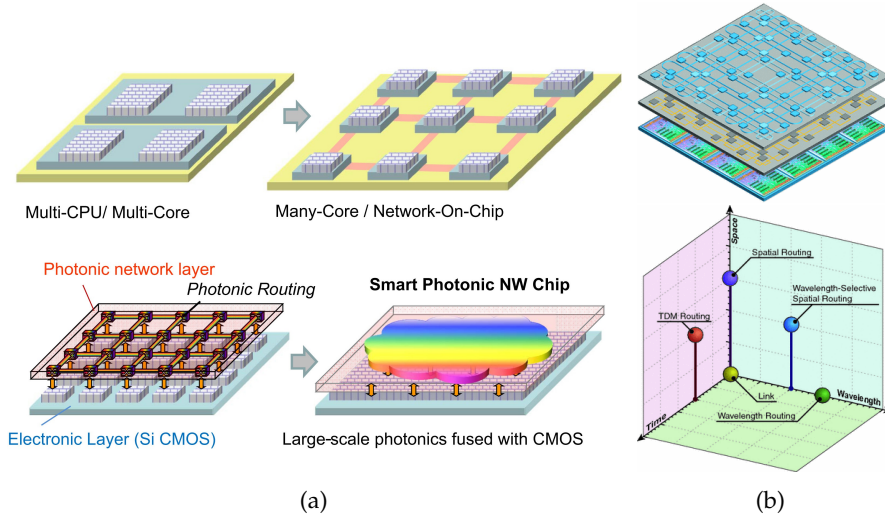


Figure 1.1: Visions for the co-integration of photonic and electronic network-on-chips. (a) Vision by Notomi et al. from NTT. Top figures show the current electronic configuration and the bottom figures show a simple and advanced vision. Reprinted from [28]. (b) Vision by Bergman et al. from Columbia University. The top figure shows a three-layered structure. Electronic logical operations occur in the bottom layer and photonic data transmission in the top layer. The middle is an electronic control layer. Bottom shows the three different dimensions, space, time and wavelength available for multiplexing data to fully utilize the benefit of photonic interconnects. Reprinted from [29].

For the optical interconnects to be a viable replacement for the current electrical ones, minimizing the total energy of the system is the main driver. A recent review by Miller [3] outlined several key goals, where the main one is to obtain a total energy per bit less than 10 fJ/bit for the interconnects in the 1 cm to 10 m range. Two schemes exist to send a modulated signal optically; first, a laser can be continuously on, and a modulator then switches the signal to create a modulated

signal. The energy consumption in such a scheme would be both the continuous operating power of the laser, as well as the energy per bit required by the modulator. An example calculation on a semiconductor laser with an active volume of $1\ \mu\text{m}^3$ can be found in table 2 of [3]. The operating energy of the laser is on the order of 160 fJ, far from the target requirement. Decreasing the active volume while increasing or at least maintaining the cavity Q factor is a direct route to minimizing the operating energy of the laser. By minimizing the active volume to $300\ \text{nm}^3$ and increasing the resonator Q factor, the operating energy can be dropped below the 10 fJ requirement, see table 2 in [3] again. If the laser instead is directly modulated, the energy consumption per bit is simply half the requirement to turn the laser on and drive it at sufficient output power⁵. It should be noted, that the average power consumption of the laser is significantly larger than the energy of a modulator and the laser is the dominating source of energy consumption regardless of whether the system is directly modulated, or an additional modulator is required [3].

Several device platforms may be considered to fulfil the role of the on-chip source for optical interconnects and on-chip communication. A recent review by Matsuo and Kakitsuka [30] looks into current state-of-the-art directly modulated lasers. First, standard in-plane emitting distributed feedback (DFB) and distributed Bragg reflector (DBR) semiconductor lasers have energy costs in the pJ/bit range, see table 5 in [30] for DFB and DBR lasers on silicon. Vertical Cavity Surface Emitting Lasers, VCSELs, on the other hand, are already widely used for interconnections in supercomputers and data centres [31] as their energy/bit consumption is on the order of 100 fJ/bit, see tables 3 and 4 in [30]. Their inherent out-of-plane emission allows efficient coupling to fibers, but additional complexity is required if they are to be integrated into planar hybrid devices. With a high contrast grating [32, 33] in place of one of the mirrors in the VCSEL, the emission of the VCSELs can be in-plane⁶ and the laser wavelength can be controlled better, which could enable wavelength division multiplexing (WDM), and thus increase

⁵Assuming a 0 bit consumes no power and that on average there is an equal number of 0 and 1 bits.

⁶Suddenly making the SE in VCSEL slightly misplaced, which has led to some renaming the device VCIEL, the IE representing in-plane emission.

capacity. Nevertheless, the energy per bit of VCSELs remains too large for it to replace interconnects for the shortest links. As the active size and the footprint of the device are essential characteristics to minimize, device mode volumes on the order of the laser wavelength are especially interesting for the optical interconnections. Hill and Gather review such small lasers in [34] with a comparison between, VCSELs, microdisk lasers, photonic crystal lasers and dielectric and metal plasmon lasers. Of these, VCSELs are the oldest, most mature technology, and the first to leave the laboratories and enter the commercial markets, but for reasons stated above are not ideally suited for interconnections on the shorter length-scales. The microdisk lasers can achieve incredibly high Q factors on the orders of 10^7 [35]. The microdisk lasers can further be coupled to in-plane waveguides and have even demonstrated switching energies in the low fJ range when used in all-optical flip-flop memory setup [36] in a silicon-on-insulator (SOI) CMOS compatible setup. The microdisks, however, have very narrow resonances due to their high Q factors, and they are sensitive to temperature, which must then be controlled. The energy for this control must be included in the total energy calculations, which Miller [1] estimates quickly puts the energy/bit above the 10 fJ/bit limit. The metallic/plasmonic devices can be a potential future candidate for interconnects due to their tiny active volumes $0.28 (\lambda/n)^3$ [37]. However, their Q factors are limited by the loss induced by the metals and further improvement to the room-temperature threshold must be achieved [34].

Finally, photonic crystal lasers can be considered as a candidate for replacing the electrical interconnects on the short length-scale. Photonic crystals may be one, two or three-dimensional periodic structures. In this work, unless otherwise specified, the term photonic crystal refers to a 2D photonic crystal in a slab of finite height. For a summary of the experimental realization of lasers for photonic crystals of different dimensionalities see [38]. The 2D photonic crystal membrane lasers have moderate active material volume, high Q factors and are inherently in-plane lasers [34]. Since the first experimental demonstration of a laser cavity in a 2D photonic crystal slab in 1999 by Painter et al. [39], the platform has seen incredible advancements [38, 40–43]. In a short period, researchers from NTT Basic Research Laboratories consistently improved upon a photonic crystal device with a quantum well buried

heterostructure (BH). The first demonstration with optical pumping on a pure InP platform in 2010 [44] had a remarkable energy consumption of only 13 fJ/bit. This performance was further reduced to 8.8 fJ/bit [45] and later 6.6 fJ/bit [46].

In 2012, the first electrically pumped BH laser was demonstrated [47]. Here the lambda-scale embedded active region PhC (LEAP) laser name is introduced. The device had a large leakage current, and the effective threshold current of the device had to be estimated to 9.4 μA . With a change in the sacrificial layer, the leakage current was significantly reduced, and in 2013 the threshold current was reduced to 7.8 μA and an energy cost of 14 fJ/bit [31]. With the addition of current-blocking trenches, the threshold current and energy cost was further reduced to 4.8 μA and 4.4 fJ/bit, respectively [48]. Recent realizations of LEAP lasers with active region lengths of only a few photonic crystal periods along the waveguide, have shown record low threshold currents of 4 μA and energy costs as low as 1 fJ/bit [49, 50]. Furthermore, heterogeneous integration of the InP platform with an SOI substrate and coupling of laser light into a silicon waveguide on the SOI has been demonstrated [51–53]. The most recent of these [53], had an energy cost of only 7.3 fJ/bit⁷. The fabrication requirements for photonic crystals can be fulfilled by current standard CMOS fabrication lines, and Q-factors on the order of 10^6 have been achieved [54, 55]. Finally, it is worth noting that the photonic crystal platform also allows for the realization of multiple optical components. Recently, electrical-to-optical, E-O, and optical-to-electrical, O-E, converters were integrated to form an E-O-E converter that can enable optical switches, transistors and wavelength converters [56]. In this sense, advancement to the field due to commercialization of any one device based on a photonic crystal platform can drive advancements for other devices.

To summarize, the photonic crystal laser platform has already been proven able to fulfil the energy requirement for optical interconnects and shows promise for integration with silicon fabrication methods.

⁷The increase in energy cost for the devices on silicon are partly due to the InP slab no longer being membranized, but having silica on one side, and air on the other, leading to slightly worse out-of-plane confinement.

1.3 Photonic crystal lasers

In the following, the necessary components of a photonic crystal laser are presented and discussed. In particular, the fundamentals of photonic crystals and different mechanisms for the confinement of light are first presented. Next, a short introduction to the different gain media used in the samples in the PhD project is given.

1.3.1 Photonic crystals

Photonic crystals are low loss dielectric materials with wavelength-scale periodic regions of high and low refractive index [57]. The dielectric function in the material may be periodic in one, two or three dimensions. The study of one-dimensional periodic structures go back to the turn of the 20th century, where diffraction gratings were studied by Lord Rayleigh [58] in 1887 and Wood [59] in 1902. The term photonic crystal, however, does not appear until 1987, when two individual papers by Yablonovitch [60] and John [61], published within two months of each other, investigated the effects of periodic dielectric materials. The two had different motivations for the application of photonic crystals; Yablonovitch sought to diminish the energy lost as spontaneous emission in lasers⁸, while John sought to localize the light to defects in the periodic material [64]. Importantly, both studies rely on the periodicity of the dielectric function in creating a bandgap in all directions, in which certain frequencies are forbidden. Such bandgap materials occur in plenty in nature [65–67] to create beautiful colours in the feathers of the peacock [68] or the black-billed magpie [69], the wings of butterflies [70], the shells of beetles [71] and even in the colour-changing mechanism of the chameleon [72]. Indeed, it is the bandgap and the ability to engineer structures with defect modes inside this bandgap that gives the ability to control light.

As mentioned above, we limit ourselves to two-dimensional photonic crystal slabs in this thesis. A band diagram for such a slab with a triangular hole lattice can be seen in figure 1.2. A TE-like bandgap

⁸Bykov [62], investigated how the spontaneous emission could be controlled in one-dimensional periodic media, and recognized how a three-dimensional periodic structure could reduce the laser threshold [63].

opens for a certain frequency range dependent on the periodicity and radius of the holes as well as the slab thickness. While the periodicity of holes confine light in-plane, the out-of-plane confinement is due to index guiding [57]. The slab has a higher refractive index than the surrounding medium (air), and total internal reflection can occur at the interface if the angle of incidence is smaller than the critical angle. The angle of incidence can be related to the in-plane wave vector as $k_{\parallel} = |k| \sin \theta$, where $|k| = n\omega/c$, where n is the refractive index, ω is the angular frequency and c is the speed of light. A light cone can then be defined as $\omega > c|k_{\parallel}|$ [57]. For frequencies inside the light cone, the modes are no longer confined but can radiate to the surrounding air. The blue shaded area in figure 1.2 shows the light cone for the slab. The reduced Brillouin zone for the periodic structure can also be seen. For more on the theory of photonic crystals, see the textbook "Photonic Crystals: Molding the Flow of Light" by Joannopoulos et al. [57].

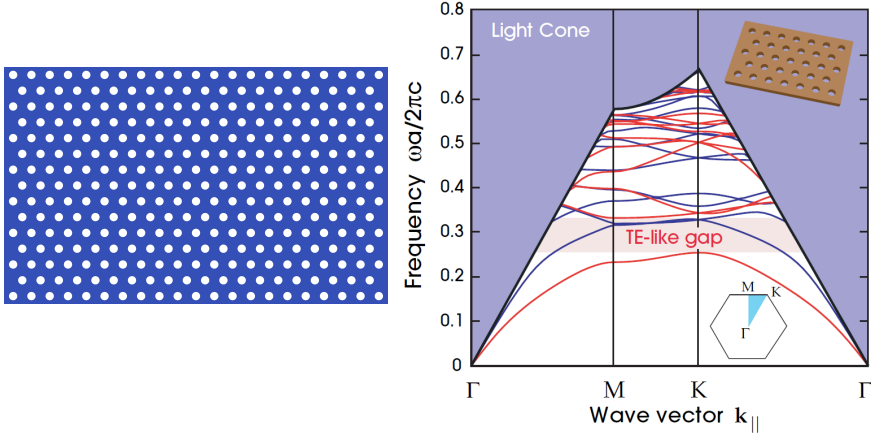


Figure 1.2: Left: Unperturbed photonic crystal. Right: Band diagram of a 2D photonic crystal slab with a triangular hole lattice. The red (blue) lines indicate TE (TM)-like modes. A band gap for TE-like modes appears for certain frequencies. The blue shaded area represents the light cone. The reduced Brillouin zone of the periodic structure is also shown. Reprinted from [57].

As Yablonovitch predicted, the spontaneous emission can be altered when the emitters are embedded in a photonic crystal, which was shown

for 2D photonic crystal slabs in 2005 [73]. In such a bandgap structure, where propagation is forbidden for electromagnetic waves within a certain range of frequencies, defects can be introduced to create defect states inside the bandgap, which can strongly localize the electromagnetic field. Next, we discuss four different defects, to guide and confine light in 2D photonic crystal slabs: The line defect waveguide figure 1.3a, the line defect cavity figure 1.3b, the double heterostructure cavity figure 1.3c and the Fano cavity figure 1.3d.

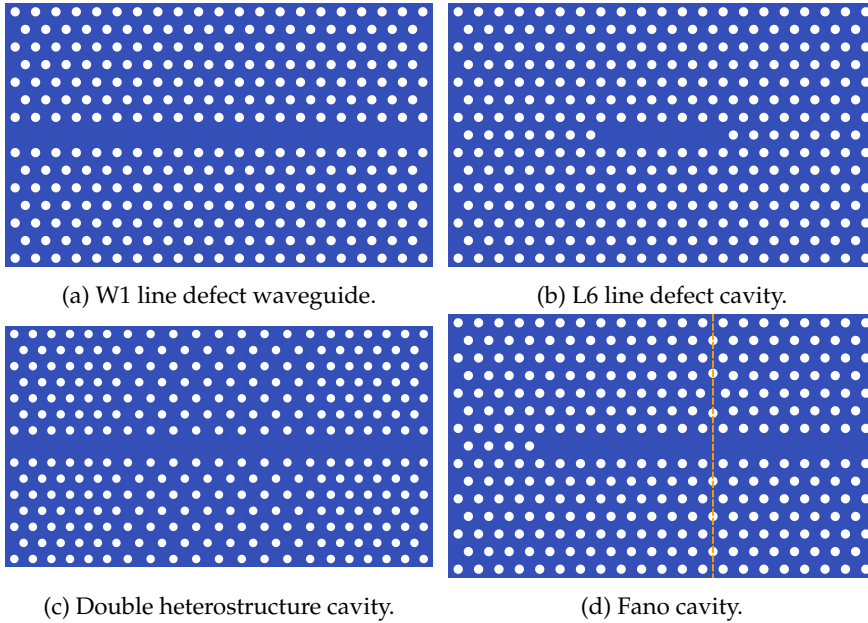


Figure 1.3: Four different defects to (a) guide light in a W1 line defect waveguide, or confine light in (b) a line defect waveguide, (c) a double heterostructure cavity or (d) a Fano cavity. In (c) a region with a different period forms a double heterostructure. In (d) a cavity is formed by a normal photonic crystal mirror (left) and a mirror formed by interference between the continuum of waveguide modes with a discrete nanocavity mode. The dashed line indicate the position of the nanocavity.

Line defect waveguide

Removing a row of holes in the photonic crystal lattice creates a line defect waveguide denoted as W1 [74], see figure 1.3a. Figure 1.4a highlights how different guided modes appear when a row of holes is removed. The dashed line from (c) to (d) is a y-odd guided mode within the bandgap. Whether a mode is odd or even depends on reflection in the $y = 0$ plane (see inset coordinate system) [57]. The odd modes are most easily excitable by plane-wave light [57], which makes them interesting. The bandgap and the defect mode may be tailored by changing the waveguide width [75], or shifting entire rows of holes laterally or longitudinally [76].

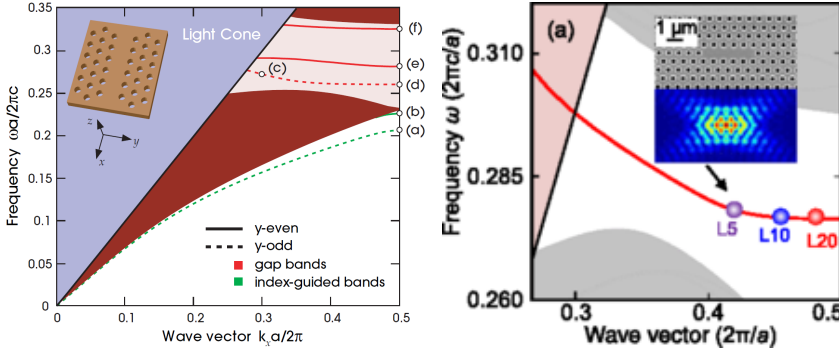


Figure 1.4: Line defect structures in 2D photonic crystal slabs. Left: W1 waveguide with guided modes in the band gap. Reprinted from [57]. Right: Discrete localized fundamental modes for L5, L10 and L20 line defect cavities. Reprinted from [77].

Line defect cavity

Instead of removing an entire row of holes, consider only removing a limited number of holes in a row to form a defect, see figure 1.3b. The cavity is designated as an L_n -cavity, where n is the number of omitted holes [78]. In such a perturbation of the photonic crystal, discrete localized modes are confined to the defect area. The resonance wavelength and corresponding wave vector depend on the number of removed

holes, see figure 1.4b, where the fundamental mode of L5, L10 and L20 cavities is highlighted. As the cavity length is increased, the number of confined modes within the cavity increases. Importantly, the line defect modes fall on the dispersion curve (the red line in figure 1.4b) of the gap guided mode for the open waveguide. Therefore, the cavity resonance wavelength can be tuned by varying the period of the photonic crystal or the radius of the holes. Optimizing the Q-factor of line defect cavities has received extensive interest where position or size of individual holes is usually changed [79–84]. In this project, the Q-factor is optimized by shifting holes. In chapter 4, the first hole in each end of the mirror are shifted similar to [79], while in chapter 5 a second round of optimization similar to [83], is carried out and both the first and third holes in both ends of the mirror are shifted.

Double heterostructure cavity

The double heterostructure cavity, see figure 1.3c, was introduced by Song et al. in 2005 [85]. Here, light is confined by introducing an area where the photonic crystal period is changed by ≈ 2.5 percent of the period. The bandgap and waveguide dispersion curve for the two different photonic crystals vary slightly, and can be engineered so that light at certain wavelengths can propagate in one part, but are forbidden in the neighbouring part, leading to reflections and ultimately a cavity is formed⁹. In the initial studies of the double heterostructure cavity, the period was changed to confine the light [87, 88]. However, the heterostructure may be formed by other variations, such as direct variation of the refractive index [86, 89], or the addition of a buried heterostructure gain material [44]. The record-breaking photonic crystal lasers with extremely low threshold fabricated by NTT [31, 44–50] are all based on the double heterostructure cavity. The double heterostructure cavity Q-factor can be optimized by making the transition between different photonic crystal regions gradual instead of abrupt [81, 88]. Such optimization is easier to carry out on structures where the period is modulated compared to structures with a buried heterostructure gain medium.

⁹See for example figure 2 in [86]

Fano cavity

Lastly, consider the photonic crystal Fano structure in figure 1.3d. Proposed by Mørk et al. in 2014 [90], the Fano cavity is comprised of two very different mirrors. One mirror is a standard photonic crystal mirror obtained by simply terminating the line defect. The second mirror is realized by a so-called Fano mirror based on the interference between a discrete nanocavity mode and the continuum of modes in an open waveguide. The larger cavity formed between these two mirrors is denoted the line defect cavity. Light in the line defect cavity travelling towards the Fano mirror can either go straight into the open waveguide or travel via the nanocavity. Far away from a nanocavity resonance, the coupling into the nanocavity is small and the reflectivity of the Fano mirror low. As the frequency approaches a nanocavity resonance, the light couples to the nanocavity, and after coupling back into the open waveguide, it can interfere destructively with the part of the field that went straight into the open waveguide. As the nanocavity has discrete resonances, the coupling into the nanocavity is extremely frequency-dependent, essentially leading to a narrowband mirror. The coupling between the light in the waveguide and the nanocavity is an important parameter in the device and can be tuned with a partially transmitting element (PTE), e.g. a hole, in the open waveguide. Varying the PTE size can tune the coupling and thus the reflectivity of the mirror [91] while the position of the PTE in relation to the nanocavity can tune the parity and lineshape of the mirror [92].

The photonic crystal Fano laser is a rich device platform, which has been predicted to possess several unique features. As the mirror reflectivity is dependent on the nanocavity resonance, the device may be tuned by modulating the nanocavity. It has been predicted that Fano lasers can be frequency modulated with a bandwidth exceeding 1 THz [90, 93, 94], and that ultra-short pulse generation in the ps range is possible [90]. The photonic crystal Fano laser was recently experimentally demonstrated [95], and found to be single-mode with a resonance wavelength independent of the line defect cavity length. In standard line defect lasers the cavity resonance redshifts for increasing cavity length, see figure 1.4b. Furthermore, the experimental demonstration revealed a transition from continuous-wave operation to self-pulsing

with increasing pump power. The theory behind the self-pulsing has since been investigated in [96]. Finally, it has recently been predicted [93], how the nanocavity acts as a narrowband filter, which reduces the bandwidth and leads to damping and a reduction in the relaxation oscillation frequency and 3 dB bandwidth. Such a damping may lead to increased stability to feedback [97], which may turn out to be practical if the photonic crystal Fano lasers are to be used for optical interconnects, because integrated optical isolators that can easily be combined with the photonic crystal platform have yet to be developed.

1.3.2 Gain media

With the different cavity designs in place, all that remains to form a laser is the gain medium. The fabricated active photonic crystal devices use embedded InGaAsP/ InAlGaAs quantum wells or InAs quantum dots to achieve optical gain. When quantum wells or quantum dots are formed by confining carriers in 2D or 0D, respectively, the density of states (DOS) changes dramatically from that of bulk semiconductor material. For bulk semiconductor material, the DOS increases with a square root dependence on the energy difference from the bandgap. For quantum wells, the DOS is a step-like function, while the DOS of quantum dots are discrete peaks at discrete energies. See figures 4-6 in Lee et al. [98] for the evolution of the density of states as the bulk material is gradually restricted in one spatial dimension at a time until the 0D quantum dot is obtained. For 3D (bulk), 2D (quantum wells) and 1D (quantum wires)¹⁰ semiconductor materials, the carrier distribution is determined by the Fermi-Dirac distribution function and the DOS. The temperature dependence of the Fermi-Dirac distribution function limits the peak gain [99]. For identical quantum dots, however, despite the temperature dependence of the Fermi-Dirac distribution, there are no states the carriers can be excited. As a result, quantum dot lasers are less sensitive to temperature increases than their quantum well counterparts [100].

¹⁰Intermediary between quantum wells and quantum dots, which will not be further discussed.

Furthermore, population inversion in the gain material is achieved more easily as the gain material is reduced in size, as there are inherently fewer states. This has already been utilized for the quantum well photonic crystal lasers to demonstrate the record low 1 fJ/bit operation [50]. Moving to quantum dots represent a natural next step to reduce the active material volume further, and further decrease the laser threshold.

1.4 Overview of the thesis

The work done during the PhD and presented in this thesis contributes to the field of photonic crystal nanolasers. The ambition of the project has been to gain a deeper understanding of the underlying physics of photonic crystal lasers, both simpler line defect lasers, as well as newer designs with Fano mirrors, and particularly devices with buried heterostructure gain material.

The remainder of the thesis is organized as follows:

Chapter 2 first introduces the reader to the fabrication method of the photonic crystal lasers, and passive photonic crystal cavities reported on in the thesis. Changes and updates to the process developed during the PhD are presented, and investigations into dry-etches of the holes in the photonic crystal are presented with the ultimate goal of fabricating a better photonic crystal laser. Specifically, the sidewall roughness inside the holes, and the verticality of the holes are investigated to optimize the Q-factor of fabricated devices.

Next, a short investigation on the buried oxide thickness found to affect the light confined in the InP membrane is presented. The chapter finishes with a description of different experimental setups used for the characterization of fabricated devices, as well as their limitations and prospects for upgrades.

Chapter 3 is divided into two parts. First, the reader is introduced to a classic rate equation model for lasers, along with the specific assumptions used in this work. The model is used in later chapters for experimental fits to fabricated devices. An automated fitting tool has been implemented, see appendix C, which

puts restraints on the complexity of the model used to describe the material gain. A discussion on approximations to the material gain model follows, before steady-state solutions to the rate equations are presented. The first part ends with a description of how the threshold pump power is extracted from experimental input-output curves and how it is necessary to limit the different parameters in the laser rate equation model to suitable ranges before using the autofitting tool. The second part describes the basic setup of finite difference time domain (FDTD) simulations of equivalent passive photonic crystal cavities in the commercial software Lumerical. The simulations are used prior to device fabrication as a design tool as well as a tool to gain a deeper understanding of the more complex structures presented in the later chapters.

Chapter 4 experimentally investigates how the threshold power of an L7 line defect photonic crystal laser can be minimized by optimizing the cavity Q factor. The optimization is done by shifting the first two endholes in the photonic crystal mirror. Next, the mirror phase of the photonic crystal L7 cavity with shifted endholes is investigated through FDTD simulations. Lastly, the penetration depth of the electric field into the photonic crystal is investigated.

Chapter 5 introduces photonic crystal lasers with buried heterostructure (BH) gain material. Samples with BH of varying length in an L7 cavity is characterized and compared to FDTD simulations. The results require a deeper understanding of the photonic crystal with embedded BH, so an extensive FDTD investigation is carried out on different configurations of photonic crystal with embedded BH. An effective medium theory for the embedded BH is introduced to minimize the computational requirements of the FDTD simulations.

Chapter 6 is dedicated to the experimental investigation of Fano lasers with the embedded BH. The investigation aims to determine experimentally if the self-pulsing of the photonic crystal Fano laser structure, observed in [95] for lasers with QDs embedded in the entire laser, is eliminated when the nanocavity is entirely passive,

and the BH is only confined in the LD and waveguide region. Preliminary FDTD simulations reveal how the addition of the BH in the Fano laser structure can lead to multiple less intense modes confined to the BH and only weakly reflected by the Fano mirror. Furthermore, due the complicated optimization required for the Fano laser structure, the device performance is predicted to quickly degrade if a BH of varying length is embedded only in the LD region without any prior optimizations.

Chapter 7 concludes the thesis with final remarks and a look to the future.

CHAPTER 2

DEVICES: THEIR FABRICATION AND BASIC CHARACTERIZATION

This chapter describes the fabrication methods of the photonic crystal lasers and the passive photonic crystal samples made during the PhD project. The description includes any developments to the process flow during the project period. A brief introduction to the fabrication process is followed by a closer look at the fabricated holes, their quality, and how the dry-etch process was improved. The quality of the holes was early in the project found to be an issue. The sidewalls were not vertical, and the surface appeared rough. Some holes also suffered from slight deformations and were not completely circular. The fabrication process is complex and different degradations to hole quality can have many origins in the fabrication process. Thus, different steps have been taken to try and improve the hole quality, and these steps will be highlighted. Next, a discussion of an issue encountered where the buried oxide led to wrong determinations of the photoluminescence (PL) spectra used for quality control when growing the active material follows. Lastly, the experimental setups used throughout the thesis to characterize the samples are presented and described.

2.1 Fabrication process overview

This section starts with a summary of all the fabrication steps necessary to fabricate the photonic crystal devices. Previous PhD students and Postdocs developed the original process for the photonic crystal devices [101]. During the PhD project, several other PhD students and Postdocs¹ in the group worked together towards realizing an electrically pumped photonic crystal laser with a buried heterostructure, confining the gain medium only to the cavity area. See the PhD thesis of A. Sakanas for a detailed introduction to the buried heterostructure and the direct bonding method [102]. The addition of a buried heterostructure, as well as doping and metallization for electrical pumping, brought changes to the process. The electrical injection still has obstacles to be overcome, and this thesis is not about the electrically pumped photonic crystal laser. It is, however, a clear future goal. Thus, some changes have already been implemented in the process flows for samples without BH or electrical injection, to ensure the photonic crystal is easily transferred once the electrical injection scheme has been implemented. The following summary includes the most recent version of the process used by the author to fabricate samples that will be characterized in the latter part of the thesis. Individual subsections will dwell on changes made to the recipe where the author contributed to the change of process. The full process flow, with the equipment used at DTU Nanolab, and process parameters can be found in appendix A.

For active samples, buried InAs quantum dots or InGaAsP/InAlGaAs quantum wells are epitaxially grown on an InP wafer with an InGaAs etch stop layer² in metalorganic vapour-phase epitaxy (MOVPE). More specific information on the epitaxial growth of the quantum wells and quantum dots embedded in the samples in this work can be found in Appendix C of [102]. For passive samples, a pure InP layer is grown, still, with the

¹Aurimas Sakanas, Andrey Marchevsky, Dagmawi Bekele and Evangelos Dimopoulos.

²The etch stop layer is necessary when removing the substrate after bonding.

InGaAs etch stop layer. A thermal oxide is grown on a Si wafer in a plasma-enhanced chemical vapor deposition (PECVD), and a thin layer of Al_2O_3 is deposited by atomic layer deposition (ALD) on both wafers before they are directly bonded together, and the InP substrate and InGaAs etch stop layer is removed by wet etch. At the beginning of the project, the samples were not directly bonded, but the polymer Benzocyclobutene (BCB) was used to glue the two wafers together. Specifically, the samples in chapter 4 are BCB bonded. The addition of BH required direct bonding to ensure better alignment between the BH and the photonic crystal structures. The direct bonding was not developed by the author, but the change caused issues when measuring the photo luminescence of the samples related to the buried oxide thickness, which will be discussed in section 2.3. Further, the author only performed the fabrication process after the samples had been bonded, and the InP substrate and InGaAs etch stop layer removed. The fabrication process performed by the author can be separated into the following steps:

1. A 200 nm thick Si_3N_4 hard mask is deposited by PECVD.
2. A 500 nm thick electron beam resist, ZEP520A, is spin-coated on top of the hard mask, and the sample is baked.
3. The photonic crystal pattern is transferred to the resist with electron beam lithography.
4. Resist is developed.
5. The Si_3N_4 hard mask is etched in ICP-RIE, the resist is stripped, and the sample is cleaned with a plasma asher.
6. The InP membrane is etched using RIE.
7. The Si_3N_4 hard mask is stripped at the same time as the SiO_2 is removed underneath the photonic crystal patterns with SiOetch^3 .

The end product is an InP membrane with/without embedded quantum dots or wells for light generation and a photonic crystal

³A BHF solution from BASF

pattern to confine the light. A graphical representation of the steps above can be seen in figure 2.1

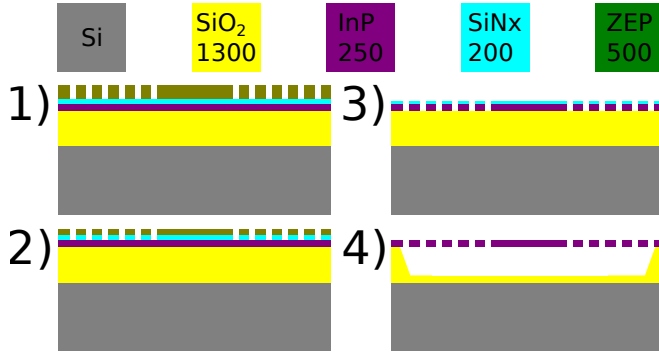


Figure 2.1: Graphical representation of the process flow. 1) Definition of resist. 2) Transfer of pattern to hardmask. 3) Transfer pattern to the InP membrane. 4) Final membranized structure. Thicknesses are in nm.

The nitride hard mask deposition

The nitride hard mask is used to transfer the pattern to the InP membrane, and good definition of the nitride hard mask is, therefore, necessary for good definition in the InP membrane. As there were always mask remaining after the InP dry etch step, it was proposed to lower the thickness of the nitride from 200 nm to 100 nm. A thinner nitride mask lowers the aspect ratio. It has the purpose of making vertical sidewalls easier to achieve, which should serve to improve the quality of the holes etched in the InP membrane, which will be discussed in section 2.2. Newer samples fabricated by others have adopted the 100 nm thick nitride hard mask, but all the samples characterized in this thesis retain the older 200 nm thickness.

The e-beam lithography

At the onset of the PhD project, the e-beam lithography carried out was standard, i.e. a dose was defined for all structures and then exposed. As mentioned above, the quality of the fabricated holes

had issues with sidewall verticality and roughness. The e-beam process is the first transfer of the design from the mask to the sample, and a good place to begin the optimization of hole quality. One of the steps taken to optimize the e-beam lithography was the addition of proximity error correction (PEC). In the e-beam lithography process, electrons are shot into the material, to alter the composition of the e-beam resist and make it soluble in resist developer [103]. While the initial entry point of the electron is well-defined by the different electromagnetic lenses in the e-beam machine, the electron undergoes different scattering events in the sample and can develop the resist far away (few micrometers) from the actual point of entrance. Simply put, electrons meant to expose one hole, may contribute to the exposure of neighbouring holes. To compensate for the proximity effects, Monte Carlo simulations were carried out where electrons are shot into a layered stack of materials defined by the different refractive indices of the layers in the actual sample. These simulations were carried out in the commercial software Tracer, in order to determine the point spread function (PSF). The PSF describes the energy density deposited in the resist layer at some distance from the initial entry point [104, 105]. The PSF was applied to the e-beam mask in the software Beamer, which resulted in dose variations between individual holes based on their surroundings, but also in slight variations within each hole. In effect, the holes closer to the side receives a smaller dose than the holes in the center. Similarly, the holes next to the cavity receive a slightly higher dose. The MATLAB script written to determine the hole sizes, which will be further described in section 2.2, was adapted to colour the individual holes in an SEM image according to their radius. Even without the PEC, no systematic variation in size could be found. The addition of the PEC step then primarily serves to optimize the roundness of each hole. Furthermore, when the holes are exposed in the e-beam, the holes are converted into individual e-beam shots. These shots are on a rectilinear grid with some stepsize (4 nm to 10 nm was used throughout the project). A curved surface on a rectilinear grid will always suffer some loss of the edge

definition⁴. To fabricate rounder holes the fracturing method was changed from standard, which always places the first shot in a given y -position at the leftmost point of the hole and continues placing subsequent shots with the stepsize Δx until the right side is reached. The final shot on the right side rarely hits precisely on top of the polygon defining the hole, but often slightly before or after. As the hole is mapped in the y -direction the right side of the hole is no longer similar to the left⁵. Atsumi et al. investigated the shot shape fracturing effect on waveguide loss in 2014 [106], where a reduction in loss from 4.7 dB/cm to 3.0 dB/cm was observed by changing the fracturing method so the shots aligned better with the edges, lowering the line edge roughness. Curved fracturing is an alternative approach and readily available in the JEOL e-beam at DTU Nanolab. In this scheme, the shots are first placed on the outer parts of the holes, and then the center part is filled last. The curved fracturing method results in an equal fracturing of holes on all sides, at the cost of some overlap, and thus slightly higher dose in the center of the hole. The author fabricated one sample using this method with success. However, subsequent fabrications by others including some smaller radii holes, ≈ 60 nm, resulted in the smaller holes being more square rather than round. As such, the method is not currently in use, but the author encourages future investigations into this part of the process.

The nitride hard mask etch

At the beginning of the project, the nitride hard mask was etched in a standard reactive ion etch (RIE) process. The process always seemed adequate to produce a well-defined hard mask, as the nanolasers fabricated achieved CW lasing under optical pumping in the lab. A deeper look into the shape of the holes revealed how the nitride mask degraded during the InP etch. The sidewall

⁴As a simple example, the reader is invited to draw a circle in paint and zoom into the edge.

⁵See the Beamer manual for more information on the different fracturing modes.

angle of the nitride mask after InP etch is far from vertical and can be seen in figure 2.3a, which could transfer into non-vertical sidewalls of the holes in the InP membrane. Therefore, the recipe should be tweaked, or a different dry-etch machine should be used to optimize the hard mask definition. SEM images and a deeper discussion is reserved for section 2.2. A test run by Luisa Ottaviano had shown that the inductively coupled plasma reactive ion etch, (ICP-RIE) process could also be used for etching of nitride. In ICP-RIE the plasma is created by an inductively coupled plasma source, and the plasma can be sustained in lower pressure than standard RIE. Lower pressure can give better control of etch anisotropy which is necessary for vertical holes. The ICP-RIE process was originally developed for etching larger open areas and had to be slightly adapted to fit our purpose. Firstly, it did not etch through the holes before the resist was used up, so the etch rate had to be improved. The composition gasses in the chamber is important in controlling the etch rate and selectivity of the etch. After inspecting the individual gas flows, the flow of the CH₄ gas in the original recipe was found to be on the edge of the detection of the installed flowmeters. If the flow of CH₄ was not constant during the etch, this would alter the etch rate. All flows were then increased while keeping the individual ratios between gasses constant, and maintaining the chamber pressure at 3mTorr. The original and final values of the gas composition can be found in table 2.1. With a higher flow of gasses holes could be etched with some e-beam resist remaining. Secondly, the process had reproducibility issues, where two nearly identical samples etched with the same recipe could have drastically different outcomes. It could be all from not etched at all to fully etched or somewhere in between. The plasma did not always ignite when the power to the coil and platen turns on. A strike-out was added to the recipe where the plasma is ignited in a higher pressure environment (10 mTorr) for three seconds before the pressure is then dropped to the original (3 mTorr). The strike-out solved the issue, and the recipe is used for all current processing.

Table 2.1: Original and final composition of gasses in the developed Si_3N_4 etch recipe for ICP-RIE

	SF_6	CF_4	CH_4	N_2
Original	4 sccm	4 sccm	2 sccm	20 sccm
Final	12 sccm	12 sccm	6 sccm	60 sccm

Etching of the InP membrane

The InP membrane is etched in a cyclical process in standard RIE. As will be shown later, the holes suffer from a poor surface quality and non-verticality. The non-verticality can be partly due to the quality of the hard mask, but the surface quality is only affected by the dry etch of InP. Secondly, in late 2018 and early 2019, the etching suddenly changed. From one day to the next, the fabricated holes were much larger. The same was also observed by colleagues using the same equipment and recipe, but nothing had seemingly changed with the process recipe nor the machine. Some etch tests were done, and with a reduced number of cycles (from 17 down to 14), the holes could once again be fabricated in the designed ranges. The sudden change in process results combined with the poor sidewall quality in the holes was the final motivation to develop an etch for the holes in InP in the ICP-RIE. Aurimas Sakanas had already developed a recipe to etch InP in his effort to fabricate buried heterostructure devices [102]. The developed recipe was once again for large openings and had to be significantly modified to etch the holes. The development of the ICP-RIE etch for the InP holes was not done by the author, and the change to the ICP-RIE was not implemented until late in the PhD project. All samples characterized in this thesis were etched with the standard RIE process.

Membranization and nitride mask removal

During the project, the oxide quality changed, which increased the time needed for proper membranization of the samples. Secondly, and more importantly, the thickness of the oxide layer changed.

After the InP has been directly bonded to the SiO₂ on Si and the InP substrate removed, the quality of the gain material is checked with PL measurements. As will be shown in section 2.3, the thickness of the oxide affects this measurement through interference effects. For the directly bonded samples in this thesis, the oxide is 1.3 μm thick. The designs for the electrically injected photonic crystal lasers include grating couplers for efficient extraction of the in-plane laser light, and the efficiency of the grating couplers require optimization to a specific oxide thickness. The grating couplers are optimized for oxide thickness of 1085 nm, and future samples will be fabricated with this oxide thickness. The nitride hard mask is simultaneously removed during the membranization wet etch. The etch time needed for proper membranization of the sample is also sufficient to remove the nitride hard mask completely.

2.2 Hole sizes and shape

As the fabrication of the photonic crystal involves both an e-beam step, and subsequent transfer to a hard mask before the final etching of the InP mask is carried out, the resulting hole sizes always vary slightly between fabrication runs. Therefore, all radii in the e-beam mask are divided by some design factor (typically around 1.2). The design factor is updated between fabrication runs, so the next process is always designed in relation to what was last fabricated. More importantly, all designs are fabricated for a range of different radii, so at least a single row in a block of photonic crystal lasers falls in the intended radius range and perform well. The fabrication quality of a photonic crystal device can be separated into two different requirements. First, the holes must have a uniform size distribution across the photonic crystal. Any local changes in radii impact the electromagnetic field and serve to lower the performance of the fabricated sample. Secondly, the holes must individually be of good quality, which can be further separated into two requirements. First, the sidewalls in the

holes must be smooth, as surface roughness cause scattering loss [107, 108]. Secondly, the air holes should have vertical sidewalls, i.e. the final air part should be a cylinder and not a truncated cone. If not, this also lowers the Q-factor of the device [108, 109].

To accurately assess the fabricated hole sizes, a MATLAB script was written that finds circles in SEM images of an entire range of radii. The script can be found in appendix B. The first advantage of such a script is automatization, removing the human part when manually fitting single circles on top of holes at the actual electron microscope. The second and more important advantage is that it allows fitting to many holes (upwards of 300) at the same time, and thus provide statistics on the hole sizes. From the statistical analysis of the holes, the latest successful fabrications in the project had standard deviations of hole sizes < 3.5 nm. Such a standard deviation is on the same order of magnitude predicted by Minkov et al. in 2013 for photonic crystals based on III-V platforms [110]. A typical SEM image can be seen in figure 2.2 along with the fabricated hole radii compared to the design radii. For practical purposes, it is important to keep the pixel size the same on all images to be analyzed, which is done by fixing the width of the SEM image to $10\text{ }\mu\text{m}$. The disadvantage of this approach is that the pixel size in the SEM image becomes large (≈ 10 nm when the image must hold this many individual holes). A pixel size that is larger than the obtained standard deviation of holes could put a limit on the variation in radii that can be observed with the program, especially when the holes decrease in size. However, the code fits circles, and errors caused by the pixel size being too large are averaged out as the circumference of the circle is traced. It is still important to also do a few manual checks of the hole sizes for each fabrication run. The effect of the pixel size was checked by instead using $5\text{ }\mu\text{m}$ wide images, which is closer to the standard deviation found, with only a quarter of the holes. No significant change in the absolute hole size or the standard deviation across a sample was found.

With the uniformity of the holes analyzed, the focus turns to the quality of the individual holes. As mentioned above the hole

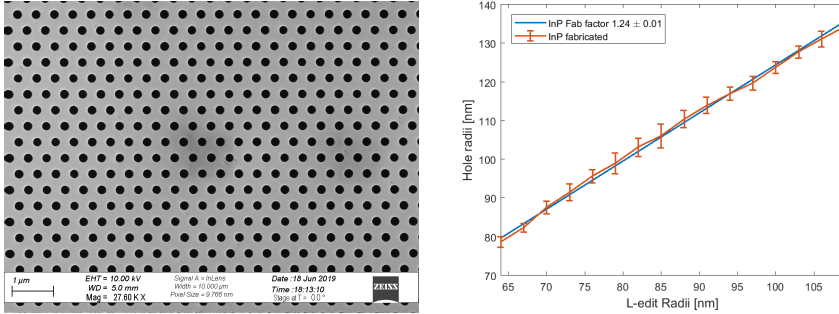


Figure 2.2: Left: Typical SEM image of photonic crystal holes used for hole size analysis. Right: The individual radii of holes are plotted with their size variation and a linear fit is made to determine the design factor for varying design radii. Here the design factor is found to be 1.24.

quality degrades when the sidewalls are rough and if the verticality is poor. The holes fabricated in this project suffer from both of these issues. As can be seen in figure 2.3, the sidewall has considerable roughness, and the angle of the sidewall is not vertical. The sidewall roughness can only come from the InP etch while the sidewall angle can be influenced by the prior lithography and etch steps. As can be seen from the left image in figure 2.3 the quality of the hard mask is poor after the etch of InP. Both samples imaged in figure 2.3 had the hard mask etched in RIE. The main motivation to switch the nitride etch to InP was to achieve a better hard mask quality. The hard mask directly after dry etch in ICP-RIE (left) and RIE with the resist stripped (right) can be seen in figure 2.4. From the top-down image, it is easy to see the hole radii are not uniform through the membrane and using the inner and outer radii of the hole the sidewall angle can be estimated to $\approx 15^\circ$. With the ICP-RIE etch the sidewall is overall more vertical. The sidewall angle was measured for multiple samples and was found to be below 6° consistently. A clear lip is visible at the bottom where nitride meets InP. This lip will be the first thing removed when the etching of InP commences. The developed etch for the nitride hard mask with ICP-RIE has the ability to

outperform the old RIE etch process. It is worth noting that the sidewall angle of the InP membrane is what ultimately matters. For both etch processes for the nitride mask, the InP sidewalls are more vertical than the sidewalls of the nitride mask. Even with the RIE process used to etch the nitride mask, angles as low as 3° could be fabricated, see figure 2.3 right bottom. However, as found by Tanaka et al. [109] even an angle of 1° can lead to significant losses. The motivation for the ICP-RIE for the nitride mask is to obtain better verticality of the InP holes, while the ICP-RIE etch of the InP holes is motivated by smoother surfaces. Samples with InP etched in the ICP-RIE has since been made by other group members, where the sidewall roughness is decreased.

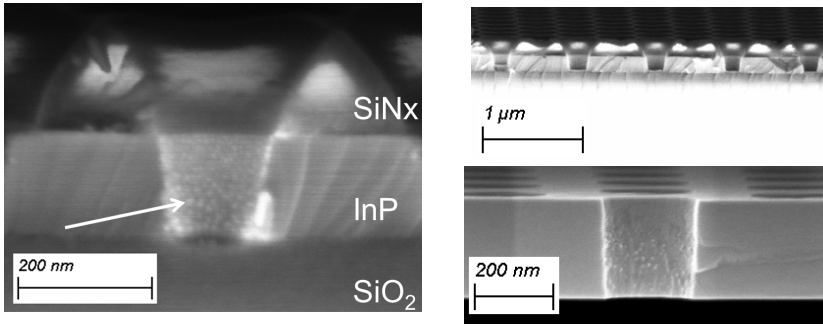


Figure 2.3: Typical SEM images of a cleaved sample with the InP membrane still on top of the silica, and with the nitride hardmask. Left: Close up of a hole from the side. The surface roughness inside the hole is indicated by the white arrow. Right top: Several holes where the sidewall angle is clear. Right bottom: Close up from a different sample after membranization. In both samples the nitride mask was etched with RIE.

2.3 Buried oxide thickness and PL spectra

The thickness of the oxide layer was approximately $3\text{ }\mu\text{m}$ for the BCB bonded samples. When the switch was made from BCB to direct bonding, the buried oxide layer suddenly affected the PL measurements. The PL measurements provide important sample

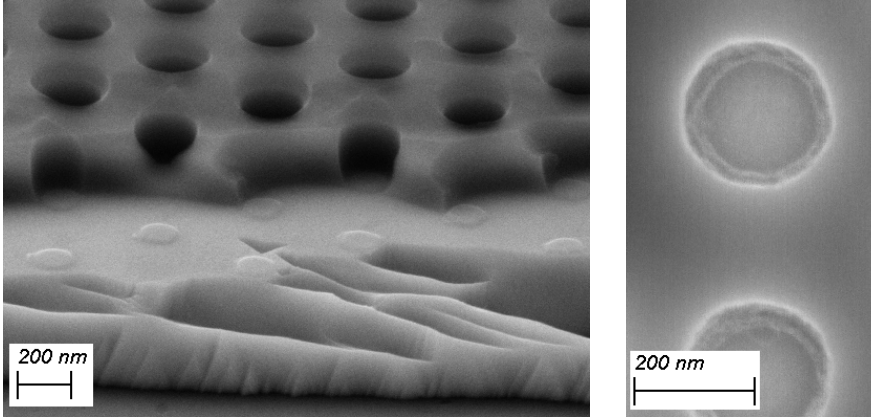


Figure 2.4: The quality of the nitride mask directly after etch. Left: With ICP etch and resist still on top. The top translucent layer is the remaining e-beam resist, followed by the etched nitride on top of the unetched InP. Right: With RIE etch and resist stripped. From the inner and outer radii of the holes the sidewall angle is estimated to $\approx 15^\circ$.

characteristics, i.e. the wavelength range that can be expected to provide gain, which is used to design the photonic crystal, so the cavity resonance has a good overlap with the PL measurement. Specifically, the PL measurements occasionally had two peaks and sometimes only one, see figure 2.6 for two different oxide thicknesses compared to a wafer without any oxide. The three wafers (2.89 μm thick SiO_2 , 2.77 μm thick SiO_2 and no SiO_2) were epitaxially grown simultaneously in the MOVPE and the PL measurements should be comparable. These samples have embedded quantum wells. It should be noted that the quantum wells are designed to have only one state in the conduction band, but in the valence band, the heavy and light hole branches are split, due to the wells being compressively strained. See Appendix 11 in [11] for further information on strained bandgaps. This splitting can cause two peaks to appear in the PL spectra, but the same peaks should then be visible for all oxide thicknesses.

FDTD simulations in 2D were carried out with a dipole source

embedded in the InP membrane and a time monitor placed $5\text{ }\mu\text{m}$ directly above the dipole monitored the field to obtain a spectrum for a given oxide thickness, see figure 2.5 left. The thickness was then swept from $1\text{ }\mu\text{m}$ to $3\text{ }\mu\text{m}$ in steps of 10 nm . The result can be seen in figure 2.5 right. From this, it can be seen that certain oxide thicknesses allow poor light emission from embedded dipoles in the wavelength range from 1500 nm to 1600 nm . The effect can be explained by interference between fields reflected at the different material interfaces in the vertical direction.

Comparisons of the FDTD results with PL measurements on two samples with different oxide thicknesses were made, see figure 2.6. The oxide thickness was measured by ellipsometry. For the sample with a thickness of $2.89\text{ }\mu\text{m}$, the interference causes the PL peak to split into two, where the side peak is less intense. For the sample with a thickness of $2.77\text{ }\mu\text{m}$, the overlap between the PL peak and the intensity profile is better, and the PL peaks only split slightly, resulting in a broad PL. Inspecting figure 2.5 right, a new oxide thickness of $1.3\text{ }\mu\text{m}$ was finally chosen as it leads to more than 90% emission in the entire range from 1500 nm to 1600 nm .

Above, the simulations were made, so the oxide layer did not affect light emission from quantum dots or quantum wells embedded in the unstructured membrane. The inverse problem, i.e. coupling pump light into the gain material is also essential. Some fabricated samples where only a portion of the oxide layer was membranized, exhibited limited pumping and collection efficiency. The limitation was overcome by merely etching the samples for longer, which increased the signal from the samples. The oxide thickness can be a limiting factor for samples where the pumping and collection are carried out through the same microscope objective above the sample. An oxide thickness that allows the pump light to pass through the gain medium multiple times and thus increases absorption can limit the amount of light that is collectable in the microscope objective. Pumping efficiency as a function of oxide thickness still needs further investigations. However, in the worst case for pumping, the light only passes

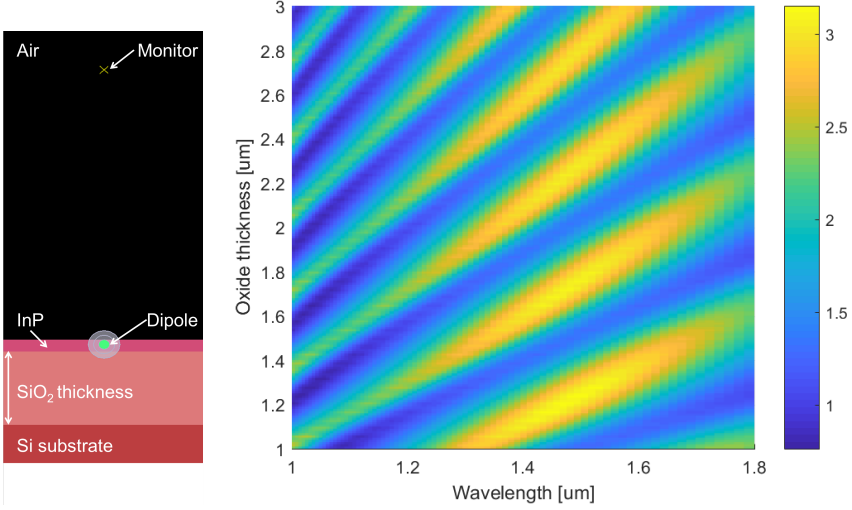


Figure 2.5: Simulating the dipole emission from an InP membrane with varying thickness of buried oxide below. Left: The simulation setup with the green dipole embedded in the InP membrane and the time monitor as the yellow cross. Right: The spectra at different oxide thicknesses. Clear peaks and dips can be seen due to interference effects. The colorbar shows $|E|$.

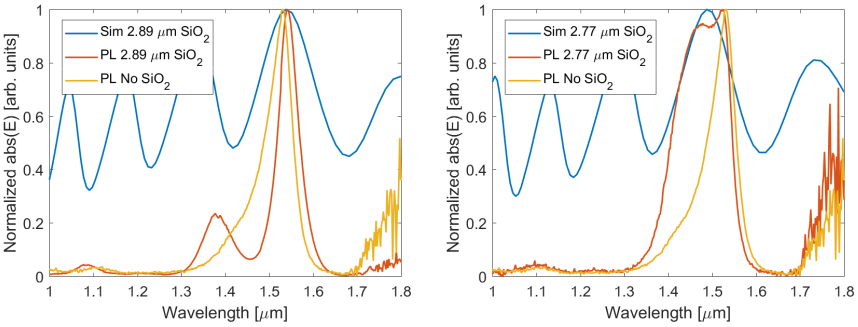


Figure 2.6: Comparison between FDTD obtained spectra and PL measurements on samples with different oxide thicknesses. Left: A sample with an oxide thickness of 2.89 μm, where the interference from the oxide layer modulates the PL signal. Right: A sample with an oxide thickness of 2.77 μm, where the interference peak overlaps better with the PL peak and no splitting occurs.

through the gain medium once, for which the amount of absorbed light in the quantum dots or wells is minuscule [102, 112]. For these reasons, the efficiency of converting pump power to output power collected by the microscope is poor ($\approx 10^{-6}$), and it takes milliwatts of pumping power to collect nanowatts of laser signal power. The pumping efficiency can be increased if the photonic crystal has a mode located at the pump wavelength [113]. Additional efficiency could be achieved if the devices could be pumped by in-plane light, and also if the light from the laser could be collected in-plane. The devices fabricated by NTT [31, 44–50] are on a pure InP platform, and these samples can be cleaved with smooth facets to allow the collection of the in-plane light. For our bonded samples, the difference in lattice constants between Si and InP results in defects and cracks along the surface of the membrane when the samples are cleaved. Thus, another method is necessary for the collection of the in-plane light. With gain material embedded everywhere in the membrane, waveguides are not practical due to absorption in the unpumped areas. The addition of the BH allows integration of waveguides but also grating couplers. With grating couplers, a horizontal scheme for pumping the gain material and collecting the light can be implemented. Horizontal pumping and collection of light are beyond the scope of this thesis. It should be noted that vertical pumping of the gain material and vertical collection of the laser light can be very useful when doing systematic investigations. Without any additional waveguides and couplers, the cavities are isolated and have very small footprints, which allows for fast measurements of many individual lasers.

2.4 Laser characterization setup

The setup used for characterizing active photonic crystal devices can be seen in figure 2.7. The setup was already established at the beginning of the PhD project. The samples are placed under an optical microscope used for both pumping the active material and

collecting the scattered light. The optical setup can be summarized as

1. A 300 mW fiber-coupled pump diode at 1480 nm is used to pump the sample.
2. The pump first goes through an attenuator, allowing us to sweep the input powers.
3. Then the polarization of the pump is rotated to align well with the sample.
4. The pump goes through a Wavelength Division Multiplexer (WDM), needed to filter the sample light from the pump light at a later step. The WDM has three ports; **Port 1** carries the pump light at 1480 nm; **Port 2** carries the pump light as well as the reflected pump light and the signal laser light; **Port 3** only carries light above 1500 nm, and thus the pump is filtered from the signal.
5. After the WDM, the pump is coupled to free space with a commercial collimation package, the beam is resized and focused onto the sample through the microscope with a 50x magnification objective with a numerical aperture of 0.65.
6. The scattered light from the PhC laser is collected with the microscope objective and is coupled back into the fiber with the collimation package.
7. At the WDM the signal light is reflected into port three with a large extinction of the pump before it is collected in the optical spectrum analyzer (OSA)⁶.

The pump spot on the sample (with the 50x, 0.65 NA objective) can be estimated⁷ to be no smaller than $\approx 3 \mu\text{m}$. It can be made larger by defocusing, but this can affect the collection efficiency. With a photonic crystal period of $\approx 500 \text{ nm}$, most lasers (longer

⁶Yokogawa AQ6370

⁷For instance, using the Topticalc tool for Gaussian beams through the objective.
<https://www.toptica.com/products/wavemeters-laser-diodes/topticalc/>

than L5) are then similar in size or larger than the pump spot. Further, the photon flux is not uniform across the pump spot. As such, the pumping efficiency is crucially dependent on the positioning of the pump spot on the sample, or specifically the position of the objective above the sample.

The actual pump power can be found by multiplying the total pump power with some ratio, Γ_{exc} , between the total pump spot area and the gain media that contributes to the lasing mode [77]. For samples with quantum dots embedded everywhere, the dots that have a good overlap with the lasing mode volume contribute most efficiently to the lasing [114]. Thus, Γ_{exc} can be found as the ratio between the total pump spot area and the lasing mode in-plane area. A simpler approximation just uses the cavity area [77]. For the samples with BH, Γ_{exc} can be defined as the ratio between the total pump spot area and the in-plane BH area. For cavities shorter than the pump beam diameter Γ_{exc} can be found as $\Gamma_{exc} = (L_{cav} W_{cav}) / (\pi P_r^2)$, where L_{cav} (W_{cav}) is the length (width) of the cavity and P_r is the radius of the pump beam. For constant pump size, this ratio then increases with cavity length until the cavity length equals the pump beam diameter. With a photonic crystal period of 440 nm, a hole radius of 100 nm and a pump beam radius of 2 μ m the ratio for an L7 cavity is $\Gamma_{exc} = 14\%$. For cavities longer than the pump spot only part of the gain material will be pumped by the pump laser directly, which can additionally lower the efficiency. Finally, the vertical absorption Γ_{abs} , is important in determining the total pump power, which for 3 QW devices is only a few percent [102, 112]. Thus, it can be estimated that less than half a percent of the energy from the pump laser is eventually absorbed in the gain material.

The light scattered from the cavity spreads in all directions, but it does not scatter equally from everywhere in the photonic crystal. Specifically, more scattering can be expected at the mirrors where the field overlaps with additional holes. As the scattered light is collected by the same objective, the collection efficiency is also dependent on the spatial position of the objective in relation to the sample. It is not necessarily the case that these two efficiencies

are optimum for the same positioning of the objective. Thus the maximum output power will be measured when the combined efficiencies observe an optimum. During the PhD project, a piezo stage was installed, which led to better reproducibility and made it easier to achieve maximum output powers from the samples.

Previously, the setup was also used in a cross port mode⁸ with a 980 nm pump diode [101]. The larger difference in wavelength between the pump and signal allows for better filtering of the pump power. However, the 980 nm laser signal heats the sample more and therefore needs to be pulsed. For the devices analysed in this project, using the CW pump always achieved higher device output power than the pulsed pump. Using the cross port mode with the 1480 nm diode was also investigated to determine if the optimum pump and collection positions could simultaneously be reached. However, for all measurements with the cross port mode, the achieved output powers were less than for the single port mode.

Very few samples were burned during the PhD project, which hints that the samples could be pumped harder. Looking at experimental input-output curves, where the output power keeps increasing as the pump power increases, at least up to our maximum pump capabilities also indicates the samples can be pumped harder. For newer samples having active material only in the cavity, and therefore less absorption of pump light everywhere else, it may be possible to pump even harder.

Finally, it should be noted, that the 1480 nm pump diode has many modes around 1480 nm spaced at 33.6 GHz to provide the maximum of 300 mW output power. Beating between the modes cause interferometric noise that introduce modulation sidebands to the peaks of the measured nanolasers. For most nanolasers, the sidebands appear when the peak power is above -50 dBm, and additional sidebands has been observed when the peak power is above -40 dBm.

⁸Different microscope ports used for the pump and collection beams.

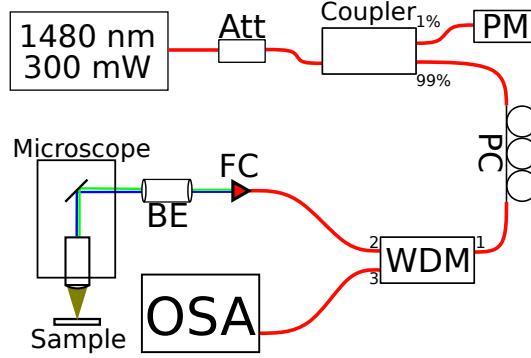


Figure 2.7: Setup for characterization of active samples. Att: attenuator, PM: Power meter, PC: Polarization controller, WDM: wavelength division multiplexer, FC: Fiber Collimator, BE: Beam expander and OSA: Optical Spectrum Analyzer. Red connections denote single-mode fibers while the blue and green beams represent the two different wavelengths of the pump and the signal.

2.4.1 Experimentally determining the threshold pump power

The threshold pump power is a key characteristic of the laser. All the devices fabricated and characterised in this work have $\beta < 0.1$, for which a clear transition can be observed in the input-output curves when the samples begin lasing. Several different methods exist to determine the threshold pump power from an experimental input-output curve with a kink at threshold. The simplest is a linear fit to data points above the threshold, and tracing it back to zero yields the threshold power. This tends to underestimate the threshold power as it assumes zero output below the threshold. A slightly better approach includes a second linear fit to data points below the threshold, and the intersection of the two lines yields the threshold power. This approach has two caveats; first, the transition at threshold must be abrupt, and more importantly, it requires sufficient optical signal below threshold. For the setup used here, where scattered light is collected from the cavity, the measured powers when pumping below the threshold are below or very close to the detection limit of the OSA, and the line is

essentially flat. Finally, it is possible to determine the threshold from the first or second derivative of the input-output curve. Of these two, the second derivative yields the most accurate result [115]. The method used here when finding the threshold is similar to the method outlined by Woodham in [116]. The second derivative has a maximum when the change in the slope of the input-output curve is maximum. A quadratic function is fitted to the points closest to the maximum of the second derivative to compensate for limited resolution when sweeping the input power. The threshold is then found as the input power at the maximum of this quadratic function.

2.4.2 Radio frequency measurements of self-pulsing

The original photonic crystal Fano laser samples with quantum dots embedded everywhere showed self-pulsing under certain conditions [95]. This self-pulsing can be measured using a fast photodetector and an RF spectrum analyzer. As the self-pulsing is predicted to vanish for samples without any active material in the Fano nanocavity [95, 96], it is important to experimentally verify this behaviour for samples with BH only in the LD cavity area.

To investigate the self-pulsing an RF spectrum analyzer⁹ is used to analyse the laser signal generated when pumping with the setup for laser threshold characterization. Before sending the signal to the RF analyzer, a few additions to the setup are necessary, see figure 2.8. First, the maximum output powers of samples measured during the PhD project all fall below -35 dBm. The best resolution from the RF analyzer is obtained for powers from 0 dBm to 3 dBm¹⁰ and thus the signal must first be amplified. Instead of going straight from the WDM to the OSA, the signal is thus amplified by a low noise erbium-doped fiber pre-amplifier¹¹. The amplified signal is filtered¹² and using a 10 dB coupler 10%

⁹HP 70000 system with a 22 GHz bandwidth

¹⁰From the HP 70000 system manual.

¹¹Amonics AEDFA-L-PA-35-B-FA.

¹²Santec OTF-350 bandpass filter

of the signal is sent to the OSA, and the remaining 90% to the RF analyzer. The OSA is kept in the setup to continue monitoring the spectrum of the laser after amplification and the bandpass filter position. It should be noted that the Amonics amplifier requires input powers larger than -40 dBm. Otherwise, an additional in-line erbium-doped fiber amplifier and bandpass filter must be used.

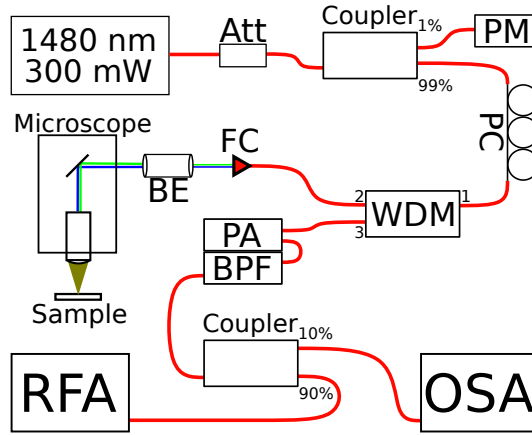


Figure 2.8: Setup for RF characterization of active samples. Att: attenuator, PM: Power meter, PC: Polarization controller, WDM: wavelength division multiplexer, FC: Fiber Collimator, BE: Beam expander, PA: Pre-amplifier, BPF: Band-pass filter, RFA: Radio Frequency Analyzer and OSA: Optical Spectrum Analyzer. Red connections denote single-mode fibers while the blue and green beams represent the two different wavelengths of the pump and the signal.

It should also be noted that the modulation sidebands caused by the beating between pump diode modes are outside the bandwidth of the RF spectrum analyzer, so if the nanolasers signals are CW, the RF spectrum is expected to be flat and featureless.

For CW lasers the fluctuations in the output intensity from a laser is also an important device characteristic. For macroscopic lasers, the relative intensity noise, (RIN) of lasers can be measured using the same setup. For nanolasers, however, the output power is typically too low to distinguish the RIN from the noise floor, and

other methods must be used. It has recently been proposed to use the low power nanolaser as a master oscillator for a macroscopic low noise laser [117] serving as a slave laser. The intensity noise fluctuations are then transferred from the low-power nanolaser to the macroscopic laser. It has also been demonstrated that a heterodyne detection scheme can be used in conjunction with machine learning to determine the RIN of low power lasers [118–120].

2.5 Setup for measuring the Q-factor

During the project, it became clear that the quality of the holes in the fabricated samples was not optimal. Thus the fabricated samples could very possibly have a much lower Q-factor than what was anticipated from FDTD simulations. Passive devices¹³ were fabricated with the same process in order to determine the quality of the cavities. The author built the setup based on the cross-polarization resonant scattering method described first by McCutcheon in [121]. The method utilizes the polarization of the modes in the photonic crystal cavity and a polarizing beamsplitter so the resonant excitation light can be filtered from the signal. The excitation light must be linearly polarized, or at least be filtered at the cost of input power. The best excitation of the mode is obtained when the excitation light polarization is the same as that of the photonic crystal mode. In this configuration, however, the signal can not be filtered from the excitation light. Instead, the polarization state of the excitation light is aligned to the 45° angle of the photonic crystal cavity. In this way, the excitation beam can still couple to the photonic crystal modes. The scattered light from the cavity mode is then a mix of two linear polarizations. The polarizing beamsplitter then filters out almost all the reflected excitation light. As the signal has a mixed polarization, the part of it that is aligned with the reflected excitation light is also filtered

¹³Q-factors of active devices can also be accurately measured if the gain media is pumped to transparency.

in the polarizing beamsplitter, which results in a loss in signal power. Figure 2.9 shows the setup as it is in our lab. Since the first demonstration of this method, similar setups have been used by other groups to investigate the Q-factor of photonic crystal devices similar to the ones fabricated in this project [122–124].

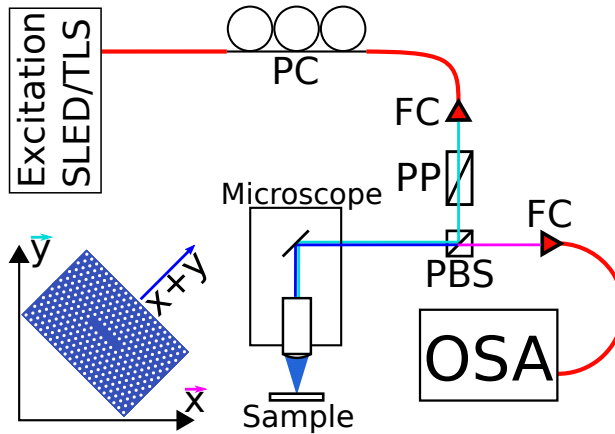


Figure 2.9: Setup for measuring quality factors of passive cavities. PC: Polarization controller, FC: Fiber Collimator, PP: Polarizing Prism, PBS: Polarizing Beam Splitter and OSA: Optical Spectrum Analyzer. Red connections denote single-mode fibers while the magenta (x) and cyan (y) beams represent the two orthogonal polarizations reflected or transmitted in the PBS. The inset shows the polarization orientation with respect to a line defect cavity. The cavity mode is a combination of x- and y-polarization.

The most crucial part of the setup is the polarization beamsplitter, specifically its extinction ratio between the two polarizations. The cube used in the current setup has an extinction ratio of $\approx 1000 : 1$ in the transmitted light, but the setup could benefit greatly of incorporating a beamsplitter with a larger extinction ratio. Secondly, the excitation light source must be considered. The easiest method uses a broadband light source such as the expensive supercontinuum source, or the more affordable superluminescent diode (SLED). The sample can then be positioned under the microscope, and an OSA can be used for the collection

of light. In this mode, the measurable Q-factors are limited by the resolution of the OSA. In order to determine the FWHM, it is reasonable to require at least three points to resolve a peak, and thus, with a resolution limit of 0.02 nm the maximum Q-factor that can be measured is ≈ 30000 .

Another option is to use a narrow linewidth tunable light source (TLS), in which case the Q-factor is instead limited by the step size of the light source. The TLS enables the measurement of higher Q-factor samples. A wavelength sweep across a bandwidth wide enough to find the peaks with a stepsize small enough to resolve the peaks is slow in the TLS, and a full sweep must be carried out between sample adjustments until the resonance appears on the OSA. This makes the initial alignment of the excitation beam to the photonic crystal cavity harder using the TLS. Therefore, the optimum solution is to use the SLED for initial positioning of the excitation beam on the sample. Then the TLS is used to do the final measurement in a much smaller wavelength range with a high resolution.

Even with this method, it is not an easy task to perform a proper measurement on a high Q-factor cavity. As the quality factor increases, the amount of light scattering from the cavity decreases. For a cavity with both high and low Q-factor modes, the low Q-factor modes are more easily excited.

For low Q-factors, signals have been measured with a signal-to-noise ratio (SNR) close to 30 dB¹⁴. However, as the Q-factor increases, the signal drops and the very high Q-factor modes can be extremely difficult to excite and subsequently measure. With a 1000:1 selectivity between polarizations in the beamsplitter, the system is no longer limited by the beamsplitter if the SNR drops below 30 dB. To increase the SNR when measuring higher Q-factor cavities the only cure is to increase the input power. In this situation the TLS available to us¹⁵ outperforms the SLED as it simply

¹⁴Similar to the polarizing beam splitter extinction ratio.

¹⁵Ando AQ4321A Tunable Laser.

provides more power, so even for low Q-factor cavities, the best result may be obtained using the TLS for the final measurement.

A beamsplitter in the microscope is necessary to transmit light to an IR camera used to align the pump on the sample. The beamsplitters available to us however, cause an interference pattern in the signal. The best performance of the system is obtained using a 90:10 beamsplitter with a 1400 nm low pass filter. With this beam splitter it is possible to measure Q-factors of cavities and in chapter 4 an initial measurement is presented where a Q-factor of 600 is measured.

CHAPTER 3

MODELLING PHOTONIC CRYSTAL NANOLASERS

Throughout the project, experimental results have been analysed with fits from a laser rate equation model. This model is presented in the first section of this chapter. An automatic fitting tool was developed to fit the laser rate equations to experimental data. This fitting tool uses a particle swarm approach to create input/output curves for many different parameter values and then compares them to the experimental results. For this approach to be computationally efficient, one must assume a linear relationship between the material gain and the carrier density in the rate equation model. The validity of this model is also analysed. Finally, the necessity of bounding parameter values used in the model is discussed.

The second section gives a general introduction to how FDTD simulations in the commercial software Lumerical have been set up and used throughout the project. It introduces the general setup used for most of the simulations in this thesis, and discuss the caveats and limitations, to facilitate reproduction of the numerical results presented in the thesis.

3.1 A rate equation model

The rate equation model is a standard model described in [111] and used in [31]. The rate of change for the carrier, N , and photon,

N_p , density can be described by the sum of rates into, minus the sum of rates out of the respective reservoirs. Each generation and loss term is related to physical processes. Thus, the model can provide useful insights into how the laser functions, and how the physical parameters influence the laser characteristics.

$$\frac{dN}{dt} = \frac{\eta_i P_i}{h\nu V} - \left(\frac{N}{\tau_r} + \frac{N}{\tau_{nr}} \right) - v_g g N_p, \quad (3.1a)$$

$$\frac{dN_p}{dt} = \left[\Gamma v_g g - \frac{1}{\tau_p} \right] N_p + \Gamma \beta \frac{N}{\tau_r}. \quad (3.1b)$$

The generation of carriers by optical pumping can be described by the pumping power, P_i , the energy, $h\nu$, of the pumping photons, the volume of the active area, V , and the injection efficiency, η_i , that describes the fraction of injected photons which successfully create carriers in the active region. As discussed in section 2.4, the pump power from the fiber laser in our setup P_{exc} can be multiplied with the ratios Γ_{exc} and Γ_{abs} to determine the power P_i absorbed in the gain region [77]. The carrier recombination processes are described by effective lifetime approximations so decay can be described by the carrier density and a decay time. For instance the spontaneous recombination rate of carriers, R_{sp} can be described by $R_{sp} = N/\tau_r$. Carriers are then lost by spontaneous emission, N/τ_r , non-radiative emission, N/τ_{nr} , and stimulated emission $v_g g N_p$. The stimulated emission is given by the product of the group velocity of the photons in the medium, v_g , the gain, g , which will be further addressed below and the photon density N_p . For the photon density, the creation terms are from stimulated, $\Gamma v_g g N_p$, and spontaneous emission into the mode $\Gamma \beta N/\tau_r$, where $\Gamma = V/V_p$, is the confinement factor, i.e. the ratio between the active volume and the volume occupied by the photons (mode volume). The β -factor describes the fraction of spontaneous emission that contributes photons to the lasing mode. The β -factor for our photonic crystal nanolasers is larger than macroscopic semiconductor laser, but is still below $\beta = 0.1$ and thus, much smaller than unity. The loss of photons in the cavity is described by the

lifetime τ_p which is related to the losses of the mirrors, α_m , the average internal cavity loss, $\langle\alpha_i\rangle$, as well as the angular frequency of the lasing mode, ω , and the cavity quality factor, Q , through $1/\tau_p = v_g(\alpha_m + \langle\alpha_i\rangle) = \omega/Q$. Under a constant input power, the carrier and photon densities will eventually assume a steady state. The ultimate purpose of the model is to generate input/output curves that can be compared to experiments, and for this, the rate equations are solved in steady-state. Before looking at the steady-state solutions, the gain model is discussed.

3.1.1 Linear or logarithmic gain model

The gain of quantum dots and quantum wells can be described by a logarithmic model [31, 111] where the material gain is given by

$$g(N) = g_0 \ln\left(\frac{N}{N_{tr}}\right), \quad (3.2)$$

where N_{tr} is the transparency carrier density, describing the carrier density needed for the gain material to appear transparent to an incoming electric field. The logarithmic gain model is used for bulk materials, quantum wells and quantum dot gain materials alike. For bulk materials, an additional linearity parameter must be added [111], but for quantum wells with reduced dimensionality the logarithmic model effectively describes the carrier-gain relationship¹. As the dimensionality is further reduced for quantum dots, the density of states change as described in section 1.3. To the authors knowledge, the logarithmic model for the gain of quantum dots has not yet been experimentally shown describe the carrier-gain relationship. However, the rate equations with the logarithmic gain model do not have an analytical solution and require a numerical solver, e.g. MATLAB, to obtain a solution. When fitting multiple experimental input/output curves with a broad parameter range, the numerical solvers must be run many times which quickly becomes computationally heavy. Therefore,

¹See section 4.6 in [111]

a simpler approximation² with linear gain is applied, for which the coupled equations in the steady-state reduce to a second-order equation for the carrier density and a first-order equation for the photon density. The linear gain model describes the gain as

$$g(N) \approx \frac{g_0}{N_{tr}}(N - N_{tr}). \quad (3.3)$$

The approximation of linear gain in this format is only valid close to the evaluation point of the Taylor expansion, i.e. if the threshold carrier density is close to the transparency carrier density. When the model was applied to the data in chapter 4, this assumption was accepted. However, the carrier density at threshold was later found to be much larger than the transparency carrier density. As the model has so many free/unknown parameters and only two governing equations, the obtained fits are not unique. An error in the estimated gain from a faulty assumption in the gain model will be absorbed into the other parameters in order to still obtain a good fit. In order to investigate the variation of a single or a few parameters across different cavities, the remaining parameters in the model must be fixed. However, many of the material parameters are not known to us. The unknown parameters can be fixed to values found in the literature. However, that is not always possible if there are no articles published on similar systems. Secondly, the parameters found in the literature could be incorrect or not directly transferable to our system. An error could then be made when defining, e.g. the transparency carrier density and the gain coefficient g_0 , which affects the fitted parameters. Thus, the parameters of the extracted fit may still be used when investigating systematic variations that affect only one or few physical parameters individually, such as in chapter 4, where the Q-factors are varied while material parameters should remain constant across devices. For future use of the autofitting tool, the author would, however, recommend incorporating an iterative approach to the evaluation point of the Taylor expansion. The carrier

²Taylor approximation to the first order of $\ln N/N_{tr} \approx N/N_{tr} - 1$, evaluated at $N = N_{tr}$.

density at the threshold, N_{th} , which can be calculated by eq. (3.10) and the experimentally determined threshold pump power can be used as the first evaluation point of the Taylor approximation, i.e. $N_0 = N_{th}/N_{tr}$ to define the linear gain as

$$g(N) \approx g_0 \left(\ln \frac{N_{th}}{N_{tr}} + \frac{1}{N_{th}} (N - N_{th}) \right). \quad (3.4)$$

With this, the gain is still linearly dependent on N , and short computation time can be achieved. The two models can be compared, and the evaluation point N_0 can be iteratively changed until a reasonable agreement is met. The gain of the three models for the parameters extracted in chapter 4 can be seen in figure 3.1 for carrier densities corresponding to experimental input powers³. It should be noted that the carrier density is calculated using the linear gain model at $N_0 = N/N_{tr}$. Finally, it should be noted that the carrier density for the minimum experimental input power is still above N_{tr} and the material gain is always positive.

The figure shows the significant difference in absolute material gain between the linear model at $N_0 = N/N_{tr}$ and the logarithmic model, note the difference in scale on the two y-axes. Secondly, the linear model at $N_0 = N_{th}/N_{tr}$ is found to be in good agreement with the logarithmic model for carrier densities close to N_{th} , and, as the carrier density clamps above the threshold the approximation remains suitable for input powers above the threshold.

Thus, for comparison with experimental results, where low output powers are neglected from the fit, the linear model evaluated at N_{th}/N_{tr} , may be sufficient without taking an iterative approach. Further investigations would be necessary to conclude if the model is sufficient, but it would also benefit from more reliable measurements on the gain material. It should be noted, that without such investigations it is also not clear if the logarithmic model is accurate for the gain material used in this project. As mentioned above, an error in the fixed value of one parameter will

³The input power measured by a power meter below the objective, and not modified by Γ_{exc} and Γ_{abs} as described in section 2.4

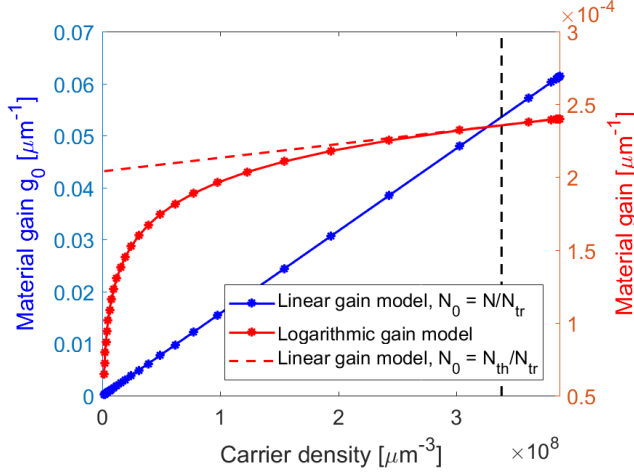


Figure 3.1: The three different models for the material gain $g(N)$, for carrier densities N corresponding to the input power of measurements in chapter 4. The blue and red color of the graphs correspond to the left and right axis respectively. The vertical dashed black line indicate the threshold carrier density N_{th} .

result in the error of one of the free parameter values determined from a fit. Specifically, a very large material gain calculated with the first linear model will be compensated by the gain coefficient, g_0 , becoming very small.

Steady state solutions

The derivation of the steady-state solutions, where $dN/dt = 0$ and $dN_p/dt = 0$, follows next. The derivations presented here uses the simple linear gain model of eq. (3.3), evaluated at $N_0 = N/N_{tr}$, but it is straightforward to exchange it with the gain model in eq. (3.4), evaluated at $N_0 = N_{th}/N_{tr}$. The two rate equations become

$$0 = \frac{\eta_i P_i}{h\nu V} - \left(\frac{1}{\tau_r} + \frac{1}{\tau_{nr}} \right) N - v_g \frac{g_0}{N_{tr}} (N - N_{tr}) N_p, \quad (3.5a)$$

$$0 = \Gamma v_g \frac{g_0}{N_{tr}} (N - N_{tr}) N_p - \frac{1}{\tau_p} N_p + \Gamma \beta \frac{N}{\tau_r}. \quad (3.5b)$$

Dividing the second equation by Γ and adding the two equations gives the equation for the photon density as

$$N_p = \tau_p \Gamma \left[\frac{\eta_i P_i}{h\nu V} - N \left(\frac{1 - \beta}{\tau_r} + \frac{1}{\tau_{nr}} \right) \right]. \quad (3.6)$$

This equation can be inserted into eq. (3.5a) to give the second-order equation

$$AN^2 + BN + C = 0, \quad (3.7a)$$

with

$$A = \left[\frac{v_g g_0 \tau_p \Gamma}{N_{tr}} \left(\frac{1 - \beta}{\tau_r} + \frac{1}{\tau_{nr}} \right) \right], \quad (3.7b)$$

$$B = \left[- \left(\frac{1}{\tau_r} + \frac{1}{\tau_{nr}} \right) - \frac{v_g g_0 \tau_p \Gamma \eta_i P_i}{N_{tr} h\nu V} - v_g g_0 \tau_p \Gamma \left(\frac{1 - \beta}{\tau_r} + \frac{1}{\tau_{nr}} \right) \right], \quad (3.7c)$$

$$C = \frac{\eta_i P_i}{h\nu V} + v_g g_0 \tau_p \Gamma \frac{\eta_i P_i}{h\nu V}. \quad (3.7d)$$

Finally, from the photon density, the output power of the optical mode P_0 and the spontaneous emission P_{sp} can be calculated as

$$P_0 = \eta_0 h\nu \frac{N_p V_p}{\tau_p}, \quad P_{sp} = h\nu V \frac{N}{\tau_r}, \quad (3.8)$$

where η_0 is the optical efficiency. The optical efficiency is defined as $\eta_0 = F\alpha_m / (\alpha_m + \langle \alpha_i \rangle)$, where α_m denotes the mirror loss, $\langle \alpha_i \rangle$ denotes the average internal loss and F denotes the fraction of

power that is coupled out of the cavity in the desired direction⁴. In this treatment, where we collect light out-of-plane with a microscope objective, F also includes the collection efficiency of the microscope objective. The spontaneous emission power, P_{sp} , below the threshold can not be resolved in our experimental setup at the moment. Furthermore, above threshold $P_0 \gg P_{sp}$ and P_{sp} in eq. (3.8) is neglected when generating input-output curves to fit experiments.

3.1.2 The threshold pump power

Lastly, our focus turns to the threshold power of the laser, which is defined as the point where the gain exactly equals cavity losses. When pumping above this point, the excited carriers are immediately consumed by stimulated photons and the spontaneous emission power is clamped at its threshold value. For lasers with small β -factors, the photon density below the threshold is very low, and it is often a reasonable approximation to use $N_p \approx 0$. Then eq. (3.1a) in the steady-state reduce to

$$\frac{\eta_i P_i}{h\nu V} = \left(\frac{1}{\tau_r} + \frac{1}{\tau_{nr}} \right) N. \quad (3.9)$$

At the threshold, $N = N_{th}$ and the threshold power can be found as

$$P_{th} = \frac{h\nu V}{\eta_i} \left(\frac{1}{\tau_r} + \frac{1}{\tau_{nr}} \right) N_{th}. \quad (3.10)$$

Using the linear gain model and that, at the threshold, the modal gain exactly equals cavity losses, we have

$$\Gamma g_{th} = \Gamma \frac{g_0}{N_{tr}} (N_{th} - N_{tr}) = \frac{1}{\tau_p \nu_g}. \quad (3.11)$$

⁴For 1D Fabry-Perot cavities with imperfect mirrors, light escapes from both ends but is typically only collected in one.

Isolating N_{th} in the above equation and inserting in eq. (3.10) the threshold power is finally found as

$$P_{th} = \frac{h\nu V}{\eta_i} \left(\frac{1}{\tau_r} + \frac{1}{\tau_{nr}} \right) \left(\frac{N_{tr}}{\tau_p \Gamma v_g g_0} + N_{tr} \right). \quad (3.12)$$

The threshold pump power can be determined from experimental input/output curves using the method described in section 2.4.1. The above expression is used to improve the automatic fitting tool by discarding parameter combinations where the threshold power calculated by eq. (3.12) is not in agreement with the experimental result before any laser rate equation is even solved.

3.1.3 Bounding parameters to reasonable ranges

As mentioned above, with many more parameters than equations to describe them, a unique fit is not obtained, when applying the rate equation model to experimental data. On a positive note, some parameters affect the input/output curves in vastly different ways than others, and this can be used to separate some parameters from others.

When faced with experimental input/output curves where some systematic investigations are carried out, and specific parameters are expected to change, it will, therefore, be necessary to limit the remaining parameters in a narrow range or even fix them. This is preferably done to values measured on the sample, values estimated from simulations, or values from published articles on similar devices.

3.2 FDTD simulations of passive cavities

The commercial software Lumerical has been used for Finite Difference Time Domain (FDTD) simulations as a tool to determine the resonance of a given photonic crystal cavity before fabrication, the effect of a buried heterostructure in the InP membrane, cf. chapter 5, or the effect of the oxide thickness cf. section 2.3.

This section focus on the standard setup for simulations of photonic crystal cavities, while the addition of the BH is discussed in chapter 5.

A typical simulation setup can be seen in figure 3.2. Both 2D and 3D simulations can be carried out, where the 2D simulation requires much less computational power. However, the Q factor from a 2D simulation neglects the out of plane scattering, which is a significant limitation on the Q factor of photonic crystal cavities. Furthermore, all the resonance frequencies are shifted, making a comparison with experiments difficult. Thus, simulations in this thesis are performed in 3D, unless specifically stated. The description is separated into its components: InP membrane, excitation source, mesh settings, FDTD settings, Q-analysis and profile monitors. As the simulations are primarily used as a design tool for fabricating samples, the individual simulations are often performed using specific sample parameters.

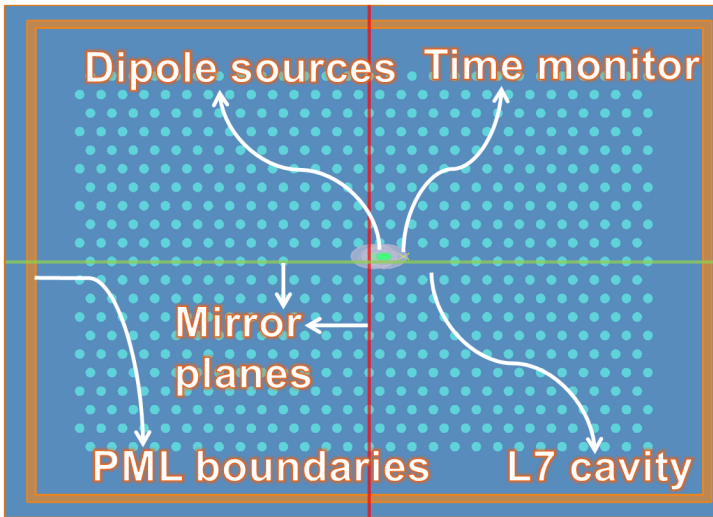


Figure 3.2: Setup of a typical FDTD simulation for photonic crystal cavity seen from the top.

InP membrane & photonic crystal

The InP membrane is generally defined with thickness ≈ 250 nm, which is slightly larger than $0.5a$, for which the fundamental mode is ell confined [57]. The membrane thickness of a given sample can be probed by ellipsometry and used when comparing to experimental results, or designing the cavity resonance. The membrane is defined with a wavelength-independent purely real refractive index, i.e. no absorption is included. Though the refractive index varies from 3.17 to 3.16 in the wavelength range from 1500 nm to 1600 nm [125] the refractive index is fixed at $n = 3.17$. The airholes are defined by extruding circles through the membrane with refractive index $n = 1$. The photonic crystal period can be varied to change the bandgap of the photonic crystal structure as described in section 1.3, but for all samples with quantum dots embedded in the entire membrane the period is $a = 438$ nm. The radius of the holes is then varied to find the value that provides good overlap between the cavity resonance and the PL peak of the sample. See figure 3.3, where a 253 nm thick InP membrane was simulated to find the corresponding radius, 112 nm, that had the best overlap with the PL peak centered at 1570 nm.

Excitation source

The cavity modes are TE-like and magnetic dipoles with dipole moments oriented out-of-plane can excite these modes. The dipoles are placed in the center of the membrane, $z = 0$ and placed off-centre in the x - and y -directions. Even when placing the dipole off-centre, there is still a possibility of poor overlap with the optical mode in the cavity. For this reason, multiple spatially offset dipoles are used, often two is enough. The dipoles are broadband with a center frequency at 205 THz. Other excitation sources are also available in Lumerical, such as Gaussian beams and plane waves, but the simplicity of the dipole makes it attractive. Ultimately, the number and type of sources must simply be chosen such that the modes of interest are excited.

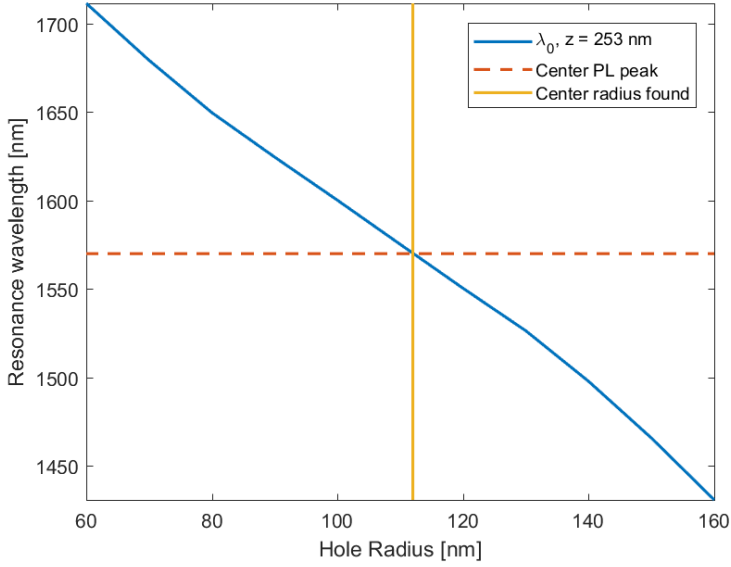


Figure 3.3: Resonance frequency of an L7 photonic crystal cavity with a period of $a = 438$ nm, in a 253 nm thick InP membrane as the hole radius is varied from 60 nm to 120 nm. The horizontal line indicates the peak of the measured PL spectra from the given sample, while the vertical line shows the required hole size for devices with resonances in this range.

Mesh settings

Certain conditions must be applied to the mesh of the simulation for consistent results. Most importantly, the mesh should be centred around the cavity center, and have an integer number of mesh points within a period of the photonic crystal. This serves to resolve all holes identically, at least until individual holes are shifted for optimisations. For convergence, in this case, the mesh resolution should be good enough to still resolve the shifted holes equally as all others. When the endholes are moved in chapter 4, this is done in steps of 2.5% of the photonic crystal period. Thus the mesh resolution needed to resolve all holes equally must be at least $MR = a/\Delta x_{mesh} = 40$.

With a standard line defect cavity the required mesh resolution for convergence is very high, see tables 4 and 6 in [126], but for comparison between simulations, for instance, when doing parameter sweeps, complete convergence is not always necessary. Simulations with lower mesh resolution can be run faster and can still give a good initial insight. Secondly, when using the FDTD as a tool to find the right photonic crystal parameters for a given resonance wavelength, the variations in fabrication is often greater than the shift in resonance wavelength between an almost converged simulation and a completely converged simulation. Most simulations are therefore carried out with a mesh resolution $MR = 12$.

FDTD region settings

Most of the simulation parameters, e.g. the boundary conditions and simulation time, are defined with the FDTD region. For analysis of the Q-factor of cavities, it is important to run the simulation sufficiently long to determine the exponential decay of the modes without interference from the source excitation at $t = 0$. Furthermore, the spectrum found from the simulation is calculated by a Fourier transform of the time signal. Thus, the longer the simulation, the better the resolution of the spectra. For most applications a simulation time of 15 ps was found to be sufficient,

though in cases where an improved resolution was needed, this was increased. Secondly, the perfectly matched layers (PMLs)⁵ are always used as boundary conditions. These serve to minimise reflections at the end of the simulation domain. As the number of layers is increased, reflections at the boundaries are minimised. However, the increase in layers come at a computational cost. Thus, eight layers are often sufficient, but if reflections occur, the layer number has been increased to 16 layers. For efficient simulations, the option to extend the structure through the PML is always chosen, at which point Lumerical assumes the geometry and material parameters at the edge of the simulation domain to continue to infinity⁶. The photonic crystal must be terminated before the PML is reached, so the outer holes are not stretched to infinity as this will influence the simulation results. For reproducible results, a good rule of thumb is to always extend the membrane structure without holes for at least two periods before the boundaries.

Symmetry settings

The photonic crystal cavities often have mirror planes through the center of the cavity along and across the cavity, see the red and green lines in figure 3.2. The mirror planes of the structure, in turn, leads to symmetric or anti-symmetric modes of the electromagnetic fields along the same mirror planes. Symmetries can be used to reduce the computational time of simulations significantly. It is important to note that not all modes share the same symmetry conditions; thus, applying symmetry conditions can effectually remove modes from the spectrum. Therefore, a new simulation setup should always be run without any symmetry conditions and the spectrum and field profiles investigated. If this results in a dominant mode that needs to be further investigated under different perturbations, symmetric conditions can be applied to

⁵<https://support.lumerical.com/hc/en-us/articles/360034382674-PML-boundary-conditions-in-FDTD-and-MODE>

⁶<https://support.lumerical.com/hc/en-us/articles/360034382414-Always-extend-structures-through-PML-boundary-conditions>

reduce computational time. Lastly, the modes in the triangular photonic crystal slab are TE-like, and field is confined by total internal reflection in the z -direction [57], and a symmetric boundary condition is always applied.

Q-analysis

The Q-factor analysis is carried out by the built-in Qanalysis group⁷, where one or more time monitors are placed to record the field intensity through the simulation. From the result in the time domain, a Fourier transform gives the spectrum, which is analysed for peaks. The peaks are then treated individually by filtering with a bandpass filter before an inverse Fourier transform gives the time domain signal of only the resonance. Finally, the Q factor is calculated from the exponential decay of the time domain signal of the resonance. For accuracy only the central part of the signal in time is used to avoid any contributions from the excitation source and numerical errors in the ends of the time signal caused by the Fourier transforms⁸. Just as the Q-factor of fabricated devices depend on the number of periods of photonic crystal around the cavity so does the simulated Q-factor. For an L3 cavity, at least 11 rows above and below the cavity must be included before the Q-factor is accurately determined [127].

Profile monitors

2D profile monitors are placed at $z = 0$ to visualise the electromagnetic field in the cavity. Once again, the field at a given frequency is determined from a Fourier transform of the time domain signal. Here it is especially important to exclude the beginning of the simulation, as the source will flood the monitors, compared to the resonant fields. This is done with start apodization⁹, where 3 ps is

⁷For more information, see the Lumerical knowledge base on Q factor calculations, https://apps.lumerical.com/diffractive_optics_cavity_q_calculation.html.

⁸See <https://support.lumerical.com/hc/en-us/articles/360041611774>

⁹<https://support.lumerical.com/hc/en-us/articles/360034902473-Understanding-time-apodization-in-frequency-domain-monitors>

often sufficient to allow the source to decay before monitoring the resonant fields.

That concludes the description of the standard FDTD simulation setup used in the thesis. Lumerical and FDTD simulations, in general, are useful tools in the design process of the photonic crystal devices. If the characterisation of fabricated samples yields unexpected results, FDTD simulations can also offer insights into their origins.

CHAPTER 4

LOWERING THE LASER THRESHOLD BY OPTIMISING THE Q-FACTOR

For on-chip optical interconnects to outperform electrical interconnects, the energy consumption is a key parameter that must be at least as low as 10 fJ/Bit [1, 3], but in general as low as possible. For interconnects with a directly modulated on-chip source, a key laser characteristic then becomes the threshold power. Specifically, the lower the threshold for the nanolaser, the lower the energy consumption required per bit to send an amplitude encoded data signal. Recalling the equation derived in section 3.1.2 the threshold pump power can ultimately be related to the quality factor as

$$P_{th} \propto \frac{1}{\tau_p} \propto \frac{1}{Q}, \quad (4.1)$$

where τ_p is the photon lifetime in the cavity. Thus, designs that increase the Q-factor while keeping other parameters constant should result in a lower threshold power.

This chapter is based on the submission to the SPIE Optics + Optoelectronics conference of 2019 [128], with some newer results added. Specifically, the setup for measuring Q-factors of similar passive cavities had not been established at the time of the conference. A full Q-factor characterisation is still required,

but a preliminary measurement has been made. The work in this chapter was mainly carried out by the author. Design and fabrication, as well as experimental characterisation of the photonic crystal lasers, was done by the author. The model for the mirror phase calculations, based on Lalanne et al. [129], was developed in house by PhD student Thorsten Svend Rasmussen. All cavity simulations were carried out by the author. The simulation of the dispersion relation was initially developed by Thorsten Svend Rasmussen, and adapted by the author to fit the fabricated photonic crystal parameters.

4.1 Increasing the Q-factor by shifting holes

As early as 2003 it was described by Akahane et al. [79], how shifting the first endholes of the inline mirror of a photonic crystal (PhC) line defect cavity can increase the quality factor. The increase in Q-factor is attributed to a less abrupt change in the electromagnetic field at the mirrors. This is termed gentle confinement, where the envelope of the cavity field approaches a smooth Gaussian and can be obtained by shifting the holes in the photonic crystal lattice. Furthermore, it was shown when shifting only one hole [79] and for multiple optimisation rounds with many shifted holes [83], that visualising the leaky components of the field can help determine which holes are primarily responsible for scattering losses. The so-called leaky components for a given cavity mode are found by a Fourier transform of the field profiles and then extracting the components that lie inside the light cone of the cavity mode resonance. Recall from section 1.3 how the light cone is given by $\omega > c|k_{\parallel}|$, then the leaky components for a given resonant mode fulfill $\omega_0 \geq c|k_{\parallel}|$. When doing an inverse Fourier transform of those components, only the part of the field where scattering to radiation modes occurs will be visible, and they can be found to overlap with certain holes, that can then be moved for optimisation. This method is used in chapter 5, where a total of four holes are shifted to optimise the cavity Q-factor.

In this chapter we investigate what effect shifting the first two mirror holes has on a PhC laser. Since 2003, several publications have been made concerning the increase of Q-factors by either shifting holes in space or modifying the radius of holes [80, 83, 84, 123]. The publications, however, are always either based only on simulations or, when experimental, considering passive devices characterised for Q-factor. Here, active devices are fabricated and characterised to investigate how the changes in Q-factor carry over to the measurable threshold powers. Specifically, the threshold powers and the maximum output powers are experimentally determined for photonic crystal lasers with different hole shifts. Secondly, a purely passive sample with equivalent cavities was fabricated for measurements of the cavity Q-factors.

Lastly, FDTD simulations on passive cavities are carried out to investigate the phase change at the photonic crystal mirror, and the penetration depth of the field into the photonic crystal mirror. The photonic crystal mirror is a distributed reflector, and the phase and magnitude of the reflections are coupled. The phase change occurring at the mirror and the penetration depth was previously investigated by Lalanne et al. [129], by comparison with an effective Fabry-Perot model. The Fabry-Perot model suggests that the cavity Q-factor can be influenced by both the penetration depth and the mirror phase [129], which merits a more in-depth look into these two physical quantities. Here, the same methodology is applied to the cavities with the first endholes shifted, to investigate how such a perturbation affects the phase change at the mirror.

4.2 Device overview

All the samples were fabricated following the recipe detailed in section 2.1. The PhC lasers were fabricated in a 250 nm thick InP membrane with three layers of embedded InAs quantum dots, see figure 4.1 top. The InP membrane is BCB bonded to a silica-on-silicon substrate, and the silica is wet etched to create a

free-floating membrane. All the fabricated cavities are made by omitting seven holes in the PhC leading to an L7 line-defect laser. All the fabricated cavities have a lattice constant of $a = 0.438 \mu\text{m}$, and varying hole radii that are determined from SEM images. Samples were fabricated with shifts, $s = (0 - 0.4)a$ in increments of $0.05a$, see figure 4.1 bottom, allowing a systematic investigation of how the laser threshold and output power depends on the hole shift. The equivalent passive cavities are fabricated on a similar sample, except that for the passive sample, the InP membrane is directly bonded on the silica-on-silicon substrate. The passive sample has no buried quantum dots, which allows for characterisation of the Q-factor. A passive L7 cavity without endhole shifts has a numerical Q-factor of around 60000 found with FDTD simulations, which agrees with, e.g. [126].

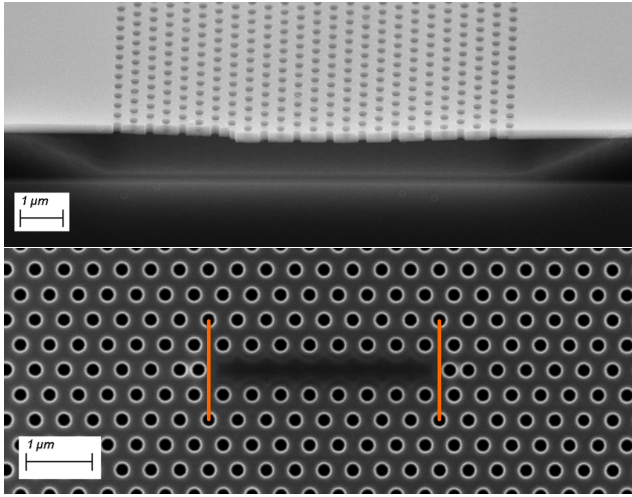


Figure 4.1: SEM images of the active samples. Top: The InP membrane with the embedded quantum dots. Bottom: An L7 cavity with the first endholes shifted by $0.35a$. Radius of the holes is 100 nm. The position of the mirror in the equivalent cavity model is indicated by the orange lines.

Adapted from [128]

4.3 Experimental Characterization

The active sample was characterised using the setup described in section 2.4 and input-output curves obtained to determine the thresholds. The passive sample with equivalent cavities was characterised using the setup described in section 2.5. Two samples were fabricated and measured. Each sample has, by design, two identical sets of groups of hole-shifted photonic crystal lasers with varying radius, in a manner where the radius varies between rows, and the hole shifts vary between columns. However, on one sample, one set had a large number of defects. Of the sets, only a few rows have radii close to the design, and of those rows, some have defective cavities for any given hole shift. In total, five different groups, each with hole shifts from 0-0.4a, was measured.

4.3.1 Threshold powers

Measured input-output curves are shown in linear scale in figure 4.2b and logarithmic scale in figure 4.2a. The onset of lasing, as well as the maximum output power, varies significantly as the endholes are shifted.

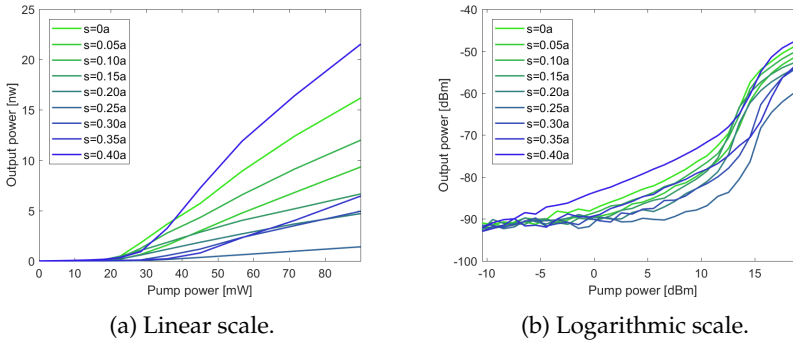


Figure 4.2: Experimental input-output curves measured for the $r_1 = 95.7$ nm group when varying the endhole shifts. The characteristic s-shape of a laser is noticeable in the logarithmic plot. Taken from [128]

From the input-output curves, the threshold levels are determined using the second derivative approach described in section 2.4.1. The threshold powers can be seen in figure 4.3a. Significant fluctuations between the different groups can be seen. Some of these fluctuations might be caused by non-uniform local variations in the PhC. Such variations are results of the limitations in the fabrication process, and the PhC environments for different laser cavities are then not completely identical across a sample.

To investigate the effect of the endhole shifts, it is more instructive to normalise the threshold pump powers within each group to that of the laser with a zero-hole shift. This can be seen in figure 4.3b along with both the mean values across all groups and FDTD simulation results. The simulated curve is obtained by first finding the Q-factors as described in section 3.2, normalising the Q-factors for all shifts to that of the normal L7 cavity and finally taking the inverse according to equation 4.1. This approach assumes that only the Q-factor changes, so all other parameters cancel out when normalising to the normal L7 cavity.

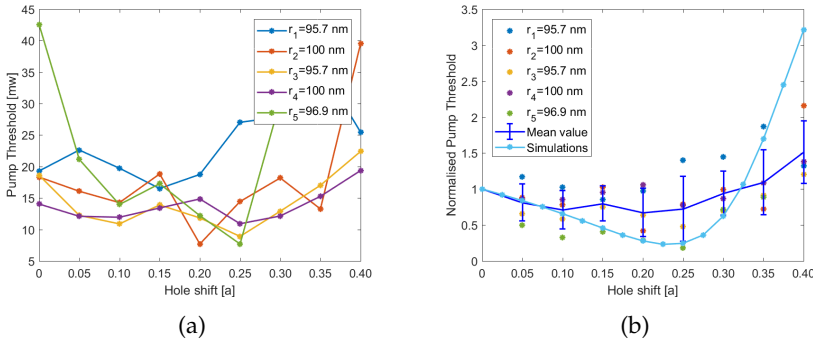


Figure 4.3: (a) Threshold pump powers extracted from the measurements. The structures have different hole radii in the range of 95 nm to 100 nm (b) Normalised threshold pump powers and comparison with results from simulations on an equivalent passive cavity. The experimental results show a similar trend as the endhole shift is varied. Taken from [128]

A similar trend can be seen in both the experimental and simulated results. The simulations reach higher quality factors and

thus lower thresholds than the experimental results, which could be partly due to fabrication limitations, as discussed in section 2.2. Furthermore, all optimised cavities become increasingly sensitive to fabrication errors, as can be seen by the increasingly small hole shifts required for further optimisation of the Q-factor in the works by Nakamura et al. [83]. Thus any fabrication error between cavities serves to further enhance the variations in the measured threshold power. The difference between experiments and simulations can also be partly explained by looking at the different contributing factors to the total Q-factor. In the FDTD simulations, only the radiative losses from the cavity are used to determine the quality factor. In real devices, however, there is also an internal loss which, recalling section 3.1, can be described in relation to the photon lifetime τ_p and Q-factor as

$$\frac{1}{\tau_p} = v_g(\alpha_m + \langle \alpha_i \rangle) = \frac{\omega}{Q_{tot}}, \quad (4.2)$$

where α_m is the mirror loss, $\langle \alpha_i \rangle$ is the spatial average over internal cavity losses, and ω is the angular frequency [111]. In essence, using the Q-factor directly from the simulations assumes $\langle \alpha_i \rangle = 0$, but a total Q-factor, $Q_{tot} = \omega / v_g(\alpha_m + \langle \alpha_i \rangle)$ can be calculated by determining the mirror loss $\alpha_m = \omega / v_g Q_{sim}$ directly from the simulated Q-factor and estimating the internal loss. The predicted threshold evolution for the hole shifts can be seen in figure 4.4 for different internal loss values along with the mean from the experiments. The inclusion of the internal loss limits the maximum obtainable Q-factor and then also the minimum obtainable threshold power. For internal losses on the order 1 cm^{-1} to 4 cm^{-1} a better agreement is obtained. The internal loss of a ridge waveguide with embedded quantum dots was examined in [130], where a value of 5 cm^{-1} was found. It should be noted that the quantum dots in the reference emit at a different wavelength and that the dimensions of the waveguides are much larger. Both may change the internal loss, compared to our structure and quantum dots. Furthermore, the slow-light effect in photonic crystals [131]

could increase the internal loss due to disorder by increased light-matter interactions. If the Q-factor of the device is limited by the internal loss, i.e. $\langle \alpha_i \rangle \gg \alpha_m$, the maximum obtainable Q-factors are 1.3×10^5 , 0.5×10^5 and 0.3×10^5 for internal losses of 1 cm^{-1} , 2.5 cm^{-1} and 4 cm^{-1} , respectively. Comparing these values to the maximum Q-factor of 2.7×10^5 predicted by simulations for the optimum hole shift, the internal loss can be the limiting factor.

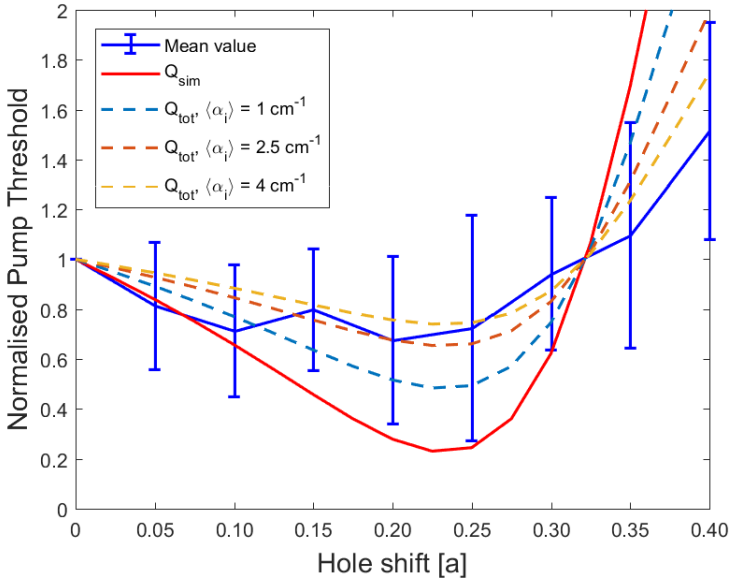


Figure 4.4: The measured mean threshold pump powers along with simulation results where the total Q-factor is calculated including an internal loss $\langle \alpha_i \rangle$. Better agreement between simulations and experimental results are observed when the internal loss is included.

After the optimum hole shift of $0.25a$, the simulations predict a drastic increase in the threshold due to a drop in the Q-factor and this is not observed experimentally. With the addition of an internal loss of 4 cm^{-1} , the predictions fit better. In the fabricated samples, the shifted holes start to merge at specific values of the radius and shift. For the radii measured, the holes are starting to merge around $0.35a$, and an air bridge is visible for shifts of

0.4a, see figure 4.5. This merging changes the mirror structure significantly, and the results for the two largest hole shifts should be viewed with this in mind.

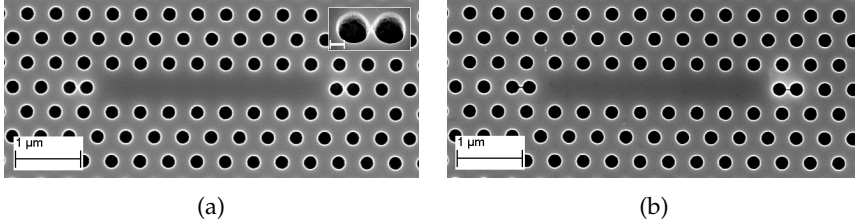


Figure 4.5: The L7 0.4a shifted cavity with $r \approx 100$ nm in two different groups on the same sample. (a) Some material still remains between the neighboring holes, but the inset shows the holes nearly touch each other. Inset scale bar is 100 nm. (b) The two holes have merged and an air bridge is formed.

4.3.2 Maximum output power

The maximum output power from the laser is also readily available from our characterisation and can for all measurements be found at the maximum input power. The measured maximum output powers can be seen in figure 4.6 and again vary significantly between different groups. These results are also normalised to the value of the zero-shifted cavity in each group, and the result can be seen in figure 4.6b. The fifth group has an abnormal behaviour with a very low output power for the zero-shifted cavity and very high output power for the cavity with a shift of 0.05a. This greatly skews the mean, and in order to show the standard deviation, the scale on the y-axis must be so large that graphically the quite significant change in the mean of the maximum output power is no longer noticeable. Therefore the range in the plot is limited to highlight precisely the change in mean values without group five. The plot with the same data and a full range of the y-axis can be found in [128].

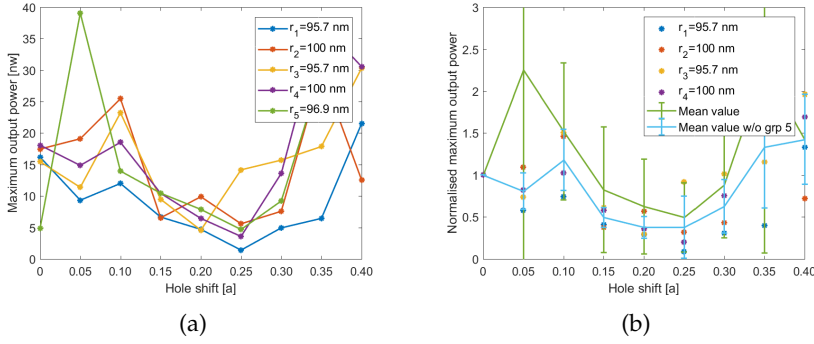


Figure 4.6: (a) Maximum measured output power of the lasers for different hole shifts. As can be seen, the fifth group (r_5 , green line) deviates from the others having a high maximum output power for a shift of $0.05a$ compared to no shift. (b) Normalised maximum output power. The group that deviates from the others is excluded from the plot and mean calculations both with and without this group are shown. Taken from [128]

The maximum output power is found to decrease initially as the holes are shifted and has its lowest value at the value of the hole shift, found above, that minimises the threshold. For larger hole shifts, the output power again starts increasing. The maximum output power is a less clear metric to determine the laser performance since a laser with higher Q-factor has a higher photon density in the cavity but a smaller percentage of these photons escape the laser cavity compared to a laser with lower Q-factor. Furthermore, the total Q-factor can be separated into individual contributions Q_i and described as $1/Q_{tot} = \sum(1/Q_i)$. One of these individual Q-factors will be the out-coupling Q-factor, which must not too small compared to the other Q-factors. The smallest individual contribution to the Q-factor then limits the total Q-factor. As done above, the individual Q_i could be separated into two parts, one related to the internal losses and another related to the mirror losses. The internal losses may be further divided into losses due to absorption in the active material and scattering on imperfections/defects along the cavity. The mirror loss can also be further divided into in-plane and

out-of-plane losses. To summarize, there are many individual contributions/limitations to the total Q-factor, but the figure of merit for the laser in practical applications will be the efficiency by which input photons (or electrons for electrically pumped devices) generate output photons from the lasing mode. This efficiency is the product of the internal quantum efficiency, describing the fraction of injected power that generates stimulated emission, and the optical efficiency, describing the ratio of stimulated emission that is collected by the microscope and coupled to the fiber.

Furthermore, the collected output power depends on what can be collected by the microscope. Specifically, a laser with a lower Q-factor but better optical efficiency could have a larger output power than a laser with higher Q-factor and a worse optical efficiency.

To take a closer look, the automated fitting tool described in appendix C, based on laser rate equations and a linear model of the gain has been used to fit the input-output curve of the r1 group, which can be seen in figure 4.7a. To obtain the fit, some parameters must be locked in order to obtain a fit on the parameters of interest. These parameters, along with the ones extracted from the fit, can be seen in table 4.1. The confinement factor Γ has been estimated by calculating the active material volume from the density of quantum dots in one layer, the number of quantum dot layers and the quantum dot size and estimating the mode volume by the line defect cavity area. The Q-factor was estimated to be no higher than two-thirds of the predicted value from the FDTD simulations, which may be an overestimation if the internal losses are greater than 2.5 cm^{-1} .

Next, the Q-factors are modified to follow the trend obtained from the simulations as the hole shift is varied from 0a-0.4a. Furthermore, the optical efficiency $\eta_0 = F\alpha_m / (\alpha_m + \langle \alpha_i \rangle)$ is also modified with the α_m determined by the Q-factor trend as the hole shift is varied from 0a-0.4a. In this analysis the internal loss is first calculated from the fit as $\langle \alpha_i \rangle = \alpha_m / \eta_0 - \alpha_m$. This results in an enormous internal loss of $2.3 \times 10^4 \text{ cm}^{-1}$, which indicates the extraction of η_0 is either poor, or the parameter F , which is here

Table 4.1: Parameters used for the maximum output power analysis.

Fixed		From Fit	
n_g^1	3.17	η_0	8.7×10^{-5}
Γ	5.1e-3	η_i	3.1×10^{-3}
τ_r [31]	2 ns	g_0^2	$3.17 \times 10^{-5} \mu\text{m}^{-1}$
τ_{nr} [31]	20 ns	β	6.6×10^{-3}
N_{tr} [31, 132]	$2 \times 10^5 \mu\text{m}^{-3}$		
Q	40000		

¹Refractive index of InP used as group refractive index.

²See section 3.1.1 for discussion on gain models. The value is low compared to [31, 133]

assumed to be one is very small. An F of 2.6×10^{-4} corresponds to an internal loss of 4 cm^{-1} . The internal loss extracted from the fit and all other parameters are kept constant. The corresponding input-output curves can be seen in figure 4.7b.

The photon density in the cavity can be seen in figure 4.8a. From the photon density, the output power can be found from equation 3.8. The output powers can be seen in figure 4.8b, along with the mean experimental output powers. From this, the photon density in the cavity is seen to initially increase dramatically with the end hole shift and then decrease again in a similar fashion as the Q-factors. However, because the vertical scattering loss is lowered as the Q-factor increases, the output power is seen to decrease with increasing Q-factor. The simulated curves agree well with the experiments. If F could be determined experimentally, the results could be used to validate the fit of η_0 .

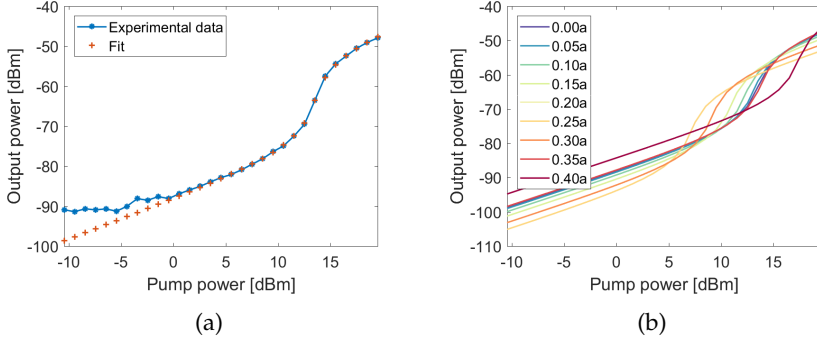


Figure 4.7: (a) Fit to laser rate equation model. Data below -90 dBm is excluded from the fit. See table 4.1 for the parameters of the fit. (b) Calculated input-output curves using simulated Q-factor and other parameters from the fit in (a) over the different hole shifts.

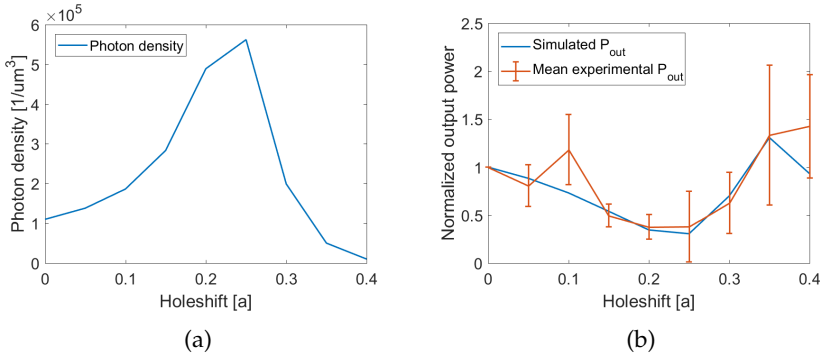


Figure 4.8: Simulation results when the Q-factor is changed with the hole size. The parameters from the fit in figure 4.7a is used along with the simulated Q-factors. (a) Photon densities in the laser cavity. (b) Normalised output powers from simulations compared to the experimental results. Good agreement is observed.

4.3.3 Measured Q-factors

An L7 cavity with a hole radius of 100 nm and endhole shift of $0.2a$ was investigated. It was not possible to measure the high Q-factor modes due to interference noise, and low signal output, as described in section 2.5, but a measurement on one of the lower Q-factor modes can be seen in figure 4.9. The Q-factor is found by dividing the resonance wavelength with the full width half maximum (FWHM) of the curve and is found to be around 600. This Q-factor is too small for it to be the main cavity mode that is observed in the laser samples, and further investigations into the Q-factors of fabricated samples are needed.

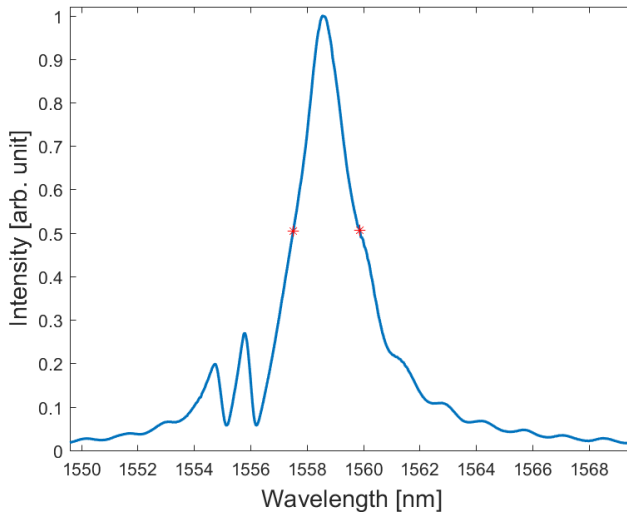


Figure 4.9: Measured scattering from a passive L7 cavity with $0.2a$ shifted endholes and a radius of 100 nm. The red dots at 0.5 intensity are a guide to the eye to indicate the FWHM.

4.4 Mirror phase calculations

Armed with the resonance wavelengths from simulations of the passive cavities along with a simulation to determine the dispersion relation of the photonic crystal waveguide, it is possible to investigate the phase change at the photonic crystal mirror, and how this changes when the first endhole is shifted. The simulations are carried out for cavities of lengths L5, L7 and L9. All the cavity simulations are carried out as described in section 3.2 with a hole radius of 99 nm, a period of 438 nm and a membrane thickness of 250 nm. Normalised E- and H-field components for an L7 cavity with the endholes shifted by $0.25a$ can be seen in figure 4.10.

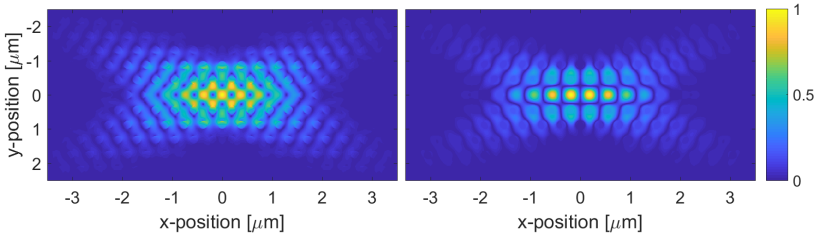


Figure 4.10: Normalized (a) Electric (left) and Magnetic (right) field intensity profiles of the resonant mode for an L7 cavity.

The resonance wavelength for the three different cavity lengths can be seen in figure 4.11a and the Q-factors in 4.11b. The resonance wavelengths can be seen to be very closely spaced for the hole shifts larger than $0.25a$, and for some shifts, the wavelengths extracted from FDTD simulations are identical. The identical resonance wavelengths for two different endhole shifts originates from the FDTD simulations, where the simulation time limits the spectral resolution¹. As the cavity becomes longer, the variation in resonance wavelength across the endhole shifts decreases. For all three cavity lengths, the Q-factor dependence on hole-shift is

¹In fact, the resolution in wavelength can be indirectly found from the steps in wavelength for the L9 cavity.

similar. As the cavity lengths decrease, the fraction of the electromagnetic field that overlaps with the first endhole becomes larger, thus increasing the loss from scattering at this hole, which finally then results in a more significant increase in Q-factor when shifting the hole.

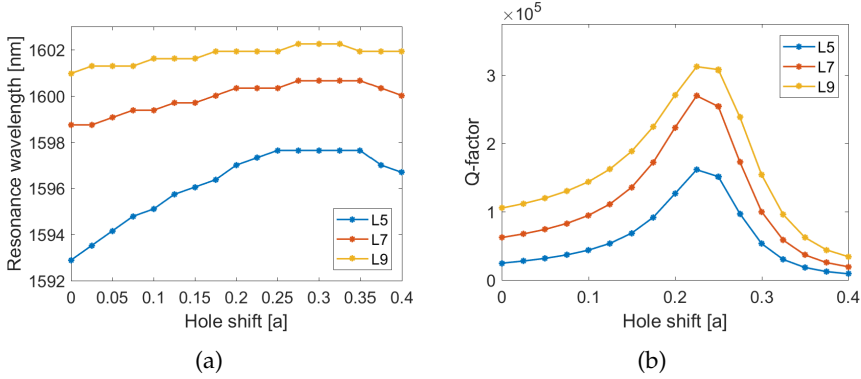


Figure 4.11: FDTD simulations of passive L5, L7 and L9 cavities with varying endhole shifts. (a) Resonance wavelengths. (b) Q-factors. Adapted from [128]

To determine the dispersion relation, a simulation with Bloch boundaries in the plane and normal PML boundaries out of the plane, and the same photonic crystal parameters as in the passive cavity simulations, were carried out. With the Bloch boundaries, only a single period of the waveguide is necessary inside the simulation domain, as the modes to be determined must be periodic in the same manner. Thus, with Bloch boundaries, the electromagnetic fields are copied from one boundary to the next, see figure 4.12a, resulting in a simulation of an infinite waveguide. The Bloch wavenumber k_b was swept to obtain the dispersion relation seen in figure 4.12b. Lastly, the resonance wavelengths obtained from the passive cavities with different hole shifts can be mapped onto the dispersion curve, and their corresponding wavenumber can be extracted. The wavelength mapping for the L7 cavity is seen in figure 4.12c, where some cavities with different endhole shifts, are mapped to the same wavenumber.

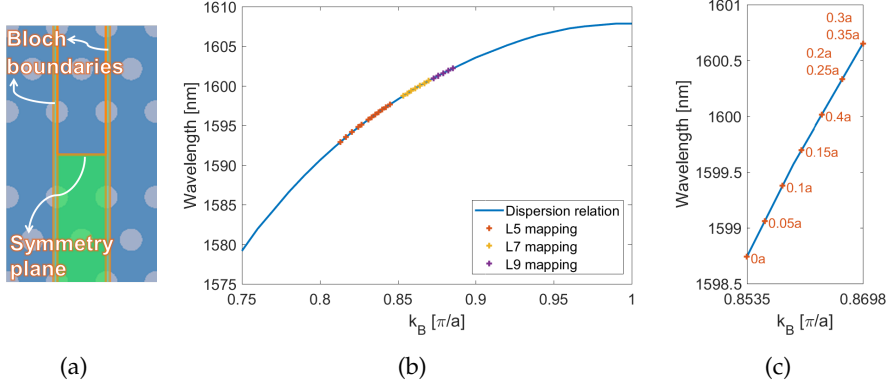


Figure 4.12: (a) FDTD simulation setup for determining the dispersion relation of the waveguide. The shaded green area indicates a symmetry condition. (b) The resonance wavelengths of the L5, L7 and L9 cavities with endhole shifts are mapped onto the dispersion relation of the waveguide. (c) Close-up of the L7 resonance wavelength mapping, highlighting how different shifts have the same wavenumber, and the maximum wavenumber is not obtained for the maximum endhole shift.

Next, an effective Fabry-Perot resonator model is used [129]. The length of the effective cavity is described as $L_{eff} = L + L_p$, where L is the physical cavity length, and L_p is the penetration depth into the mirror. A roundtrip condition for the field then leads to the phase condition

$$\pi p = \phi(\lambda) + k_B L, \quad (4.3)$$

where p is the number of oscillations in the electric field of the standing wave along the cavity, $\phi(\lambda)$ is the mirror phase, and k_B is the Bloch wavenumber [129].

For a Fabry-Perot cavity, there is usually a well-defined spatial position at which the mirrors are placed, and the cavity length is straightforwardly determined as the distance between the two mirrors. For photonic crystal cavities, the actual position of the equivalent mirror is less obvious, and here the length of the physical cavity is simply defined as $L = (N + 1)a$, where N is the number of missing holes in the cavity. Different conventions for

defining the length of a cavity equivalent to that of a PhC exist [77, 78, 129]. The model chosen here places the mirror in the equivalent cavity at the center of the first endhole in a standard L_N cavity, see figure 4.1.

As the first endhole is shifted further away, the physical cavity length is kept constant, and any changes induced by this shift are then included in the mirror phase. The number of oscillations in the electric field of the standing wave along the cavity is $p = N + 1$ for all modes investigated.

The results can be seen in figure 4.13 for the three different cavity lengths. The mirror phase varies around a π phase shift for the L5 cavity as the endhole is shifted, indicating a good choice of the effective cavity length. The absolute mirror phase increases with the cavity length, but for all three cavity lengths, it is close to π phase shift. As expected from eq. (4.3), the mirror phase follows directly from the resonance wavelengths seen in figure 4.12c. The minimum phase change occurs at a larger endhole shift than the endhole shift maximising the Q-factors, which could indicate that the change in the mirror phase is due to the physical change in the cavity and not the change in Q-factor. As the cavity length increases, the curves are less smooth due to the cavity resonances being very closely spaced in wavelength for all the hole shifts. As mentioned above, this is due to limitations in the spectral resolution from the FDTD simulations. The resolution could be improved by increasing the simulation time and increasing the number of simulations along the span of endhole shifts.

Lastly, the penetration depth, L_p , into the photonic crystal mirror is investigated. Here, the photonic crystal mirror in the effective Fabry-Perot model is interpreted with conventional grating mirror theory. For a conventional Bragg mirror, the penetration depth is related to the mirror phase as [111]

$$L_p = -\frac{\lambda_0^2}{4\pi n_g} \left. \frac{d\phi}{d\lambda_0} \right|_{\lambda_0}, \quad (4.4)$$

where λ_0 is the resonance wavelength, n_g is the group velocity

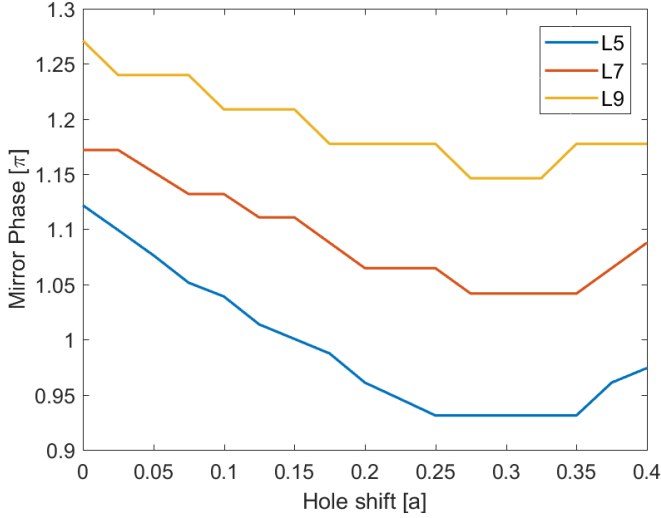


Figure 4.13: Calculated mirror phases for L5, L7 and L9 cavities. For L5, the phase change varies close to π . The absolute phase change increases and decreases with the cavity length. Taken from [128]

determined from the dispersion relation, and $d\phi/d\lambda_0|_{\lambda_0}$ is the change in the phase as a function of cavity wavelength [111]. The penetration depth for the L7 cavity is determined by extracting the phase and resonance wavelength from simulations of L5 and L9 cavities to calculate $d\phi/d\lambda_0|_{\lambda_0}$.

The penetration depths for different endhole shifts can be seen in figure 4.14a. As they are calculated directly from the mirror phases in figure 4.13, the result is also slightly jagged, and could benefit from a better resolution.

The penetration depth is seen to vary around 1 μm and increases as the endhole are shifted up to a certain point. The penetration depths can also be directly extracted from the variation of the E-field along the centerline in the FDTD simulations. Figure 4.14b shows the normalised E-field intensity displayed from the effective cavity mirror position, i.e. $x = L/2 = (N + 1)a/2$, and further away from the cavity for the L7 cavity with different

endhole shifts. The calculated penetration depths are overlaid on the curves. The calculated penetration depths appear to reflect both that the intensity at the mirror position $x = (N + 1)a/2$ increases with Q-factor, and the decay away from the cavity into the mirror, exactly as expected, indicating the usefulness of the equivalent Fabry-Perot model. The increase in penetration depths reflects well the more gentle confinement of the field described by Akahane et al. [79] when shifting the holes.

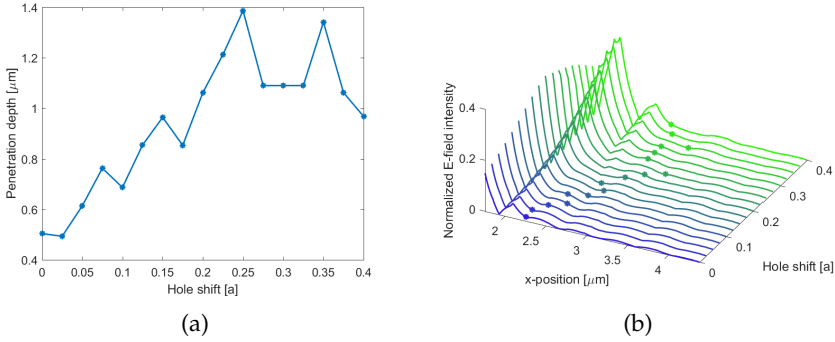


Figure 4.14: (a) Penetration depth calculated from the mirror phase extracted from simulations. (b) Visualization of simulated E-field penetration into the mirror as the endhole shift is varied. The x-axis in the figure starts at $L = (N + 1)a/2$, corresponding to the edge of the cavity. The dots are the calculated penetration depth, shown in (a), mapped onto the simulated results. Adapted from [128]

4.5 Summary and outlook

It has already been established by others how an abrupt change in the electromagnetic field is an important cause of scattering, and the first endhole is the primary cause of vertical loss in the photonic crystal cavities. By spatially shifting this first hole slightly, the overlap with the field becomes smaller, and the change becomes less abrupt. This decreases the vertical scattering, resulting

in a higher Q-factor cavity, which is predicted to decrease the laser threshold and increase the penetration depth.

Here, we fabricated and characterised samples with photonic crystal nanolasers with a systematic shift of the first endhole to determine how the threshold power changes, and if the change follows directly from the predicted change in Q-factor as shown earlier for passive cavities. In general, this appears to be the case. However, the thresholds observed experimentally decrease less than predicted by the Q-factors obtained from FDTD simulations. With the inclusion of an internal loss in the model, the Q-factor has an upper limit, and limitations in the fabricated hole quality for the samples in this chapter might further decrease the upper Q-factor limit.

Further, the maximum output power was measured for the different endhole shifts. The maximum output power was found to decrease as the endhole was shifted, up to an endhole shift of $0.25a$, after which the output power again increases. For the laser with an endhole shift of $0.25a$, the maximum output power is halved compared to the zero-shifted cavity. Intuitively this can be explained by considering that a higher Q-factor leads to less vertical scattering loss, and thus simply less measurable output power. The laser rate equation model was used to predict the change in output power when the Q-factor changes due to endhole shifts. It is also necessary to include changes in the efficiency η_0 , as this parameter is strongly dependent on the Q-factor (mirror loss), and directly related to the output power. The model was shown to capture the evolution in output power observed experimentally. We note that, an increase in photon density in the cavity is predicted, but the decrease in vertical scattering loss is a stronger effect, ultimately limiting the output power. If a similar experiment is carried out for devices with a buried heterostructure gain material in the cavity and a side coupled waveguide the maximum in-plane output power could also be characterised. The in-plane output power is, of course, much more interesting from an application point of view.

Lastly, simulations were carried out to investigate the phase

change occurring at the photonic crystal mirror and the penetration depth into the photonic crystal mirror and how these vary with the endhole shifts. The 1D effective Fabry-Perot model appears a viable way to investigate this, insofar as it provides reasonable penetration depths when compared to FDTD simulations. The model used here with the chosen effective cavity length L leads to a mirror phase close to π , which indicates a good choice in the definition of the cavity length. The mirror phase decreases with increasing endhole shifts up to a certain shift where it plateaus, after which it again increases. The behaviour follows straight from the resonance wavelength of the cavities, and the mapping of resonances onto the dispersion curve. The penetration depth is seen to increase as the endhole is shifted, peaking close to the same endhole shift as the minimum of the mirror phase. The penetration depth is directly dependant on the mirror phase. It is therefore greatly affected by the jumps of the mirror phase calculations, due to limited resolution in resonance wavelengths from the FDTD simulations for different endhole shifted cavities. Still, the penetration depths around $1\text{ }\mu\text{m}$ appear reasonable, when compared with the field profiles from the FDTD simulations.

The current investigation is limited by the fabrication methods that have since changed, as described in section 2.1. Specifically, the dry etch recipes of both the silicon nitride hard mask and the indium phosphide membrane have changed since the first fabrication of the samples reported here. Two main things determine the success of such an etch recipe, the uniformity of the holes and the quality of the holes, i.e. the verticality and the roughness. Cavities fabricated with the new fabrication methods have not yet been characterised for a higher Q-factor with the setup described in section 2.5. However, initial SEM inspections of samples with the new fabrication method show smoother and more vertical sidewalls than the method used for the fabrication of the samples used in this chapter. Furthermore, since the measurements presented in this chapter, a piezo-stage has been installed under the microscope used for input-output characterisation of the lasers, which

yields more reproducible results, which could hopefully serve to limit the uncertainties in the measurements. The new fabrication methods give hope that a higher Q-factor can be reached in the future, where more vertical sidewalls hopefully limits the internal loss. This will be an essential step towards gaining a better understanding of the phase change the electromagnetic fields undergo at the photonic crystal mirror, which can be used to enhance the cavity design [129]. At the time of writing, a new sample is in the fabrication pipeline, containing optimised line defect cavities of L5, L7 and L9 that will allow for experimental comparison across cavity lengths. The design also includes smaller increments in the endhole shifts.

CHAPTER 5

BURIED HETEROSTRUCTURE LINE DEFECT DEVICES

Reducing the active material volume inside the nanolaser cavity while maintaining a high Q-factor can reduce the laser threshold and energy consumption of the device [3]. One way to reduce the active material size inside the cavity is by selectively removing the active material where it is not wanted, and regrowing passive material instead to form isolated regions of an active material known as buried heterostructures. Fabricating a photonic crystal waveguide around the BH can form a double heterostructure cavity [44], where the bandgap of the photonic crystal in the BH part is shifted so light of slightly longer wavelengths is allowed in the BH part of the structure, but above the bandgap and therefore forbidden in the open waveguide area. The record-breaking photonic crystal lasers with extremely low thresholds fabricated by NTT [31, 44–50] are all based on the double heterostructure cavity.

The lasers from NTT use quantum wells as the gain material, for which the difference in refractive index between the BH region and the passive region is significant. Switching to quantum dots promise a further reduction in the laser threshold [134, 135], as well as a much better temperature stability [100, 135]. For quantum dots, the thickness of the wetting layer can directly tune the refractive index difference between the BH region and the passive region may still be significant. If the wetting layer is only a few monolayers thick, and the different quantum dot layers separated by the same material as the surrounding passive material, the

refractive index difference between the BH and its surroundings might be minimal. While it has been predicted by numerical simulations that tiny differences in the refractive indices can form a cavity with a high Q-factor [89], this remains to be experimentally demonstrated.

If the refractive index difference is too small to confine the light effectively, the advantage of the reduction in active material volume can still be harnessed, by surrounding the BH with a line defect cavity instead of an open waveguide. QW BHs of similar lengths as the cavity for short L3 cavities have been experimentally demonstrated [136]. However, no experimental investigation where the BH length is varied inside a fixed-length line defect laser has yet been published.

Here we fabricate such photonic crystal lasers with a quantum well BH of varying lengths confined to an L7 line defect cavity. The fabrication of the gain material only in regions where it is desired is enabled by technological achievement by Aurimas Sakanas in his PhD project [102].

The chapter starts with a discussion on the physical effects of introducing and varying the buried heterostructure in relation to the laser rate equation model. The following sections introduce samples fabricated and characterised before finishing with a numerical FDTD investigation of the buried heterostructure cavities, and how this influences the cavity resonances. This chapter is based on the submission to CLEO/Europe 2019, and the design and measurements were carried out by the author. Different parts of the fabrication process were carried out in collaboration with Aurimas Sakanas.

5.1 Varying the active region in a photonic crystal cavity laser

The active region containing the gain material is a crucial part of any laser. The material parameters have a direct influence on the threshold of the laser and the maximum output power achievable.

Firstly, the assumption is made that the cavity as a whole remains mostly unchanged by altering the size of the buried heterostructure, i.e., the Q-factor of two otherwise identical cavities remains unchanged, and that the group velocity only changes slightly, due to the small effective refractive index difference between the two cavities. Relating this to the rate equation model in section 3.1, changing the longitudinal length of the buried heterostructure can be coupled directly to modifying the confinement factor $\Gamma = V/V_p$, where V is the active material volume and V_p is the mode-volume. In the case of small perturbations, the mode-field profile, and thus mode-volume, remains unchanged. However, the active material volume is directly changed. Γ is a crucial parameter in the laser rate equations and will influence the input/output curves, and the thresholds that are measured, see figure 5.1, where the BH is varied, and Γ thus changes accordingly. In this figure, the pump efficiency is not changed as the BH length is varied, but it must be discussed how the power absorbed in the gain medium depends on the BH length. For samples with gain material embedded everywhere, the pump power, P_i , used for excitation should be defined as the product of the total excitation power P_{exc} , and the ratio between the pump spot area and the cavity area, Γ_{exc} [77]. For samples with embedded BH, Γ_{exc} may be defined as the ratio between the BH in-plane area and the pump spot area. For a pump beam with a $2\text{ }\mu\text{m}$ radius, and a 350 nm wide and $7a$ long BH, $\Gamma_{exc} \approx 8.6\%$. Note, that the power distribution should be uniform across the pump spot for the above to hold. Otherwise, an additional correction could be used when determining Γ_{exc} .

It should also be noted, that the dependency of Γ_{exc} on the BH spot is dependent on how the pump light couples to the sample and generates carriers; if the pump light is simply absorbed in the gain material then Γ_{exc} should be dependent on the BH size. Instead, if the photonic crystal cavity has a mode at the pump wavelength, the light could initially couple into the photonic crystal, and subsequently excite carriers in the BH. Then the in-plane

cavity area should first be normalised by the pump spot area. Secondly the coupling efficiency of the pump light to the mode at the pump wavelength should be included. Finally, the ratio of the BH length to the cavity length should be included to reflect absorption through different lengths of BH. In the experimental results presented in the following, the input power on the horizontal axis is the total excitation power P_{exc} , and no normalisation to the BH size has been done. Making the active volume smaller decreases the available states in the active material, and thus lowers the number of excited carriers needed for population inversion. Changing the active area can, therefore, be an attractive route to lowering the device threshold [31, 137]. In the experiments, there are variations between cavities on a single sample of such a scale that no single physical parameter can be varied uniquely. This will distort the picture as we will see in the following sections.

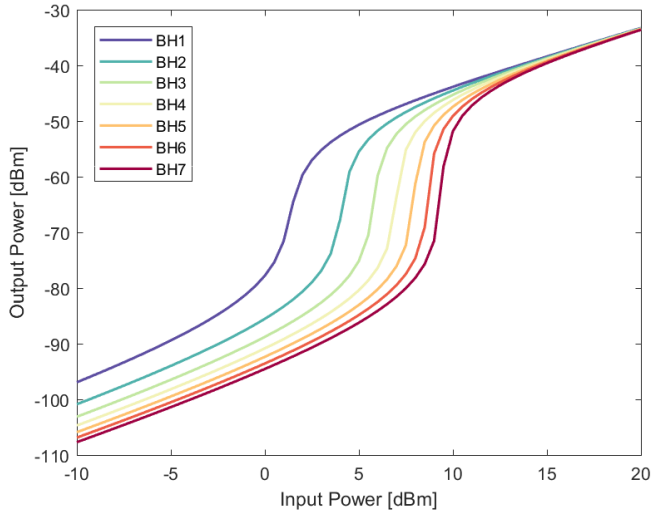


Figure 5.1: Input-output curves for different lengths of BH in an L7 cavity generated from laser rate equations. Only the active volume is changed between curves. BHn corresponds to a BH of length na , where a is the photonic crystal period.

5.2 Device overview

The sample analysed in this chapter is based on the fabrication method outlined in chapter 2. It has three layers of embedded quantum wells that are 350 nm wide and with lengths from $1a$ to $20a$ in steps of $1a$. Lasers with an n long BH embedded are denoted BH n . The SiN $_x$ was etched with the ICP-RIE process, and the InP etched with the standard RIE process. The sample had one group of standard line defect lasers of length L7 with varying hole radii, but also contained one group of optimised L7 cavities with varying radii. In the optimised design, the first and third endhole shifted by $s_1 = s_2 = 0.225a$ to increase the cavity Q-factor.

An SEM image of the optimised cavity can be seen in figure 5.2a. Only one chip was fabricated, and thus only one group of photonic crystal lasers for the standard L7 and the optimized design was analysed. The Q-factor obtained from FDTD simulations is approximately 80000. Figure 5.2b shows the L7 cavity with a BH of length $13a$ embedded. Due to fabrication constraints, the dry-etch method does not etch through the QW layer, as it contains aluminium which can not be etched by the current recipe. For BH lengths longer than the cavity, i.e. L7, the holes in the mirror are not fully etched. It is reasonable to assume this will decrease the performance of the mirrors and results for BHs larger than L7 should be interpreted with this fact in mind. Finally, the sample can be cleaved and the QW BH can be etched away to investigate the alignment. This can be seen in figure 5.2c, and good alignment of the BH with the photonic crystal defect is achieved. The QW etching and SEM imaging of the cleaved sample was done by Aurimas Sakanas.

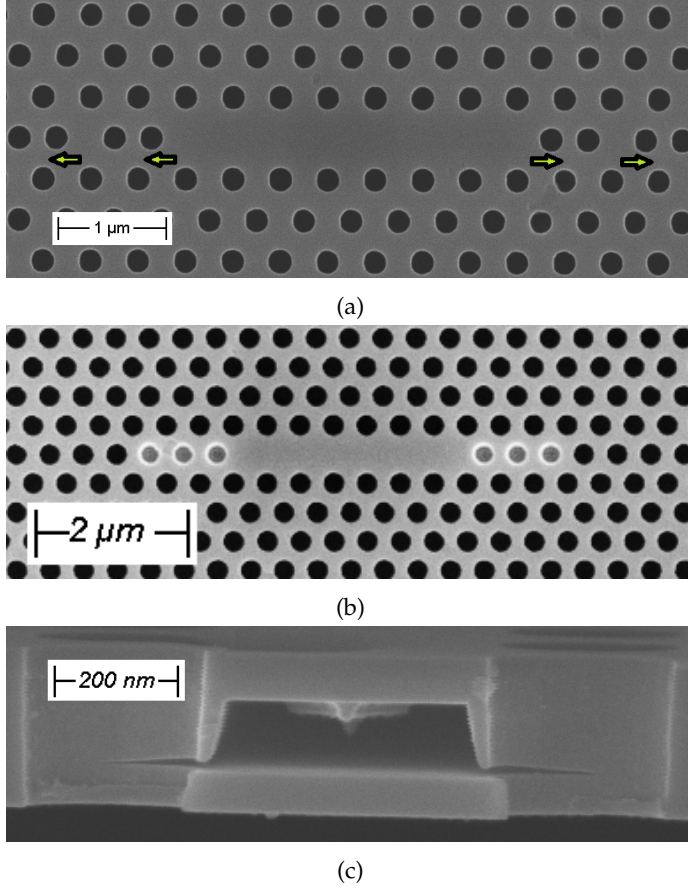


Figure 5.2: SEM images of the sample. (a) The optimized cavity where the first and third in-line hole are shifted to optimize the quality factor. Shifted by $s_1 = s_2 = 0.225a$. (b) An L7 cavity with a buried heterostructure of length $13a$ embedded. The dry etch does not etch the QW and the holes are not fully etched for BHs longer than $7a$. (c) Side-view of a cleaved membrane where the QWs have been etched away to highlight good alignment of the BH[†].

[†]QW etching and imaging of the cleaved sample was done by Aurimas Sakanas.

5.3 Experimental Characterization

The fabricated sample was characterised with the setup described in section 2.4. The measured input/output curves for BH lengths from $1a$ to $7a$ in the optimized L7 cavity can be seen in figure 5.3. For a BH length of $1a$, the measurement is difficult due to low signal, and the shape of the curve for the lowest BH is also different than the others.

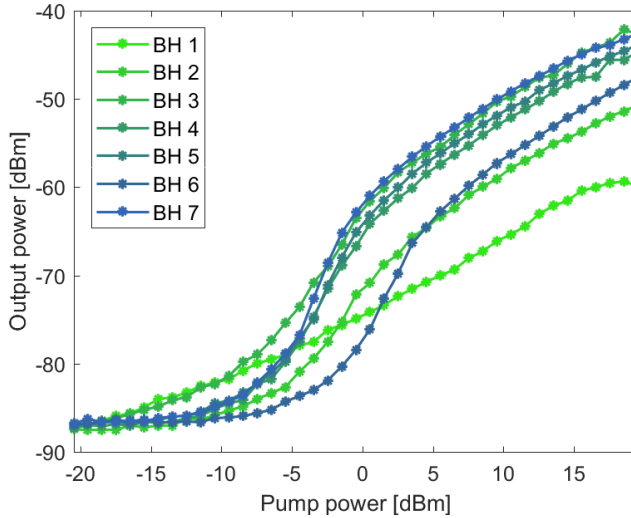


Figure 5.3: Experimental input/output curves for different lengths of BH in the optimized L7 cavity. BH_n corresponds to a BH of length na , where a is the photonic crystal period. The laser with the shortest BH, does not achieve lasing.

The thresholds and maximum output powers (taken at 3 dB attenuation, where the OSA traces are more stable due to less thermal fluctuations) of the sample can be seen in figure 5.4.

First, no clear trend emerges in neither the thresholds or maximum output powers as the BH length is varied. The optimised cavity with BH of length $6a$ has a very high threshold, but also a lower maximum output power than its immediate neighbours, which could be caused by local defects in the sample. This could

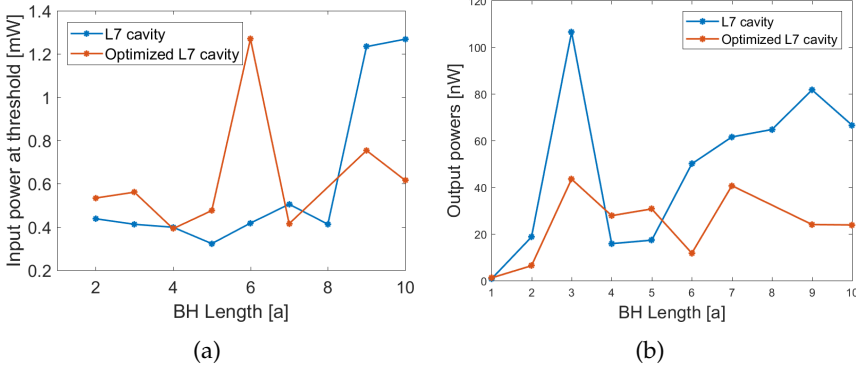


Figure 5.4: Experimental results for the standard and optimized L7 cavity with varying lengths of BH. (a) Laser thresholds powers. (b) Maximum output power at 57 mW pump power.

be due to some local defect in the sample. The threshold powers for cavities with BHs of length $1a$ should also be considered with caution as the onset of lasing is much less evident in these results. Without an apparent onset of lasing, the devices can be considered more LED-like, and the assignment of a threshold is erroneous. The maximum output power also fluctuates too much to conclude anything. It could appear as if the output power increases with the BH length for the standard L7 cavity, apart from the cavity with a BH of length $3a$. However, for BHs longer than $7a$, the BH protrudes into the mirror, and due to fabrication limitations, the mirror holes are not fully etched. Considering only the cavities with BH lengths from $4a$ to $7a$, the increase is much less clear. Furthermore, such behaviour should be visible in both the standard and the optimised cavity for a conclusion to be accepted, which is not the case. In [114] it was shown how resonant pumping through a higher order mode could increase the device efficiency. If a higher order mode overlaps with the pump spot, the position of the pump spot could affect the coupling efficiency. The optimum spot position for collections is above the mirrors where the primary scattering occurs. The optimum pump position, on the other hand, would be either where the largest overlap of the

beam with the BH (if the pump light is absorbed vertically), or where the coupling efficiency of pump light into a higher order cavity mode is largest. For small BH lengths located in the cavity centre, the current setup pumping and collecting from the same spot on the sample might then suffer by not being able to both pump and collect optimally at the same position. With only one group of each type of photonic crystal laser on the sample, the outliers impair the results. More measurements on similar cavities on identical samples must be done to reduce uncertainties on individual measurements, and average over fabrication variations.

5.4 Simulations of buried heterostructure devices

With the discouraging experimental results, the focus shifts to numerical simulations using the FDTD software Lumerical as described in section 3.2. The BH can be included by merely adding embedded volumes in the InP membrane with thicknesses and different refractive indices corresponding to fabricated well and barrier heights and indices respectively. In order to resolve the difference in the refractive index, the mesh resolution in the z -direction must be increased dramatically. Total internal reflection in the membrane confines the light out-of-plane. Ordinarily, the resolution in the z -direction is not strict as no additional features must be resolved across the membrane. The only requirement is to choose an integer number of periods in the membrane, to ensure the mesh correctly ends at the membrane edges. Furthermore, the fields are typically recorded in the plane, relaxing the requirement on the stepsize further. A stepsize in the z -direction with ten periods inside the entire membrane is sufficient. For a 250 nm thick membrane this is a stepsize of $\Delta z = 25$ nm, for which it is impossible to resolve the BH with a well thickness below 10 nm. To resolve wells with heights approximated by 10 nm and barriers of 20 nm, a stepsize of 5 nm can be chosen, and this is still computationally feasible for simple LD cavities. In the next chapter,

the BH will also be incorporated in Fano laser cavities, and FDTD simulations, where the mesh resolution in the plane must also be increased in order to resolve the nanocavity. For such simulations, the extra computational power required for a good mesh in the z -direction becomes too heavy.

5.4.1 Effective medium theory for the buried heterostructure

An effective medium theory is applied to resolve the computation issue. The effective medium theory is often used when dealing with subwavelength structures, especially when considering metamaterials [138]. The BH consists of three well layers, surrounded by four barrier layers embedded in a top and bottom InP layer. The permittivity changes across the membrane as the materials are switched between passive InP, QW and barrier layers across the membrane. Instead, a parallel effective permittivity can be calculated for the membrane in the region where the BH is embedded as

$$\varepsilon_{eff} = \sum_{i=1}^3 f_i n_i^2, \quad (5.1)$$

where $f_i = \Delta z_i / z_{tot}$ and n_i denotes the filling fraction and the refractive index of the i^{th} material in the membrane respectively [138]. The effective refractive index can then be calculated as $n_{eff} = \sqrt{\varepsilon_{eff}}$. Instead of individual layers, the simulations have an embedded box of volume $V = z_{memb} w_{BH} l_{BH}$ with refractive index n_{eff} , where z_{memb} is the thickness of the membrane, w_{BH} is the width of the buried heterostructure and $L_{BH} = BH a$ determines the length. The effective medium still reflects the refractive index change along the membrane at the edges of the BH. However, all field effects across the membrane between individual well and barrier layers are neglected. The effective medium approximation might add an error to the calculations of reflections at the edge of the BH, especially in the presence of a photonic crystal cavity [139]. However, as will later be discussed, it is the

index change which forms a heterostructure photonic crystal environment that is primarily responsible for reflections at the BH edge. The effective medium theory lowers the requirements on the stepsize in the mesh in the vertical direction again, making LD simulations with BH much faster and Fano simulations with BH feasible. It should be noted that the thicknesses of the individual well and barrier layers are not known to a very high precision as they are not directly measured during growth, so the simulations with individual QW layers embedded also did not reflect the fabricated samples exactly, making the approximation more enticing. For three layers of embedded QWs with a well thickness of 10 nm and a refractive index of $n_{well} = 3.6$ surrounded by four barrier layers with a thickness of 20 nm and a refractive index of $n_{barrier} = 3.26$ in a 250 nm thick InP membrane with a refractive index of $n_{memb} = 3.17$, the effective refractive index from equation 5.1 is approximately $n_{eff} = 3.25$.

5.4.2 Open photonic crystal waveguide

To gain insight into the effect a BH can have on the photonic crystal devices, consider first a simpler system. An open waveguide with some length of buried heterostructure embedded. Transmission simulations were carried out to determine if reflections from the BH are strong enough to create cavities where the field is confined to the BH without the addition of photonic crystal mirrors. The simulation setup with a BH of length $8a$ can be seen in figure 5.5. A Gaussian source is used, which has many reflections when first injected into the waveguide at the wavelengths that are not guided. For this reason, apodization in the monitors must be used. The left and right yellow lines are reflection and transmission monitors, respectively. The yellow cross in the middle is a time monitor for the spectrum in the centre of the BH. The two yellow rectangles are index and electromagnetic field monitors.

The transmission through the open waveguide along with the transmission through an open waveguide with a BH embedded in the entire waveguide length can be seen in figure 5.6a. The

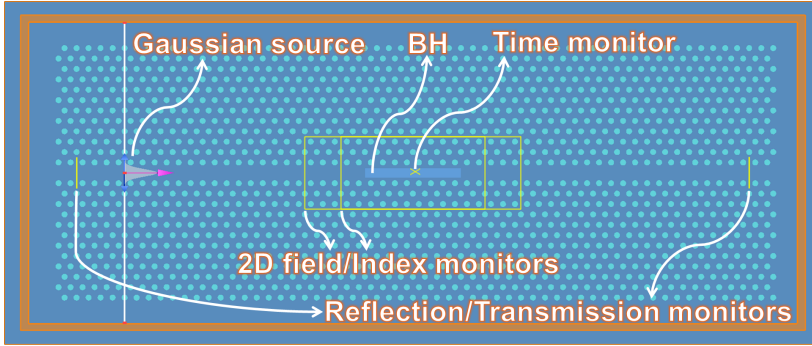


Figure 5.5: Simulation setup for the transmission through BH in an open waveguide with a Gaussian source and different monitors.

transmission is seen to be broadband for both cases until the band-edge is approached, at which point ripples in the graph occurs. The shaded orange area clearly shows how a mode can exist in the waveguide with BH in a spectral region above approximately 1561 nm, where no transmission is allowed in the waveguide without any BH. As the wavelength approaches the bandedge, the dispersion becomes increasingly strong, resulting in a drastic drop in the group velocity while the group index increases dramatically [75, 140, 141]. As the group velocity is lowered, the light-matter interaction is increased through the effect known as slow-light [63, 75, 131, 142, 143]. The increased light-matter interaction was found enhance the material gain in active photonic crystal waveguides was investigated in [131]. However, the gain increases with the same amount as the round-trip time increases, and the round-trip gain remains constant. The strong light-matter interaction has previously been shown lower the mirror loss of photonic crystal lasers [77], which can be explained by the increased round-trip time, i.e. if the light moves slower through the cavity, it impinges on the mirror less often. It should be noted that the modes confined by the photonic crystal heterostructure of the BH all have resonances close to the bandgap, where slow-light can be observed. Figure 5.6b shows the transmission of through BHs with lengths

of $2a$ to $10a$ in steps of $2a$, normalised to the open waveguide transmission. The immediate conclusion is that the addition of a higher index BH affects the transmission only for wavelengths close to the bandedge of the waveguide. This effect is due to the effective index change that the BH adds, which effectively creates a photonic crystal heterostructure. Depending on the index difference the BH adds, the waveguide with and without BH will have slightly different bandgaps, which results in a small mode gap. Light with wavelengths in this gap, can propagate in one of the photonic crystal waveguides, but not the other, which ultimately leads to reflections close to the bandedge [85, 144]. When the transmission is altered near the bandedge, it is reasonable to expect that modes very close to the bandedge can similarly be affected by the reflections happening at the edge of the BH. As the spectral distance between the modes and the bandedge increases, the effect vanishes, and for modes farther away from the bandedge than 10 nm to 15 nm the change in transmission is small. Field profile monitors were applied to determine if the different lengths of BH can cause standing waves. However, as the light source emits into the open photonic crystal waveguide, the light intensity in the modegap is too small to cause confinement. Transmission simulation results for an $8a$ long BH in the waveguide can be found in appendix D. To investigate modes where the field is confined inside the BH region, a different series of simulations are carried out.

Next, simulations with dipoles embedded in the BH were carried out. The purpose of these sources is to excite modes from inside the BH. The spectra for different BH lengths can be seen in figure 5.7a.

Only one resonance exists in the 1500 nm to 1600 nm range for BHs shorter than $4a$, at which point a 2nd order mode confined to the BH begins to emerge. For even longer BHs additional modes appear. The calculated Q-factors of the first-order mode are found to be extremely high, starting from a Q-factor of 2.8×10^5 for the $1a$ long BH, and growing as the BH increases, reaching 1.8×10^7 for the $13a$ long BH, see figure 5.7b. The Q-factors are

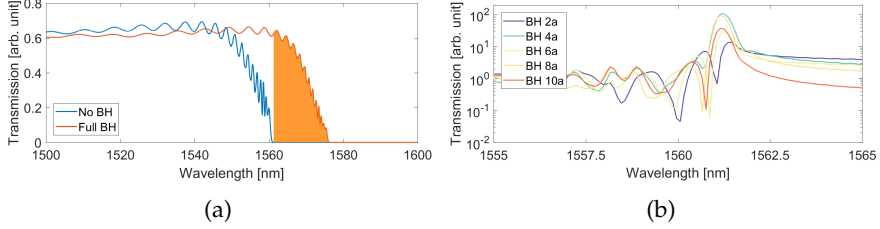


Figure 5.6: Comparison of transmission through an open waveguide with embedded BH of varying length. (a) Transmission through a fully open and waveguide, and one with BH embedded in the entire waveguide length. The shaded orange area indicate the mode gap. (b) The transmission through open waveguides with embedded BH sections of varying lengths normalized to the transmission of the open waveguide.

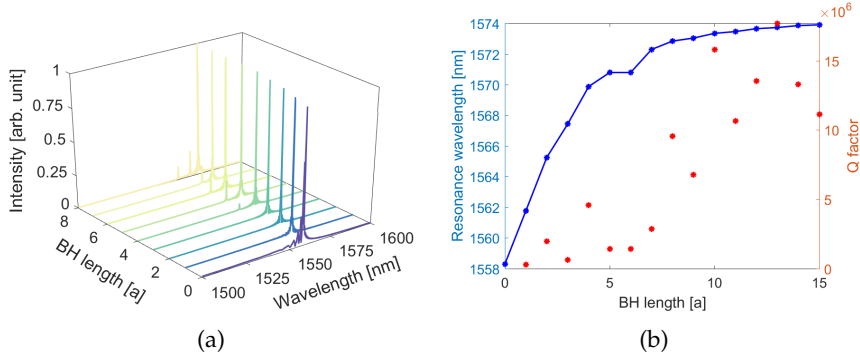


Figure 5.7: Simulations with dipole sources embedded in the BH of varying lengths. (a) Full spectra from 1500 nm to 1600 nm, where additional modes appear as the BH length is increased. (b) Resonance wavelength of the first order mode, and the corresponding Q-factor.

not steadily increasing with the BH keeps increasing with the BH length. However, in real samples, there are disorder and losses along the waveguide. Such disorders can cause reflections which has been shown to eventually limit the cavity length [145, 146] and Q-factor [146]. As described in section 1.3 the waveguide with embedded BH functions as a double heterostructure, with one effective photonic crystal in the BH part of the waveguide surrounded by a different effective photonic crystal. For double heterostructures achieved by changing photonic crystal parameters in a small region of the waveguide Song et al. [87] reported as early as 2005 a Q-factor of 2.7×10^5 and Tomljenovic-Hanic et al. [86] theoretically predict a Q-factor upwards of a million using a Kerr-type nonlinearity in chalcogenide glasses to modulate the refractive index. Finally, Notomi et al. [89] further showed with FDTD simulations how minimal changes in the refractive index could lead to a confined mode in the bandgap resulting in strong confinement in photonic crystal waveguides leading to Q-factors well above 10^9 .

The electric field intensity of the fundamental mode along the waveguide through the centre of the BH for different BH lengths can be seen in figure 5.8. The addition of the BH confines the light. There is a significant change in the shape when going from a BH of length $1a$ to a BH of length $2a$, top left and right in figure 5.8 respectively. The resonance frequency of the mode for the $1a$ long BH is still close to the bandedge of the fully open photonic crystal waveguide and is therefore not as strongly confined to the BH. For the $2a$ long BH, the resonance frequency is now shifted far enough away from the bandedge of the fully open photonic crystal waveguide, that the field outside the BH decays more rapidly. Interestingly, the number of periods in the same spatial window does not change with the BH length, only the number of periods contained within the BH changes. A simulation without BH was also made, where the only mode that appears is a standing wave in the entire waveguide. The reflection from the ends of the waveguide is small, and a standing wave must be close to the bandedge for the reflection to be strong enough to confine

the field. The absolute field intensity is many times smaller for the mode in the simulation without the BH, which indicates poor confinement of the light. The result from the waveguide without BH can be seen in appendix D, along with a similar plot as figure 5.8, but with 2D profile monitors.

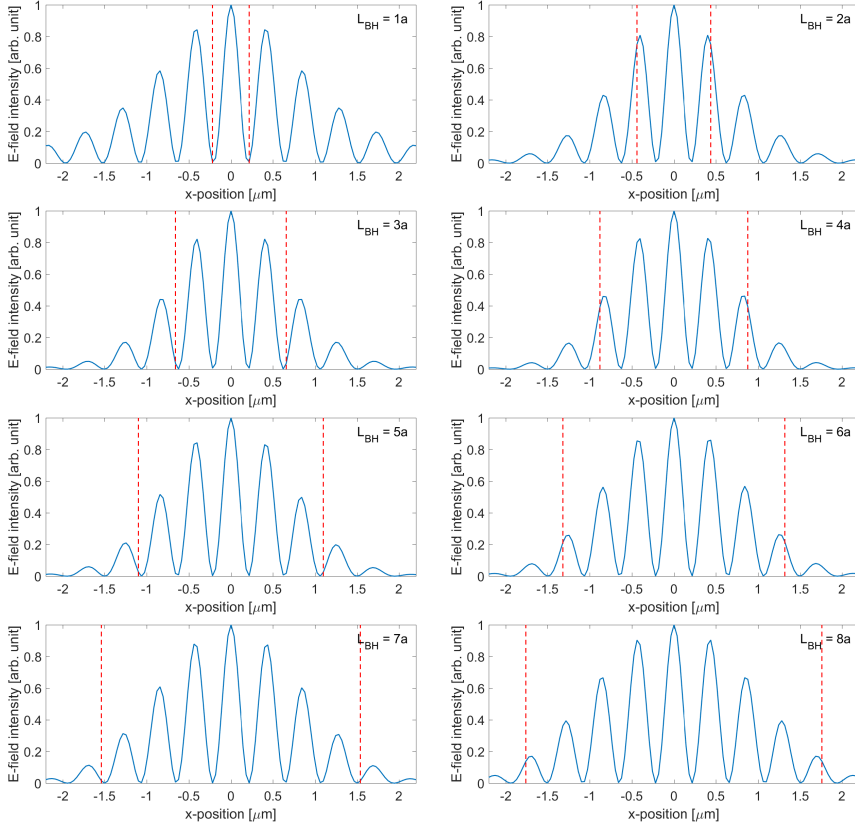


Figure 5.8: Normalized E-field intensity along the waveguide through the center of the BH for varying BH lengths from $1a$ to $8a$. The red dashed lines indicate the edges of the BH.

5.4.3 Line defect cavities

Having investigated the reflections from the edges of the BH, the focus shifts to L7 line defect cavities with an embedded BH to compare with the experimental results. The spectra for simulations with BHs with lengths ranging from $0a$ to $10a$ can be seen in figure 5.9a. When adding the photonic crystal, the mirrors and total cavity length determine what modes are supported in the cavity. The modes observed through the span of different BH lengths are all confined to the entire L7 cavity and not the BH of varying size. The only thing that effectively changes is the resonance frequency, explained by the refractive index changing the effective cavity length. Figure 5.9b shows the resonance frequencies obtained in the experiments along with that from simulations. Error bars are calculated from the standard deviation found in hole sizes ($\sigma_r = 1.7$ nm) and the shift in resonance wavelength ($\sigma_\lambda = 4.3$ nm) caused in an L7 cavity without BH. Good agreements between the simulation and experiments in shape and evolution are observed as the BH length is varied, though with a slight offset in wavelength from the actual resonance values. This discrepancy could originate from the analysis of the hole size, where a radius of 117 nm was measured from SEM images. If the actual radius is slightly smaller, the resonance wavelengths are slightly redshifted for a better agreement. Also, even if the hole sizes have been correctly determined, the experimentally determined resonance frequencies are plotted here for the maximum pump power for all BH lengths. At maximum pump power, the resonance wavelengths are often slightly redshifted due to thermal effects. This effect is not included in the simulations.

Taking a more in-depth look at the fields from the L7 simulations with varying BH lengths, the BH is found to perturb the optical mode. The changes in the electric fields when the BH length is varied is subtle. It is challenging to discern the changes when comparing different plots of either the 2D mode profile or 1D electric field intensity along the LD through the centre of the cavity. For completeness those figures can be found in appendix D

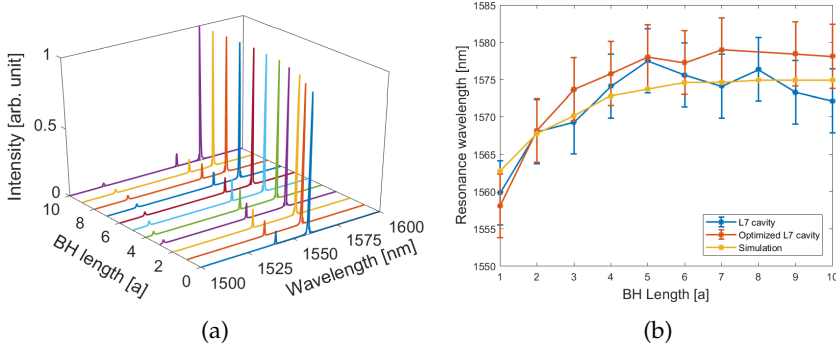


Figure 5.9: Simulation results and comparison with experiments for the L7 cavities with embedded BH of varying length. (a) Spectra from simulations with a hole radius of 117 nm. (b) Resonance wavelengths from the experiments compared to resonance wavelength of the first order mode seen in (a). Error bars are calculated from the standard deviation of fabricated hole sizes and the shift in resonance wavelength caused in an L7 cavity without BH.

for both the first- and second-order modes. Instead, the difference in field intensities $|E|^2$, between the cavity without any BH and the cavities with varying lengths of BH highlights the effect. The difference in the field intensity through the cavity center is seen in figure 5.10 for the 1st order mode. The figure is reproduced in appendix D as figure D.4 with additional BH lengths. From this, the nodes of the field are seen to vary in strength depending on the BH length, leading to both a negative and positive $\Delta(|E|^2)$. The effect is strongest for small BH lengths and then diminishes as the BH becomes increasingly long. This can be explained by the resonance frequency of the mode essentially being outside the bandgap of the photonic crystal without the BH. When the BH is smaller than the line defect cavity, this causes reflections. However, as the BH length approaches the cavity length, the effect vanishes as the region with a photonic crystal line defect without BH, and the photonic crystal mirror is diminished. This behaviour can be further investigated by including longer line defect cavities in future numerical investigations.

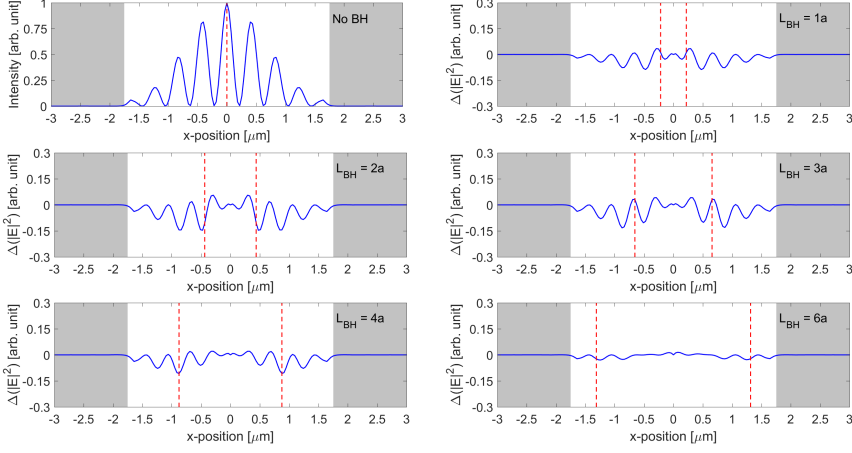


Figure 5.10: Top left: E-field intensity $|E|^2$ for the L7 cavity without BH. Rest: Difference in normalised E-field intensity $\Delta(|E|^2)$, between the cavity without BH and a cavity with varying lengths of BH embedded. The red dotted lines indicate the edges of the BH and the grey shaded area indicates the edge of the cavity. The addition of the BH perturbs the field, close to the edges of the BH. As the BH fills the L7 cavity, the effect vanishes.

5.5 Summary and outlook

Photonic crystal nanolasers with BH of varying lengths inside an L7 photonic crystal line defect cavity were fabricated and analysed to investigate if a lower threshold could be achieved when shrinking the active material volume. All lasers with BHs longer than $1a$ could lase. With the sample analysed no clear dependence of the laser threshold on the BH volume emerges. This result is limited by outliers, specifically, the BH3 of the standard L7 design and the BH6 of the optimised L7 design. Furthermore, the gain material protrudes into the photonic crystal when the BH is longer than the cavity, and the current dry-etch does not etch the QWs, in which case the first holes of the mirror are not fully etched through the membrane. To investigate further and reduce the impact of outliers, additional chips should be fabricated and characterised.

When optical pumping is used for the excitation of carriers, the efficiency can also be affected by the BH size and the overlap with the pump spot. A solution while using optical pumping could be to separate the pump and collection spot, however, in our current setup this comes at an efficiency cost and so far no increase in measurement quality has been observed when using two different ports.

Next, simulations on photonic crystals waveguides and cavities with embedded BHs of varying lengths were presented and discussed, investigating the effects of the refractive index perturbation provided by the BH. The introduction of a BH in a waveguide redshifts the band edge of the photonic crystal around the BH, creating a mode gap in which light can propagate in the BH part of the photonic crystal, but lie outside the bandgap of the passive photonic crystal. This mode gap effectively causes in reflections at the edge of the BH. These reflections form cavities with Q-factors as high as 1.8×10^7 . From the FDTD simulations of an L7 cavity with BH of varying lengths embedded, it was observed that the resonance frequency shifts due to the increased round trip time for photons in the cavity when an increasingly large BH was embedded. Despite the unclear evolution in the threshold pump power, the resonance frequency shifts followed the experiments. Furthermore, the numerical investigations show that the BH can confine light slightly stronger in the region where the BH is embedded, but only if the BH is smaller than the cavity length. While the field profile of the main mode does not change significantly as the BH is varied, the absolute value of the electric field in the cavity does. An increase in the absolute electric field intensity can result in larger stimulated photon emission. Additional investigations of the ratio of mode overlap with the BH and absolute value of the electric field could be carried out in the future to determine if an impact on laser performance is expected. For future samples with a quantum dot-based BH, a direct comparison between experimental resonance wavelengths for BHs of varying lengths and FDTD simulations using an effective medium theory can shed light on the refractive index difference between a

QD BH and the surroundings.

In the future, it would be interesting to apply the methods described in chapter 4 on the mirror phase and penetration depth to the simulations in this chapter. The change in effective cavity length due to the refractive index change of the BH could impact the round-trip phase conditions, which could be visualised with the equivalent Fabry-Perot model.

Furthermore, the L7 cavities with BHs longer than $1a$ achieves lasing, which opens up for new measurement possibilities. For Lx cavities with BHs of length $x a$, it will be possible to move to smaller cavities than what was previously possible with quantum dots embedded everywhere and still achieve lasing. Furthermore, the sample design with $x a$ long BHs embedded in an L n cavity could be expanded to include more cavity lengths than L7. Including longer cavities would increase the span of devices measurable before the BH protrudes into the mirror, which ultimately provides more data to draw conclusions on.

Lastly, open photonic crystal waveguides with an embedded BH of varying length should be fabricated and characterised. Some open waveguides with longer BH ($>10a$) were designed on some of the samples, but defects prevented a thorough investigation. In the future, open waveguides also including the smaller BH ($<10a$) could be designed and fabricated to compare with the numerical investigations presented in this chapter. Their performance can provide valuable insights into the active material, while the resonance wavelengths can be used to probe the effective refractive index of the BH and the bandgap of the photonic crystal.

The effort presented in this chapter is just the beginning of photonic crystal lasers with the buried heterostructure at DTU. It is based on one of the first working samples with the BH embedded, where proper alignment was obtained, and the fabrication of the photonic crystal went as planned. As the absorption of vertical pump light is very small, future samples with electrical connections, could have better injection of current. With this it is possible even lasers with BHs shorter than one photonic crystal

period can achieve lasing. Furthermore, calculating the actual generated carriers in the BH for a given optical input power is not straightforward, while electrical injection of carriers allows easier characterization of the gain media, making an investigation of the variation of active material size in the fixed cavity less complex.

CHAPTER 6

BURIED HETEROSTRUCTURE FANO DEVICES

The Fano laser structure in a photonic crystal was first proposed by Mørk et al. in [90]. The laser is realised by exchanging one of the photonic crystal mirrors in a conventional line defect cavity with an open (or semi-open) waveguide and a coupled nanocavity. See figure 6.1 for SEM images of the fabricated structure. The right side of the cavity, where the conventional mirror has been replaced, is denoted the Fano mirror. The left mirror is denoted the photonic crystal mirror. The H0 cavity that is part of the Fano mirror is denoted the nanocavity, while the open waveguide part between the two mirrors is denoted the LD cavity. The light in the LD cavity travelling towards the Fano mirror will have two possible paths, either straight into the open waveguide or via the nanocavity. The interference of these two paths is what essentially acts as a mirror, and the continuum of modes in the waveguide against the discrete mode in the nanocavity is what gives it the characteristic line shape as described by Ugo Fano in 1961 [147]¹.

The first photonic crystal Fano laser was previously realised on samples with embedded quantum dots everywhere by Yu et al. in [95]. Surprisingly, the samples exhibit a self-pulsing behaviour under certain conditions. It was suggested that the self-pulsing

¹Fano originally studied the inelastic scattering of electrons by helium, but Fano interference is a general wave phenomenon and can be observed in many physical systems.

is due to unpumped quantum dots located in the nanocavity acting as a saturable absorber [95, 96]. The dynamics would be as follows; Initially, the absorption in the nanocavity is high, resulting in a low reflectivity, but as some of the quantum dots in the nanocavity are excited by the laser field itself, the reflectivity increases slightly, which increases absorption in the nanocavity, and a positive feedback loop is established. Eventually, the system settles in a dynamical state where the mirror reflectivity changes periodically. With this passive Q-switching mechanism, the mirror then oscillates between low and high reflectivity at a given wavelength with some characteristic frequency resulting in the pulsed output.

Theoretical investigations by Rasmussen et al. in [96] showed how the self pulsing regime is governed by reflection changes due to nanocavity absorption and further corroborate how a saturable absorber in the nanocavity can cause laser operation to become pulsed. It is further shown how the Fano laser can be engineered to operate in a continuous wave (CW) regime.

With the ability to include BH in the samples, it is possible to fabricate Fano lasers without an effective saturable absorber in the nanocavity leading to CW Fano lasers. Such Fano lasers with BH embedded only in the LD cavity and waveguide region were fabricated and characterised. In this chapter, the fabricated devices are first introduced and discussed, after which the experimental results are presented. Then, a numerical FDTD investigation of Fano cavities with embedded BH of varying length in the LD cavity is carried out, before finally concluding and looking to the future prospects.

The design of the Fano lasers was made by Yi Yu and followed the same design strategy as the devices fabricated in [95], for easy comparison between experiments. The designs all have a LD cavity length of $11a$ and were optimised for the current sample parameters, i.e. membrane thickness and gain material PL. To obtain a high Q-factor Fano laser with a resonance frequency that has a good overlap with the gain material PL, many holes in the photonic crystal must be shifted. All the shifted holes are

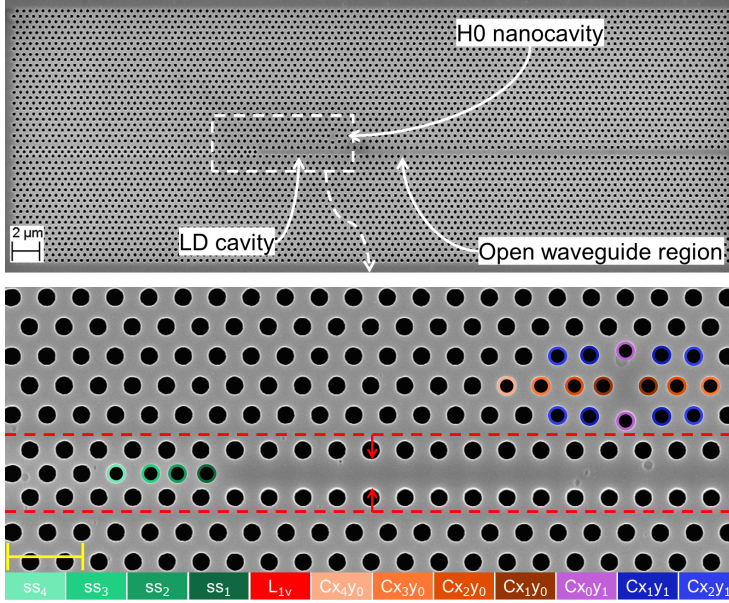


Figure 6.1: SEM images of fabricated Fano laser sample with embedded BH. Top: Full device with the entire length of the open waveguide. Bottom: Close up of the Fano cavity. Holes are shifted around the nanocavity and in the left mirror to optimize the Q-factor. The holes in the rows closest to the waveguide are shifted to tailor the waveguide and nanocavity coupling. All the shifts are highlighted. The yellow scalebar is 1 μm .

highlighted in figure 6.1b.

The design strategy for the Fano laser is outlined in [97] and can be summarized in the following steps; First, the H0 cavity is formed by shifting holes away from the cavity. These hole shifts are denoted C_{x_i, y_j} , where (x_i, y_j) is the position of the hole in relation to the H0 nanocavity. Secondly, the H0 nanocavity is side coupled to a W1 waveguide formed by the removal of one row of holes in the photonic crystal. The two innermost rows are shifted towards the waveguide by L_{1v} to engineer the coupling between the nanocavity and the waveguide. Finally, the broadband left mirror is formed by closing the waveguide. The first holes in left photonic crystal mirror are shifted to tune

the round trip phase of the light in the LD cavity and minimize scattering loss in the mirror. These hole shifts are denoted ss_k , where k is the mirror hole number, i.e. ss_1 is the first mirror hole. The Fano laser devices in this chapter are fabricated jointly by the author and Aurimas Sakanas on the same chips as the BH devices in the previous chapter. The experimental characterisation and numerical investigation were carried out by the author.

6.1 Confining the gain region to the waveguide of a Fano cavity

Careful considerations must be made when the BH of some length is embedded in the semi-open waveguide. First, while the nanocavity has discrete modes with high Q factors, obtaining a high Q factor for the total mode of the Fano laser cavity requires careful design of the different coupling coefficients between the LD, nanocavity and waveguide. Furthermore, the photonic crystal mirror on the left and the waveguide width must be optimised, so the round-trip phase in the LD cavity results in destructive interference at the Fano mirror. This richness is what truly separates the photonic crystal Fano laser from standard photonic crystal line defect lasers. The Q-factor of the total mode has been numerically investigated for different cavity lengths in [97]. Here it was found that a high Q-factor can only be reached if the left mirror is engineered so the round-trip phase results in destructive interference at the Fano mirror. The Fano mirror is so sensitive to this phase change that even a 10 nm change in effective cavity length was found to halve the Q-factor. Embedding a BH smaller than the LD cavity will at least correspond to changing the effective cavity length which can then be expected to affect the Q factor.

Lastly, the Fano mirror can be tuned with a partially transmitting element in the waveguide [91], changing the ratio of the field going straight through the waveguide or through the nanocavity. This tuning affects the Fano lineshape, which has been shown to go from asymmetric, to symmetric and finally to asymmetric

with opposite parity for both active and passive devices [92, 95, 148]. Thus ending the BH close to the nanocavity can result in a reflection from the edge, that could act in a similar manner as the partially transmitting element in prior studies.

Recognising this, Fano lasers with three different BH lengths (8 μm , 15 μm and 30 μm), all of them longer than the LD cavity, were fabricated. The different Fano lasers are denoted FL8, FL15 and FL30, determined by the length of the BH in waveguide². The e-beam lithography pattern can be seen in figures 6.2. The impact of the different BH-lengths is discussed further after experimental results are presented.

6.2 Device overview

As mentioned above the Fano laser structures are on the same samples as the ones discussed in chapter 5, and thus follow the same fabrication recipe. The reader is directed to the previous chapter for the description. Importantly, the widths of the BHs are not the same in the two chapters, and for samples with Fano structures, the BHs have widths of 440 nm. The change in width affects the band structure of the photonic crystal, and therefore the exact simulation results in chapter 5 can not be transferred, but the underlying effects of the BH previously observed remain the same. The period of the photonic crystal is 464 nm, and the fabricated radii of the holes are 120 nm and smaller. The experimentally best performing devices have a radius of 120 nm. All the individual shifts seen in figure 6.1 can be found in table 6.1.

²If both the LD cavity length and the BH length is varied, it would make more sense to denote the lasers by FLnBHx, where n (x) is the length of the LD cavity (BH region), but since all the devices analysed here have the same LD length, the naming is simplified.

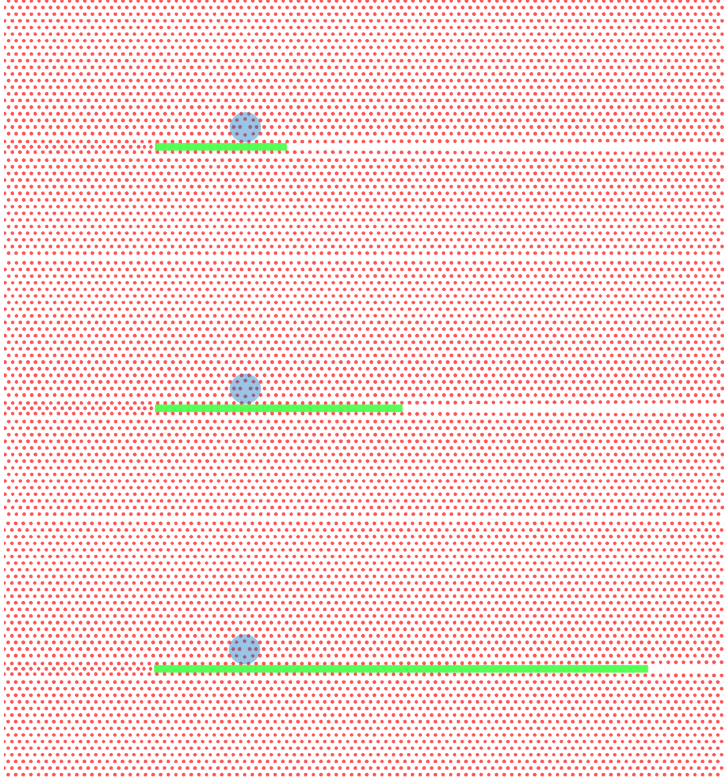


Figure 6.2: E-beam mask for the Fano lasers fabricated with three different lengths of embedded BH (the green rectangles), of $8\text{ }\mu\text{m}$, $15\text{ }\mu\text{m}$ and $30\text{ }\mu\text{m}$. The nanocavity is highlighted with the shaded blue area.

Table 6.1: Different hole shifts used to optimize the Fano laser cavity. All shifts are in nm.

	Cx_1y_0	Cx_2y_0	Cx_3y_0	Cx_4y_0
Δx	76	0	-4	-3
	Cx_0y_1	Cx_1y_1	Cx_2y_1	L_{1v}
$\Delta x, \Delta y$	0, 77	28, 16	0, 2	0, 79
	ss_1	ss_2	ss_3	ss_4
Δx	152	88	-14	-3

For the holes around the nanocavity a positive shift correspond to a shift away from the center of the nanocavity. For the row of circles closest to the waveguide a positive shift corresponds to a shift towards the center of the waveguide. For the endholes in the LD mirror a positive shift corresponds to a shift away from the LD cavity. All the shifts are highlighted in figure 6.1b

6.3 Experimental Characterization

First, the sample is characterised using the setup described in section 2.4, to obtain input/output curves and measure the spectra for the three different lengths. Figure 6.3 shows the output spectra for each BH length at maximum pump power for a hole radius of 120 nm. The spectra are resolution limited by the OSA at 1 nm³. First, it is noticed that the peak output powers are different for the three BH lengths, with the middle being lower in intensity. Secondly, the number of modes in the same spectral window differs between BH lengths. Specifically, the FL30 lasers with the longest BH are more single-moded, with a suppression ratio between the 1st and 2nd highest intensity modes of 35 dB. In the FL8 lasers with the shortest BH, two modes are very close in intensity, and there are modes at lower wavelengths that do not appear for the longest BH. The fabricated Fano design supports two Fano modes where there is strong field confinement to both the LD and nanocavity region. Usually, one of them has a much lower Q factor than the other, which experimentally results in only one of the modes being able to lase. For these samples, however, both modes appear in the spectra, at least for the two shorter BH lengths. The additional non-Fano modes could be an effect of the BH extending into the waveguide, where reflections at the edge of the BH can constitute the right mirror in a cavity.

Next, the threshold pump powers for the three different BHs are found, and they can be seen in table 6.2. The threshold pump powers are extracted from measurements for the three largest fabricated holes with radii from 118 nm to 120 nm. The FL30 laser with the largest hole radius is the one with the lowest laser threshold. The FL15 laser with a hole radius of 120 nm has two closely spaced modes, where the lower wavelength mode appears at lower input power, but the higher wavelength one can sustain

³Increasing the resolution limits the lowest input power where the peak can be detected. With a resolution of 1 nm better experimental data close to threshold can be obtained.

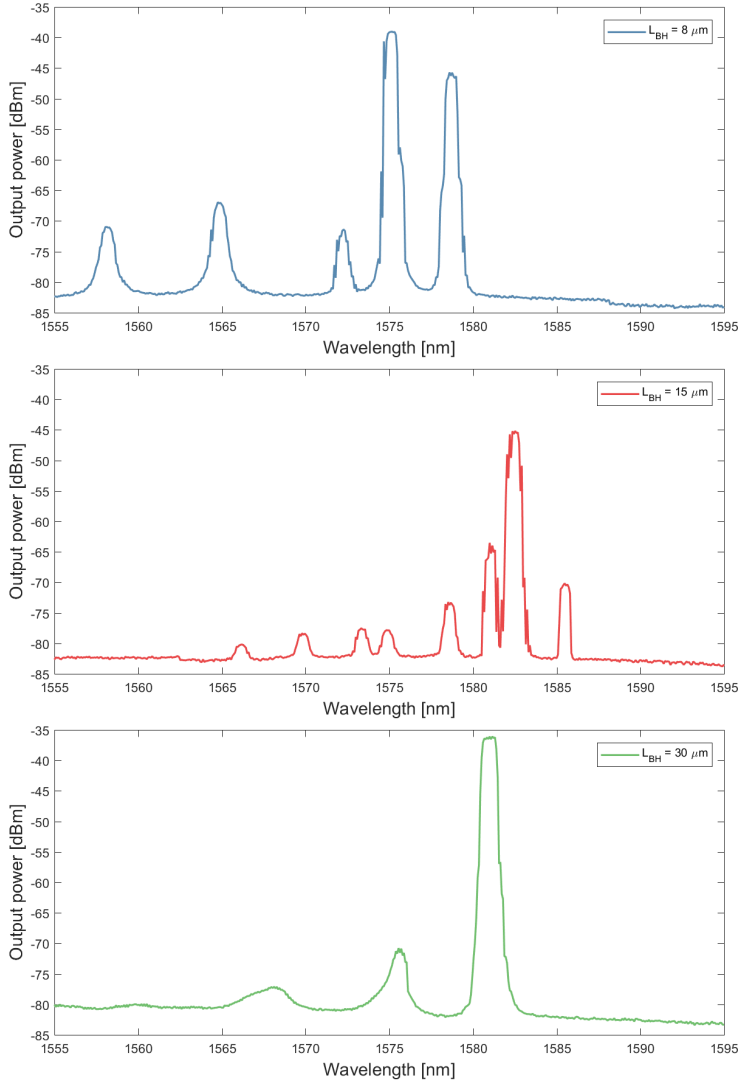


Figure 6.3: Spectra from the Fano lasers with a LD length of 11a and a hole radius of 120 nm for the three different BH lengths.

the highest output power. The loss of carriers to the competing mode results in a high laser threshold for the FL15.

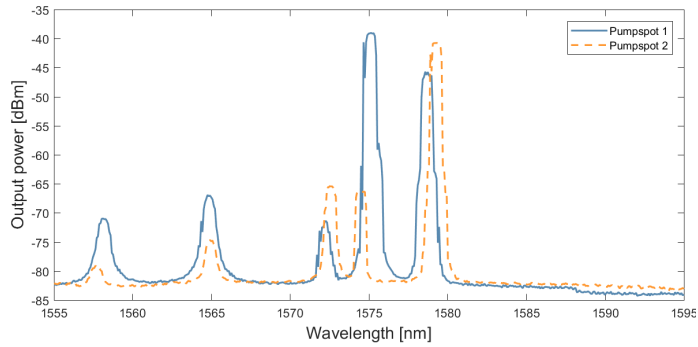
Table 6.2: Thresholds of nine Fano lasers with different hole radii and BH lengths.

	8 μm BH	15 μm BH	30 μm BH
118 nm	3.42 mW	5.80 mW	19.3 mW
119 nm	4.97 mW	2.83 mW	3.99 mW
120 nm	4.98 mW	11.2 mW ¹	2.47 mW

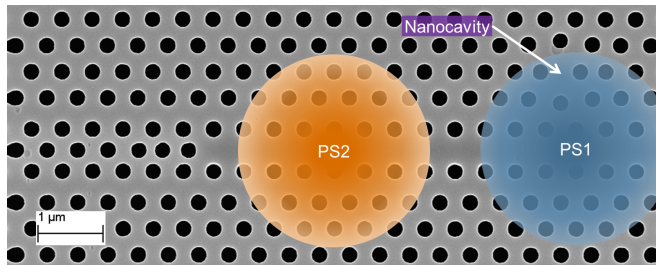
¹The high threshold pump power is due to the competing mode.

As described in section 2.4, the intensity measured is always very dependent on the pump spot position on the nanolaser. However, in the case with the three varying BH lengths, both the intensity and the output spectrum for the shortest and medium BH lengths changes significantly depending on the position of the pump spot on the nanolaser. Indeed, it is possible to position the pump spot so the pumping and collection of light from one or the other Fano modes are favored. Two spectra for different pump positions on the FL8 Fano laser with holes of radii 120 nm can be seen in figure 6.4a. A sketch of the two pump spot positions can be seen in figure 6.4b. Absorption of the optical pump power can cause small changes in the refractive index, which can change the coupling between the nanocavity and the LD cavity in the Fano laser, or the round-trip phase in the LD cavity. For the all-active device such changes were observed to change the output power and measured thresholds [95]. For the BH Fano lasers, the entire device can be tuned by shifting the pump spot, providing different mode selectivity, output powers and laser thresholds.

Next, our attention turns to the investigation of self-pulsation. To do so, the most intense peak for all the BH lengths is inspected with a higher resolution in a smaller spectral range for different



(a)



(b)

Figure 6.4: Changing the pump and collection position always affects the intensity measured, but for the FL8 lasers the spectrum also changes significantly, this can be seen in (a) for two different positions of the pump. (b) Sketch of the Fano laser with PS1 and PS2 representing the different position of the pump for the two spectra in (a).

pump powers. The result can be seen in figure 6.5⁴. First, it appears as though the peak becomes unstable⁵ at some input power. The reason could be self-pulsing⁶, or it could simply be due to thermal effects. The heating caused by the increased pump power causes a red-shift of the resonance wavelength, see e.g. figure 6b in [101], where the resonance wavelength red-shifts by 1.4 nm when the pump power is increased. While it appears that the laser with the medium length BH is stable through the entire pump sweep, it should be noted that the maximum output power for the medium BH is much lower than for the two other configurations. Comparing the spectra from the medium BH to spectra from either the long or short BH at comparable output power, they are all stable. Furthermore, it should be noted that the side peaks appearing for higher pump powers originate from interferometric noise caused by the beating between modes in the pump diode, and are not sample related. From the spectra alone, it is not possible to conclude whether the fabricated samples are self-pulsing.

To further investigate if the samples are self-pulsing, the setup described in section 2.4.2 is used to measure the intensity fluctuations of the nanolaser. If the intensity fluctuations are due to self-pulsing, i.e. a train of pulses with some repetition rate T impinges to the photodetector, the power spectrum should have discrete peaks spaced in frequency by $1/T$ [149]. Exactly this was observed in the original photonic crystal Fano laser demonstration [95], where a maximum repetition rate of 8 GHz was observed.

The longest BH with holes of radius 120 nm are investigated due to its strong mode suppression and its resonance wavelength. The measured RF spectrum can be seen in figure 6.6a. Here, two cascaded fiber amplifiers and bandpass filters have been used to pump the signal power to just below 0 dBm. Figure 6.6b shows the corresponding spectra measured on the OSA⁷. The RF

⁴See figure 3a in [95], for results on the Fano laser with QDs embedded everywhere.

⁵The resonance wavelength is no longer stable across the scan in the OSA.

⁶similar to what is seen in figure 3a in [95]

⁷A 20 dB splitter has been used so only a tenth of the power is sent to the OSA.

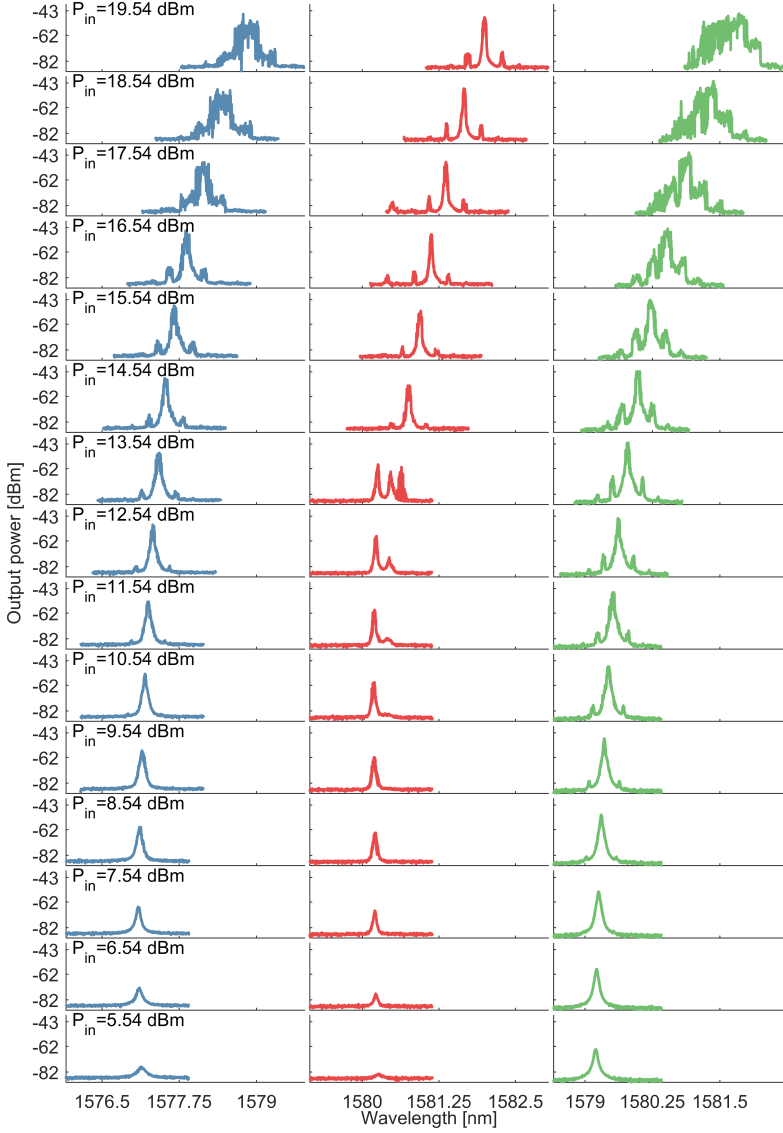


Figure 6.5: High resolution measurements of the Fano laser with hole radius 120 nm. From left to right the BH lengths are 8 μm (blue), 15 μm (red) and 30 μm (green) respectively. The input power for each row is shown in the top left of the corresponding row.

spectrum is rather flat and monotonous without any indication of self-pulsing, nor much else. The signal-to-noise ratio in the system also limits direct measurements of the RIN from the lasers, but the self-pulsing peaks observed earlier were strong enough to break through the noise floor to be measured. It should also be noted, that while theory predicts a strong suppression of the relaxation oscillations in Fano lasers [93], this suppression is not the immediate reason the relaxation oscillations does not appear in the measurements. Instead, the signal-to-noise ratio is simply too poor and the relaxation oscillation peak remains below the noise floor for standard LD cavities with similar output as well.

An effort was made to redo measurements on the older samples with quantum dots embedded everywhere and then the new samples with similar measurement setup configurations. However, the original Fano laser samples had degraded, providing maximum output powers of only -65 dBm. To observe self-pulsing in the all-active samples, the pump must be positioned so it does not pump the nanocavity, which further limits the output powers. Thus, the initial conclusion is that using a passive nanocavity to realize the Fano mirror renders the Fano laser in CW mode. The conclusion would be strengthened if a direct comparison could be made between the all-active Fano laser and the passive nanocavity Fano laser with the setup in exactly the same configuration.

6.4 FDTD investigation of buried heterostructure devices

As described above, the Fano laser requires optimisation of many individual hole positions to obtain a high quality factor of the Fano mode. The device optimisation prior to fabrication was carried out without consideration of the BH. Considering the results of the last chapter, the addition of a BH within the LD cavity of some length could impact the performance. This does appear to be the case, see figure 6.7, where the Q factor is shown

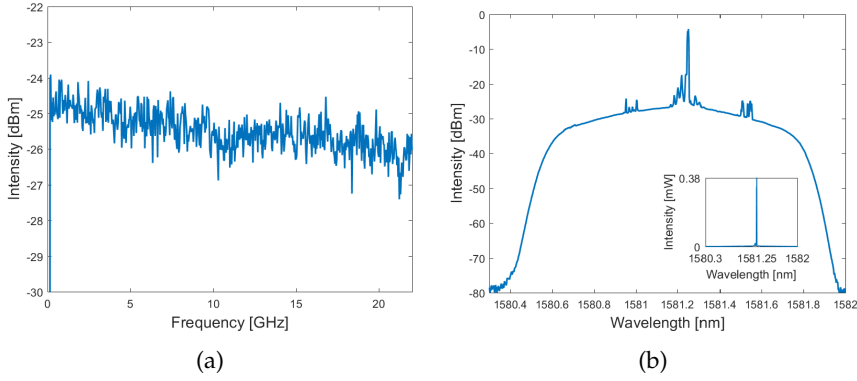


Figure 6.6: Investigation of self pulsing in the Fano lasers. (a) Radiofrequency measurement. The RF spectrum has no noticeable peaks. (b) High resolution spectra after amplification, bandpass filter and a 20 dB splitter. The sidepeaks are caused by fluctuations in pump power. The inset shows the spectrum on a linear scale.

for different lengths of BH in the LD cavity. The figure also shows BH lengths longer than the LD cavity, but apart from a small increase for a $14a$ long BH, the Q factor remains low. As can be seen in figure 6.7b[97], the Q-factor is halved if the effective cavity length is changed by just 10 nm. Thus, the buried heterostructure should be included the FDTD optimisations prior to fabrication. It also highlights how choosing a BH longer than the cavity can be preferable, to avoid further complexity.

Next, the modes appearing at the lower wavelength for the shortest BH is investigated numerically. The mode spacing, $\Delta\lambda$, is related to resonance frequency, λ_0 , the group index, n_g , and cavity length, L , by the free spectral range formula, $\Delta\lambda = \lambda_0^2 / (n_g L)$. Here the mode spacing is 6.72 nm, which then requires a group index for the mode of approximately 45, for the cavity length to match the BH length of $8\text{ }\mu\text{m}$ exactly. Such a group index might seem high at first glance but recall from the last chapter how the transition from a waveguide with embedded BH to a waveguide without can produce a strong reflection close to the band edge, due to the change of the photonic crystal locally. Thus, for

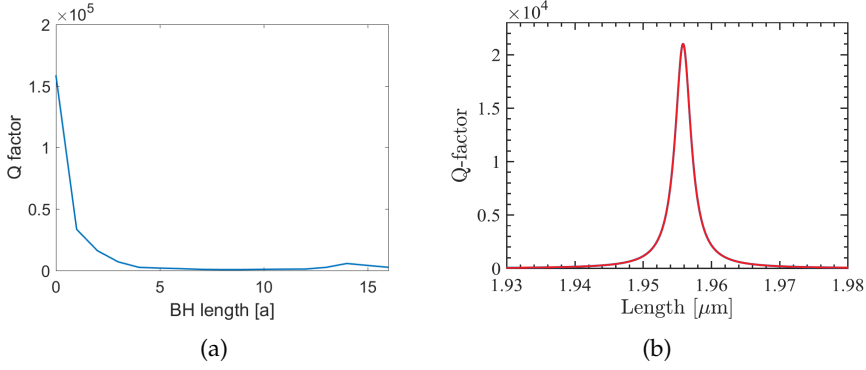


Figure 6.7: Q-factor investigations of the Fano cavity. (a) Simulations with varying lengths of BH embedded in the LD cavity. The Q-factor drops rapidly, but a small increase is observed for an $14a$ long BH. (b) The total Q-factor of the Fano mode is extremely dependent on the effective cavity length. From [97].

modes that are close to the bandedge, the group index can be large. Furthermore, the BH has a distinct endpoint determined by dry-etching, but the field can extend into the left photonic crystal mirror part, as described in chapter 4. Then the actual effective length of the cavity is longer than $8\mu\text{m}$, which relaxes the requirement on the group index slightly. Preliminary simulations of the dispersion relation, similar to those in chapter 4, for the photonic crystal waveguide with embedded BH have been made, and the group index for the mode at 1565 nm is found to be larger than 33. It seems then that the modes at lower frequency originate from a cavity made by the photonic crystal mirror and the BH edge. For longer BHs of $15\mu\text{m}$ the modes away from the high-intensity Fano modes are spectrally closer as is expected, if they originate from the BH. Furthermore, it should be noted that because the Fano resonance is very narrowband, the modes this far from the Fano resonance essentially pass straight by the H0 nanocavity. Lastly, for the longer BHs, a larger part of the BH remains unpumped, and the BH can act as an absorber for any light that passes into the waveguide. This can explain why the

peaks vanish for the longest BH, making the laser more single moded than the other BH lengths. For longer BH, more states need to be excited for population inversion, and the modes in the longest BH could possibly also be excited if a stronger optical pump was used.

6.5 Summary and outlook

Photonic crystal Fano lasers with a buried heterostructure gain material in the line defect cavity only was fabricated and characterized. The fabricated devices achieve lasing under optical pumping. Initial investigations shows a flat radiofrequency spectrum, and the self-pulsing behaviour of the previous samples [95] has vanished with the removal of the active material from the nanocavity. To further corroborate the experimental results, direct comparison between samples with an active and a passive nanocavity could be carried out. Furthermore, the length of the BH that spans into the waveguide was found to affect the output spectrum of the laser output, and produce additional modes. Two of the modes are Fano modes, where strong field confinement to both the LD and nanocavity is observed. Furthermore, there are additional modes with resonance wavelengths away from the discrete resonances of the nanocavity. The narrowband Fano mirror is transparent to these modes, and the right mirror is instead realised by the photonic crystal heterostructure at the edge of the BH. Numerically the Fano laser design was investigated with BH of varying lengths embedded in the LD cavity, and the simulations highlighted the critical optimisation required for a good Fano laser, as the Q factor drops dramatically as soon as the BH is embedded.

In the future, more samples and measurements are needed to conclude on the elimination of the self-pulsation. Here a new sample with embedded quantum dots everywhere could be fabricated to recreate the original sample design and measurements [95], so a direct comparison with the new BH samples can be

made. Another possibility is to fabricate Fano lasers on the same sample with and without a small BH embedded in the nanocavity region. If the two different lasers produce a CW and pulsed signal respectively the conclusion is straightforward. A few practical limitations lie in this approach. For samples with quantum wells, the BH alignment must be good enough that the BH does not protrude into the holes of the nanocavity, which limits the possible size of the BH. For samples with quantum dots, this requirement is less strict, but the samples fabricated with BH quantum dots do not yet lase. It remains unclear why the quantum dots samples are unable to lase, but in [102] it was suggested that the fabrication of the BH might damage the quantum dots. Secondly, numerical investigations show how embedding any form of BH in the nanocavity changes the resonance wavelength and Q factor. Thus, realizing two different laser configurations, with and without BH in the nanocavity, with similar coupling coefficients between the LD cavity, nanocavity and waveguide which is necessary for direct comparison, will require numerical investigations prior to fabrication. Such numerical investigations would benefit from a better characterization of the refractive index of the gain media so the simulated structures are more similar to the fabricated samples.

An investigation of the effect of the BH edge functioning as a partially transmitting element could also be conducted in the future, to determine how strong the effect is on the Fano resonance. Combining the Fano laser with the investigations in chapter 5 could also be an exciting way to gain further insight into the effects of the BH. The maximum gain achievable by a laser device is dependent on the laser resonance frequency and the gain spectrum, but with the nanocavity governing the resonance wavelength, only a slight resonance shift occurs between devices, resulting in the gain being more comparable between devices. While the resonance wavelength is robust to the changes in the cavity length, the Q-factor is not. Thus, the issue of the drop in Q factor when introducing the BH and changing its size must first be addressed. Ideally, this can be done by keeping the

nanocavity identical across lasers but changing the hole shifts in the left photonic crystal mirror to counter the effect from the BH. This can be investigated numerically prior to fabrication. The spatial resolution in hole shifts in the fabrication process is very good and such devices should be realizable.

CHAPTER 7

CONCLUSION AND OUTLOOK

This final chapter summarises the thesis, concludes on the main results and achievements and discusses future possibilities. Three distinct optically pumped photonic crystal laser devices were designed, fabricated and characterised and will be individually addressed. Final remarks and a future outlook for the photonic crystal lasers based on our material platform is offered.

Optimized line defect lasers with quantum dots

The reduction of laser threshold pump power is essential in enabling the use of photonic crystal lasers for on-chip interconnects, as it ultimately reduces the energy/bit. The first investigation of laser threshold of active devices as the Q-factor is optimised through hole-shifts was presented. The investigation highlights how optimisation of the cavity Q-factor leads to a reduction in the laser threshold. Line defect lasers with buried quantum dot gain material were fabricated. The first two endholes of the mirrors were shifted to optimise the cavity Q-factor, and the corresponding laser threshold measured. The fabricated devices had endhole shifts varied from $0a$ to $0.4a$ in steps of $0.05a$. The laser threshold was expected from simulations to be minimised for an endhole shift of $0.25a$, which was also observed experimentally. The minimum experimental threshold pump power was found to be limited by the internal loss in the cavity.

Furthermore, the maximum output power for cavities with different endhole shifts was measured. The maximum output power was experimentally found to decrease, following the same evolution as the laser threshold. The maximum output power decreased to less than half of the output power for the cavity without any hole shift. The laser rate equation model was used to predict the change in output power when the Q-factor changes due to endhole shifts. It is also necessary to include changes in the efficiency η_0 , as this parameter is strongly dependent on the Q-factor (mirror loss), and directly related to the output power. The model was shown to capture the evolution in output power observed experimentally. We note that, an increase in photon density in the cavity is predicted, but the decrease in vertical scattering loss is a stronger effect, ultimately limiting the output power. If a similar experiment is carried out for devices with a buried heterostructure gain material in the cavity and a side coupled waveguide the maximum in-plane output power could also be characterised. The in-plane output power is, of course, much more interesting from an application point of view.

A numerical investigation of the phase change occurring at the photonic crystal mirror and the penetration depth into the mirror was carried out. Here an equivalent 1D effective Fabry-Perot cavity model was used. The effective cavity length, L_{eff} , is composed of the physical cavity length $L = (N + 1)a$ and the penetration depth into the photonic crystal mirror, L_p , where N is the number of missing holes in the cavity and a is the photonic crystal period. When the endhole was shifted, the mirror phase was found to vary around π for an L5 cavity, and the absolute mirror phase increases with the cavity length. The shift in the mirror phase directly follows from the change in cavity resonance wavelength as the endholes are shifted. The penetration depth into the photonic crystal mirror was found to increase as the endhole shift is increased up to $0.25a$, after which it decreases, with a slight peak also occurring at $0.35a$. The penetration depth increases with the Q-factor, which is explained by a gentle confinement of the field as described in [79]. The penetration depth calculated from the

equivalent Fabry-Perot model is found to be around $1\text{ }\mu\text{m}$, which agrees well with results obtained directly from FDTD simulations. The numerical investigations suffer from poor resolution in the cavity resonance wavelength, which carries over to the mirror phase calculations and finally, the penetration depth calculations. The resolution can be improved by decreasing the endhole shift step further, i.e. including more simulations in the sweep between 0 and $0.4a$.

The internal loss in the devices is found to be a limiting factor. If new samples are fabricated with lower internal losses, the laser threshold can be further reduced. Variation in the laser threshold and output power was observed across devices. This variation can be reduced in future samples if the uniformity of devices is increased. Furthermore, the increment in endhole shifts can be reduced in future samples, so a device with an endhole shift closer to the predicted optimum can be fabricated. New samples can include different cavity lengths, such as L5, L7 and L9 so that the experimental results can be directly compared to the numerical investigations on the mirror phase and penetration depth. The optimisation can include shifts of more than the first endhole, which can serve to determine the minimum measurable laser threshold in our current setup. Finally, the optimisation can be done for cavities with the buried heterostructure gain material, and a side coupled waveguide, where light is then collected in-plane. The analysis of maximum in-plane output power would be vastly more useful than that of the out-of-plane carried out in this work. If such a device is fabricated, the coupling between the cavity and waveguide can be expected to change with the endhole shift, and careful modelling should precede the experimental investigation.

Buried heterostructure line defect lasers

Photonic crystal L7 line defect lasers with varying lengths of embedded buried heterostructure quantum well gain material

were fabricated and characterised. To date, only one other group in the world (NTT Basic Research Laboratories) has realised such devices. The maximum output power measured was just below 400 nW. Considering this is scattered light collected out-of-plane, the devices are truly state-of-the-art compared to [150].

Both a standard L7 cavity and an optimised L7 cavity with four shifted holes was investigated. All lasers with BHs longer than 1a could lase. With the sample analysed, no clear dependence of the laser threshold on the BH volume emerges. Outliers limit this result, specifically, the standard L7 design with a BH length of 3a and the optimised L7 design with a BH length of 6a. Furthermore, the gain material protrudes into the photonic crystal when the BH is longer than the cavity, and the current dry-etch does not etch the QWs, in which case the first holes of the mirror are not fully etched through the membrane.

While no clear evolution in the laser threshold was found as the BH length was varied, the resonance wavelength of the fabricated devices could be accurately determined by FDTD simulations on similar cavities with a passive BH of a different refractive index embedded.

FDTD simulations were carried out on a BH embedded in an open W1 waveguide, and an L7 cavity. The simulations on the open waveguides showed how a refractive index change forms a double heterostructure photonic crystal cavity with Q-factors as high as 1.8×10^7 and confine light to the BH area of the waveguide. The addition of the BH was found to redshift the resonance wavelengths above the bandedge of the photonic crystal without any BH. The resonance wavelength increases with the BH length, and it approaches the bandedge of the photonic crystal waveguide where the BH is embedded along the entire length. For shorter lengths of BH in the L7 cavity, an increase in intensity in the BH region was observed. Such an increase in field intensity in the gain material could increase the gain in fabricated devices.

In the future, open photonic crystal waveguides with embedded BHs of varying length can be fabricated and characterised. The

performance of the open waveguides with a double heterostructure formed by the BH can provide valuable insights into the active material. At the same time, the resonance wavelengths can be used to probe the effective refractive index of the BH and the bandgap of the photonic crystal. The sample design can also include more line defect cavity lengths to increase the certainty of the measurement.

The line defect lasers with BH fabricated here achieved lasing for BH lengths as short as $2a$. In the previous samples with quantum dot gain material embedded everywhere, such short line defect lasers have not consistently been able to achieve lasing.

It would be interesting to apply the mirror phase and penetration depth analysis to the BH line defect lasers as well, to investigate how a refractive index change in part of the cavity would impact the round-trip phase condition. For such an analysis to be effective, the BH lengths should be varied in smaller increments than the photonic crystal period.

The ability to push a line defect cavity resonance above the bandgap of the surrounding photonic crystal also merits further investigation. When electrical injection of carriers is achieved, an investigation of the variation of active material size inside a fixed-length line defect cavity would be more straightforward, as the dependence on the BH overlap with the pump spot is removed. The work was based on one of the first working samples with the embedded buried heterostructure, fabricated in-house at DTU Nanolab, where proper alignment between the BH and the cavities was achieved.

Buried heterostructure Fano lasers

Photonic crystal Fano lasers with embedded BH in the line defect cavity and open waveguide were fabricated and characterised. Experimental results confirm that the self-pulsing behaviour observed in previous samples [95] with quantum dots embedded everywhere, including the nanocavity, can be eliminated when

the nanocavity is purely passive and no longer acts as a saturable absorber. The length of BH that extends beyond the nanocavity, into the open waveguide was found to affect the output spectrum of the lasers. The addition of the BH to a waveguide can form a heterostructure which is responsible for additional modes appearing in the spectra, depending on the BH length. The Fano mirror is very narrowband, and as the modes confined to the BH are far away from the nanocavity resonance, the Fano mirror is essentially transparent to such modes.

Intensity fluctuations of the Fano lasers with BH were measured. The flat RF spectra show how a Fano laser with a passive nanocavity lases CW.

The Q-factor of the photonic crystal Fano laser is dependent on the total cavity length, and numerical investigations with BH embedded only in the line defect part of the Fano laser showed a drastic drop in the Q-factor due to the change in effective cavity length. Therefore, the optimisation of the device must be carried out with the embedded BH. This further highlights the importance of a good characterisation of the BH, so the refractive index used in simulations is close to that of real samples. The dependence of the Q-factor on the round-trip phase connects the investigation of the photonic crystal mirror phase to the Fano laser. Gaining a good understanding of the phase change occurring at the left mirror enables a more efficient design of the Fano laser.

The output power of the fabricated BH Fano laser devices exceeds the output power of the original samples with quantum dots embedded everywhere [95]. A direct comparison between the original sample that showed self-pulsing [95], and the new sample with BH and a passive nanocavity was not possible as the original sample had degraded and its output power was too low to measure the intensity fluctuations. In the future a new sample identical to the one used in the first experimental demonstration of the Fano lasers [95] can be fabricated, so a direct comparison with new BH samples can be made.

Instead, the BH technology enables the fabrication of Fano lasers both with and without BH embedded in the nanocavity

on the same sample. If the two lasers produce self-pulsing and CW light, respectively, the conclusion would be straightforward. As the nanocavity is very small, such a scheme would require proper alignment of the BH to the photonic crystal. The alignment requirement can be reduced if quantum dot BHs are used, as misalignment and protrusion into the photonic crystal holes are less detrimental for device performance. As long as the BH with quantum dots remain unable to lase, a different approach with a larger nanocavity, e.g. an H1, can be attempted.

The embedded BH forms a photonic crystal heterostructure, where light from the line defect cavity (or in the waveguide) with embedded BH is reflected at the BH edge if the wavelengths are above the bandgap of the passive photonic crystal waveguide. Thus, if the BH is terminated close to the nanocavity, it can act as a partially transmitting element. Such partially transmitting elements have been shown to alter the coupling between the field in the line defect and the nanocavity, which can change the spectrum of the Fano mirror [91, 148, 151]. Engineering the mirror spectrum can be useful in the future if the Fano laser is modulated by directly modulating the nanocavity, and understanding if the BH affects the mirror spectrum would be the next step in numerical and experimental investigations.

The novel ability of the all-active photonic crystal Fano laser to self-pulse can be utilised whenever a pulsed source is needed. However, the experimental demonstration of a pure CW Fano laser due to a passive nanocavity presented here truly highlights the richness of the photonic crystal Fano laser.

Final remarks and perspective

The photonic crystal laser platform with a buried heterostructure gain material has allowed us to fabricate of state-of-the-art devices, with a low threshold power, a high output power, and novel device characteristics. The addition of electrical injection to the device platform at DTU is currently being developed and will

further enable the realisation of novel devices. The Fano laser, in particular, is a rich system, and with electrical injection of carriers, the laser can be directly modulated via the bias applied to the gain material, or through the nanocavity, to exploit the strengths of the Fano laser fully. Furthermore, the Fano laser has been predicted to have a frequency modulation bandwidth orders of magnitude larger than traditional photonic crystal lasers and increased stability to reflections [93]. With electrical injection of carriers, both of these predictions can be experimentally investigated.

APPENDIX A

DEVICE FABRICATION PROCESS FLOW

On the following pages the complete fabrication procedure is presented along with the equipment, recipes and parameters used for each step.

If the sample is fabricated without the buried heterostructure, steps 3 (BH definition) and 4 (Alignment marks etching/sample protection) are skipped and there is no need for alignment during the e-beam exposure step.

Steps 1-4 was usually carried out by colleagues, while the remaining was carried out by the author.

Step Heading	Equipment	Procedure
1. Initial steps before bonding		
1.1. MOVPE sample growth		
1.1.1. Epitaxial growth	MOVPE	Grow InP with active QWs or QDs layers + In(x)Ga(1-x)As sacrificial layer ($x = 0.53$, $d = 200 - 250\text{nm}$)
1.1.2. PL characterization	PL mapper	532/980 nm, surface-map/wide-scan
1.2. Si thermal oxidation		
1.2.1. Thermal oxidation	Furnace: Anneal-oxide (C1)	Wet oxidation at 1100°C for 5h45min Annealing for 20min
1.2.2. SiO ₂ thickness measurement	Ellipsometer VASE	
2. Direct bonding		
2.1. Al₂O₃ deposition in ALD for realizing bonding interface		
2.1.1. Dummy run	ALD	Temperature: 250°C Deposition: $25x(\text{Al}_2\text{O}_3 + \text{H}_2\text{O})$, $4x\text{H}_2\text{O}$
2.1.2. Loading	ALD	Gently place wafers on the metal grid, close the chamber, evacuate
2.1.3. Deposition run	ALD	Temperature: 250°C Deposition: $25x(\text{Al}_2\text{O}_3 + \text{H}_2\text{O})$, $4x\text{H}_2\text{O}$
2.2. Wafer pre-bonding		
2.2.1. Si wafer unloading	Teflon bonding chuck	Place and align on the teflon chuck (face up), add the teflon corner tool on top
2.2.2. InP wafer unloading	Teflon bonding chuck	Position and align a few mm above the Si wafer (face down)
2.2.3. Putting in contact	Teflon bonding chuck	Release the InP wafer, let it drop on Si, guided by the teflon corner tool
2.2.4. Applying pressure	Teflon pressing tool	Quickly press with the Teflon pressing tool in the middle of the InP wafer, then press around
2.3. Wafer bonding in a wafer bonder		
2.3.1. Loading	Wafer Bonder 02	Place on the chuck
2.3.2. Bonding process	Wafer Bonder 02	Temperature: 300°C Force: 2 kN Pressure: vacuum Total time $\sim 2.5\text{ h}$

2.3.3. <i>Unloading</i>	Wafer Bonder 02	
2.4. Substrate removal		
2.4.1. <i>Wet etching</i>	HCl	Time: ~1 h Use magnetic stirrer for agitation
2.4.2. <i>Rinse</i>	DI water	
2.4.3. <i>Blow dry</i>	N ₂	
2.5. Stop layer removal		
2.5.1. <i>InGaAs wet etching</i>	H ₂ SO ₄ , H ₂ O ₂	Mixture: (10 %)H ₂ SO ₄ :H ₂ O ₂ = 1:1 Time: 30 s
2.5.2. <i>Rinse</i>	DI water	
2.5.3. <i>Blow dry</i>	N ₂	
2.6. PL mapping		
2.6.1. <i>Emission characterization</i>	PL mapper	532/980 nm, surface-map/wide-scan
2.7. Thickness mapping		
2.7.1. <i>Thickness estimation</i>	Ellipsometer VASE	Angle scan: 65° – 70° – 75° Acq. time: 5 s
3. BH definition		
3.1. Sample surface preparation before e-beam resist coating		
3.1.1. <i>Wet etching</i>	BHF	Time: >10 s
3.1.2. <i>Rinse</i>	DI water	
3.1.3. <i>Blow dry</i>	N ₂	
3.2. E-beam resist coating		
3.2.1. <i>Baking</i>	Hot plate	5 min, 220 °C
3.2.2. <i>Spin-coating</i>	HSQ Fox-15	60 s, 6000 RPM, 3000 /s ²
3.2.3. <i>Baking</i>	Hot plate	2 min, 120 °C 2 min, 220 °C
3.3. Buried heterostructure mask exposure in e-beam		
3.3.1. <i>Cassette loading</i>	E-beam	preferably 4" Ti cassette

3.3.2. <i>Pre-alignment</i>	E-beam pre-alignment stage	Choose good quality P and Q global alignment marks
3.3.3. <i>Exposure</i>	E-beam	Condition file: 45na_ap8 Dose: 3800 $\mu\text{C}/\text{cm}^2$, with PEC Alignment: P and Q global marks; chip marks for individual chips
3.4. <i>E-beam resist development</i>		
3.4.1. <i>Development</i>	AZ400K, H ₂ O	Mixture: AZ400K:H ₂ O = 1:3 Time: 2 min 40 s
3.4.2. <i>Rinse</i>	DI wafer	
3.4.3. <i>Blow dry</i>	N ₂	
3.5. <i>Formation of mesa-structures by dry etching</i>		
3.5.1. <i>Chamber preparation</i>	III-V ICP	Temperature: heat up to 180 °C Chamber cleaning: run 30 min O ₂ clean
3.5.2. <i>Chamber preconditioning</i>	III-V ICP	Recipe: ausa/"HBr etch (low p)" Time: 15 min Carrier: dummy 4" Si
3.5.3. <i>Dry etching</i>	III-V ICP	Recipe: ausa/"HBr etch (low p)" Time: 20 – 60 s
3.5.4. <i>Unloading</i>	DI water	Put into the glass beaker with DI water to neutralize Br
3.5.5. <i>Chamber cleaning</i>	III-V ICP	30 min O ₂ clean if no more InP etching is done
3.6. <i>Thickness mapping</i>		
3.6.1. <i>Thickness estimation</i>	Ellipsometer VASE	Angle scan: 65° – 70° – 75° Acq. time: 5 s
3.7. <i>Sample preparation for the 1st re-growth</i>		
3.7.1. <i>Plasma ashing</i>	Plasma Asher 1	5 min, 0.8 mbar, O ₂ = 300 ml/min, 400 W
3.7.2. <i>Cleaning/wet etching</i>	H ₂ SO ₄	Mixture: concentrated H ₂ SO ₄ Time: 3 min
3.7.3. <i>Rinse</i>	DI water	Time: 1 min
3.7.4. <i>Rinse (bubbler)</i>	DI water	Time: 3 min
3.7.5. <i>Blow dry</i>	N ₂	
3.8. <i>1st MOVPE re-growth (selective area growth)</i>		

3.8.1. <i>Sample loading into the load-lock</i>	MOVPE	Load and evacuate for >15 min
3.8.2. <i>InP regrowth</i>	MOVPE	Regrowth thickness: aiming for what was etched in III-V ICP + H ₂ SO ₄ cleaning/etching
3.9. Thickness mapping		
3.9.1. <i>Thickness estimation</i>	Ellipsometer VASE	Angle scan: 65° – 70° – 75° Acq. time: 5 s
3.10. E-beam resist removal from the buried heterostructure regions		
3.10.1. <i>Wet etching</i>	BHF	Time: 2 min
3.10.2. <i>Rinse</i>	DI water	
3.10.3. <i>Blow dry</i>	N ₂	
3.11. Sample preparation for the 2nd re-growth		
3.11.1. <i>Plasma ashing</i>	Plasma Asher 1	5 min, 0.8 mbar, O ₂ = 300 ml/min, 400 W
3.11.2. <i>Cleaning/wet etching</i>	H ₂ SO ₄	Mixture: concentrated H ₂ SO ₄ Time: 3 min
3.11.3. <i>Rinse</i>	DI water	Time: 1 min
3.11.4. <i>Rinse (bubbler)</i>	DI water	Time: 3 min
3.11.5. <i>Blow dry</i>	N ₂	
3.12. 2nd MOVPE re-growth (planarization)		
3.12.1. <i>Sample loading into the load-lock</i>	MOVPE	Load and evacuate for >15 min
3.12.2. <i>InP regrowth</i>	MOVPE	Re-growth thickness: aiming for 250 nm final InP membrane thickness and 50 nm InGaAs thickness
3.13. Thickness mapping		
3.13.1. <i>Thickness estimation</i>	Ellipsometer VASE	Angle scan: 65° – 70° – 75° Acq. time: 5 s
4. Alignment marks etching/sample protection.		
4.1. Adhesion promoting		
4.1.1. <i>Baking</i>	Hot plate	5 min, 100 °C
4.1.2. <i>Adhesion promoting</i>	Surpass 3000	1 min dip

4.1.3. Rinse (beaker)	DI water	1 min dip
4.1.4. Rinse	DI water	
4.1.5. Blow dry	N ₂	
4.2. AZ5214E spin coating		
4.2.1. AZ5214 spin coating	Spin coater: Gamma UV	10 s, 500 RPM, 1000 /s ² 30 s, 3000 RPM, 3000 / s ²
4.2.2. Wafer baking	Hot plate	90 s 90 °C
4.3. UV exposure		
4.3.1. UV exposure	Aligner MA6-2 (Süss MA6/BA6 contact mask aligner and bond aligner)	Mask “ BH PhC Alignment Marks 05 2017” Hard contact mode, Time 10s, Intensity 11-13 mW/cm ²
4.4. AZ5214E development		
4.4.1. Development	Developer: TMAH Manual	AZ726MIF: 2.38% TMAH 120 s
4.4.2. Rinse	DI water	For a few minutes
4.4.3. Blow dry	N ₂	
4.5. Surface preparation for wet etching		
4.5.1. Plasma ashing	Plasma Asher 1	20 s, 0.8 mbar, O ₂ = 300 ml/min, 400 W
4.5.2. Hard bake	Hot plate	120°C, 90s
4.6. InP etching around the alignment marks		
4.6.1. InP etch	1HCl : 4H ₃ PO ₄	1 min (with stirring)
4.6.2. Rinse	DI water	For a few minutes
4.6.3. Blow dry	N ₂	
4.7. Resist strip		

4.7.1. Stripping	Acetone	~5 min
4.7.2. Cleaning	IPA / ethanol	Rinse
4.7.3. Cleaning	DI water	Rinse
4.7.4. Blow dry	N ₂	
4.7.5. Plasma ashing	Plasma Asher 1	5 min, 0.8 mbar, O ₂ = 300 ml/min, 400 W

5. PhC definition

5.1. Hard-mask deposition

5.1.1. Test deposition	PECVD4	Recipe: "HF SiN with wafer clean" Time: ~17 min
5.1.2. Thickness estimation	Ellipsometer VASE	Determine SiN _x thickness and deposition rate on dummy Si
5.1.3. Real deposition	PECVD4	Recipe: "HF SiN with wafer clean" Time: ? min

5.2. E-beam alignment/exposure of photonic crystal patterns

5.2.1. Baking	Hot plate	5 min, 180 °C
5.2.2. Resist coating	ZEP520A	5 s, 500 RPM, 200 /s ² 60 s, 2600 RPM, 1500 /s ²
5.2.3. Baking	Hot plate	3 min, 180 °C
5.2.4. Cassette loading	JEOL JBX-9500FSZ	Preferably 2" Ti cassette, slot D
5.2.5. Pre-alignment	E-beam pre-alignment stage	Choose good quality P and Q global alignment marks
5.2.6. Exposure	JEOL JBX-9500FSZ	Condition file: 2na_ap4 Dose: 260 – 290 µC/cm ² , with PEC Alignment: P and Q global marks; chip marks for individual chips

5.3. E-beam resist development

5.3.1. Development	Developer: E-beam	Recipe: N-50-180s Developer: ZED N50 Rinsing: IPA Time: 3 min
--------------------	-------------------	--

5.4. Transfer of the photonic crystal patterns into the hard-mask

5.4.1. Chamber preparation	III-V ICP	Chamber cleaning: run 30 min O ₂ clean
----------------------------	-----------	---

5.4.2. Chamber preconditioning	III-V ICP	Recipe: "krsma/krsmaSiNx3" Time: 15 min Carrier: dummy 4" Si
5.4.3. Dry etching	III-V ICP	Recipe: "krsma/krsmaSiNx3" Time: 7-8 min
5.4.4. Chamber cleaning	III-V ICP	30 min O ₂ clean
5.5. E-beam resist strip		
5.5.1. Stripping	Ultrasonic bath	Mixture: Remover 1165 Level: 1 Temperature: <60 °C Time: 1 h
5.5.2. Cleaning	Acetone	~5 min
5.5.3. Cleaning	IPA	Rinse
5.5.4. Cleaning	Ethanol	Rinse
5.5.5. Blow dry	N ₂	
5.5.6. Plasma ashing	Plasma Asher 1	5 min, 0.8 mbar, O ₂ = 300 ml/min, 400 W
5.6. Transfer of the photonic crystal patterns into the InP layer		
5.6.1. Chamber preparation	III-V RIE	Chamber cleaning: 30 min vclean
5.6.2. Chamber preconditioning	III-V RIE	Recipe: precondition
5.6.3. Dry etching	III-V RIE	Recipe: cyc8ch42, 14 cycles
5.6.4. Chamber cleaning	III-V RIE	10 min O ₂ clean
6. Membranization		
6.1. Cleaving wafer into chips		
6.1.1. Cleaving	Cleaving fumehood	Manual cleaving
6.2. Membranization		
6.2.1. Wet etching	SiOetch	10 min
6.2.2. Rinse	DI water	

6.2.3. <i>Blow dry</i>	N ₂	
------------------------	----------------	--

APPENDIX B

AUTOMATED ANALYSIS OF HOLE SIZES FROM SEM IMAGES

The following MATLAB code is used to determine the average hole radius and the standard deviation across the holes analysed in the SEM image of the photonic crystal. The code requires five inputs:

1. `fullFileName` - The path to the SEM image.
2. `PxSize` - The pixel size of the SEM image, can be found in the annotation bar of the image.
3. `ExpectedR` - First guess of hole radius, used to determine a range of radii to fit circles.
4. `IterativeRadius` - Binary, explained below.
5. `Rfactor` - Factor used for the `IterativeRadius` approach.

If the code is used for multiple images, e.g. when analysing an array of radii fabricated to determine the fabrication factor, it is essential to make sure all SEM images are taken with the same pixel size. The pixel size can not be directly input when taking the images on the SEMs at DTU Nanolab, but the width of the image can and serves the purpose.

The IterativeRadius approach picks four of the holes at random and shows them along with the fitted circles, see figure B.1. An input dialog is then used to adjust the radii of all the holes. Each time the new radii is discarded, four new random holes are plotted, so the adjustment is unbiased.

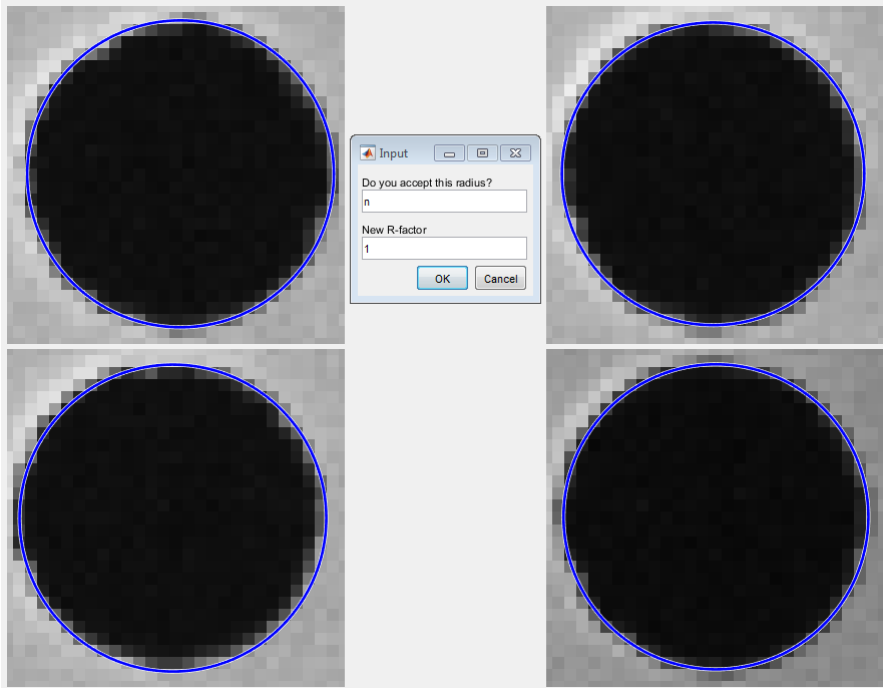


Figure B.1: Four random holes are plotted along with the fitted circles. An input dialog allows to adjust the radii of all holes by some factor.

```
%% Function for analysing photonic crystal hole
    diameters
% Written by Kristoffer S. Mathiesen 2017 –
    krsma@fotonik.dtu.dk
function [MeanR, StdR] = SEM_holesizes(fullFileName ,
    PxSize , ExpectedR , IterativeRadius , Rfactor)
fullImage = imread(fullFileName); %Load the full size
    SEM image
```

```
[frows, fcolumns, fnumberOfColorChannels] = size(
    fullImage); %Sizes of the fullsize image
originalImage = imread(fullFileName, 'PixelRegion', {[1
    frows-210],[1 fcolumns]}); % Cut out the SEM
    annotation bar
originalImageBar = imread(fullFileName, 'PixelRegion', {[
    frows-210 frows-15],[1 fcolumns]}); % Image
    annotation bar
originalImagePxSize = imread(fullFileName, 'PixelRegion'
    , {[frows-45 frows-20],[383 658]}); % Pixel size from
    SEM
ExpectedRinPx = ExpectedR/PxSize; %Calculate the
    expected radius in terms of pixels from the radius
    guess in [nm]

% Use the imfindcircles function to determine all
    circles in the SEM
[centers, radii, metric] = imfindcircles(imcomplement(
    originalImage), [floor(ExpectedRinPx*0.8) ceil(
    ExpectedRinPx*2)]);

% If the Iterative radius approach is used, the first
    inputs are defined
if IterativeRadius
    acceptR = 'n'; %Used for the while loop
    newRfactor = 1; %Don't change radii in the first
        imaging

    rfig = figure; %Open figure
    set(gcf, 'units', 'normalized', 'outerposition', [0 0 1
        1]); %Full screen figure

    while strcmp(acceptR, 'n') %A while loop for the
        iterative radius approach
        newradii = radii*newRfactor; %Update the radii
            of the circles
        MeanRpx = mean(newradii); %Update the mean radii
            in pixels
        rndHole = randi([1 length(centers)], 1, 4); %Find
            4 random holes for imaging
        for ii = 1:4 %Plot the 4 random holes
```

```

    subplot(2,2,ii) %2x2 image
    imshow(originalImage) %Display entire image
    axis image %Keep image aspect ratio
    viscircles(centers(rndHole(ii),:), newradii(
        rndHole(ii)), 'EdgeColor','b'); %Add the
        found circles
    %Isolate only one of the four random holes
    xlim([round(centers(rndHole(ii),1)-1.1*
        MeanRpx) round(centers(rndHole(ii),1)
        +1.1*MeanRpx)]);
    ylim([round(centers(rndHole(ii),2)-1.1*
        MeanRpx) round(centers(rndHole(ii),2)
        +1.1*MeanRpx)]);
end
%Create input dialog to either accept current
settings, or update them
UserInput = inputdlg({'Do you accept this radius
    ?','New R-factor'}, 'Input',1,{ 'n', num2str(
        newRfactor)});
acceptR = UserInput(1);
newRfactor = str2double(UserInput(2));
end
close(rfig) %Close figure

MeanR = MeanRpx*PxSize; %Then calculate the mean
radius
StdR = std(newradii)*PxSize; %And the standard
deviation

else %If the iterative radius approach is not used
MeanR = mean(radii)*PxSize; %Calculate the mean
radius
StdR = std(radii)*PxSize; %And the standard
deviation
end

end %End function SEM_holesizes

```

APPENDIX C

LASER RATE EQUATIONS BASED AUTOMATED FITTING TOOL

The following three MATLAB scripts can be used to generate fits from the rate equation model to experimental data. Using the Particle Swarm (PS) function in MATLAB, it continually tries to minimize the difference between the input-output curve generated from rate equations for a given set of parameters to the input-output curve from experimental measurement. The difference between the input-output curves defines the Goodness-of-Fit (GoF).

The first script defines all parameters, loads the experimental data, and calls the other scripts when running the particle swarms. The second script generates an input-output curve for the current parameter values and calculates the GoF. Here parameter combinations, that results in a laser threshold far different from that determined in experiments can be discarded. In this case, the GoF is set to some value $(200) +$ a random number between 0 and 1. The random number is added to make sure the particle swarm does not get stuck in a local minimum with $\text{GoF}=200$. The third script is used to generate the input-output curve for a given set of parameters from the laser rate equation model. The script below is based on the linear gain model evaluated at $N_0 = N/N_{tr}$, and could in the future be updated to use the better evaluation point of $N_0 = N_{th}/N_{tr}$.

Calling script

```

clc
clear all
close all

% Get current working directory
currentFolder = pwd;

%Constants:
h = 6.626070040e-34*1e6; %Plancks constant in [N.um.s]
c = 3e8*1e6; %Speed of sound in [um/s]

%Parameter generally not varied across optimizations
ng = 3.17; %Refractive index of InP, can also be from
simulations
vg = c/ng; %Group velocity, assuming no disperion (poor
approximation) [um/s]

%Laser parameter space:
PStruct.eta_0 = 1e-6*logspace(-2,2,101); %Optical
efficiency
PStruct.eta_i = 5e-4*logspace(-1,3,101); %Injection
efficiency
lambda_p = 1480e-9*1e6; %Pumping laser wavelength in [um
]
nu_p = c/lambda_p; %Pumping laser frequency in [Hz]
PStruct.tau_r = 2e-9; %Radiative lifetime [s]
PStruct.tau_nr = 20e-9; %Non-Radiative lifetime [s]
PStruct.g0 = 4.5e5*1e-6*logspace(-9,4,101); %Empirical
gain constant[1/um]
PStruct.Ntr = 2e18*1e-18; %Transparency carrier density
[1/um^3]
PStruct.beta = 1e-2*logspace(-2,1,101); %Beta factor

%Calculation dependent on laser length:
a = 438e-9*1e6; %PhC period [um]
r_PhC = 100e-9*1e6; %Radius of air holes in PhC [um]
Lc = 7; %Cavity length in terms of missing holes
Lcav = (Lc+1)*a-2*r_PhC; %Length of the cavity [um]
Wcav = 2*a*sin(pi/3)-2*r_PhC; %Width of the cavity [um]

```

```

Hcav = 250e-9*1e6; %Height of the membrane [um]
Vcav = Lcav*Wcav*Hcav; %Volume of the cavity (estimate
    for Vp, could be replaced by mode volume)

rho_QD = 4e14*1e-12; %Density of quantum dots in one
    layer [1/um^2]
nl = 3; %Number of layers of quantum dots
r_QD = 8e-9*1e6; %Radius of the quantum dots [um]
V = 2/3 * pi *r_QD^3 *rho_QD * nl *Wcav *Lcav; %Volume
    of all quantum dots, ie. active area [um^3]
Gamma = V/Vcav; %Confinement factor

PStruct.Q = 60000; %Quality factor of the PhC
lambda_l = 1573.8e-9*1e6; %Resonance wavelength of the
    laser [um]
nu_l = c/lambda_l; %Resonance wavelength of the laser [
    Hz]
PStruct.tau_p = PStruct.Q/(2*pi*nu_l); %Photon lifetime
    in the cavity [s]

%% Load the experimental data, must have the threshold
    already calculated;
load = 'D1078_2_Q3_S1_left_r82nm_0d00_PD.mat';

%% With limited parameter space
PthVec = [V, Gamma, vg];
skipData = find((PeakData.PeakPower>-88) < 1, 1, 'last')
    + 1; % Only fit data above 88 dBm

% Reduce the particle swarm function to only run in 4
    dimensions
reducedPS_fun = @(x) NODA_PS_fun(x(1),x(2),PStruct.tau_r
    ,PStruct.tau_nr,x(3),PStruct.Ntr,x(4),...
    PStruct.tau_p,nu_p,Lc,nu_l,...
    PeakData.PumpPower(skipData:end),PeakData.PeakPower(
    skipData:end),PeakData.threshold_fit*1e3,PthVec);

% Set upper and lower bounds of the PS
PS_lb = [PStruct.eta_0(1),PStruct.eta_i(1),PStruct.g0(1)
    ,PStruct.beta(1)];

```

```

PS_ub = [ PStruct.eta_0(end), PStruct.eta_i(end), PStruct.
          g0(end), PStruct.beta(end) ];

%% Particle swarms

% Set PS options
options = optimoptions('particleswarm','Display','off','
    SwarmSize',1000,'FunctionTolerance',1e-12,'
    MaxIterations',100000,'MaxStallIterations',1000);

% Initiation
numPS = 10; % Number of PS solutions
PS_params = nan(numPS,4); %Pre-allocation
PS_fval = nan(numPS,1); %Pre-allocation
exitflag = nan(numPS,1); %Pre-allocation

% Print progress bar
fprintf('Progress:\n');
progressMat = repmat(' ',1,numPS);
if numPS>10
    for kk = 1:9
        progressMat(round(kk*numPS/10)) = num2str(kk);
        progressMat(round(kk*numPS/10)+1) = '0';
    end
end
fprintf(['\n' progressMat '\n\n']);

% Run PS
for ii = 1:numPS
    [PS_params(ii,:), PS_fval(ii), exitflag(ii), output(
        ii)] = particleswarm(reducedPS_fun,4,PS_lb,PS_ub,
        options);

    % Live feed of the GoF result from each PS
    if PS_fval(ii) > 199
        fprintf('\b0\n');
    elseif PS_fval(ii)<199
        fprintf('\b1\n');
    else
        fprintf('\b|\n');
    end
end

```

```
end

% Exitflag indicates if the PS found a solution
if sum(exitflag) ~= numPS
    display('Not_all_particle_swarms_obtained_a_solution')
else
    display('All_particle_swarms_obtained_a_solution')
end

%% Save the .m file to avoid running the PS again:
save('PS_solution_workspace.mat');
```

Goodness-of-fit script

```

function GoF = NODA_PS_fun(eta_0,eta_i,tau_r,tau_nr,g0,
    Ntr,beta,tau_p,nu_p,Lc,nu_l,Pin_dBm,Pout_dBm_data,
    Pth_data,PthVec)

h = 6.626070040e-34*1e6; %Plancks constant in [N.um.s]

% Defining the parameters from the threshold vector
V = PthVec(1);
Gamma = PthVec(2);
vg = PthVec(3);

% Calculating threshold from current parameters
Pth_curParam = h*nu_p*V/eta_i*(1/tau_r+1/tau_nr)*(Ntr/(
    tau_p*Gamma*vg*g0)+Ntr);

% If the threshold of current parameters are within +-
    10 mW
if Pth_curParam > Pth_data-10*1e3 && Pth_curParam <
    Pth_data+10*1e3
    % Generate output curves for the parameters
    This_Pout_dBm = NODA_RLssLG_Fun(eta_0,eta_i,tau_r,
        tau_nr,g0,Ntr,beta,tau_p,nu_p,Lc,nu_l,Pin_dBm);
    % Find the goodness of fit (GoF)
    GoF = sum(abs(This_Pout_dBm-Pout_dBm_data));
else % Set the GoF as 200 + rand(1), the rand(1) is to
    keep the PS running
    GoF = 200+rand(1);
end

```

Rate-equation script

```
function [Pout_dBm, Np, N] = NODA_RLssLG_Fun(eta_0, eta_i  
    , tau_r, tau_nr, g0, Ntr, beta, tau_p, nu_p, Lc, nu_l, Pin_dBm)
```

```
%Constants:
```

```
h = 6.626070040e-34*1e6; %Plancks constant in [N.um.s]
```

```
c = 3e8*1e6; %Speed of sound in [um/s]
```

```
q = 1.602e-19; %Elementary charge [C]
```

```
%Parameter generally not varied across optimizations
```

```
ng = 3.17; %Refractive index of InP
```

```
vg = c/ng; %Group velocity [um/s]
```

```
%Calculation dependent on laser length:
```

```
a = 438e-9*1e6; %PhC period [um]
```

```
r_PhC = 95.7e-9*1e6; %Radius of air holes in PhC [um]
```

```
Lcav = (Lc+1)*a-2*r_PhC; %Length of the cavity [um]
```

```
Wcav = 2*a*sin(pi/3)-2*r_PhC; %Width of the cavity [um]
```

```
Hcav = 250e-9*1e6; %Height of the membrane [um]
```

```
Vcav = Lcav*Wcav*Hcav; %Volume of the cavity (estimate  
    for Vp, could be replaced by mode volume)
```

```
rho_QD = 4e14*1e-12; %Density of quantum dots in one  
    layer [1/um^2]
```

```
nl = 3; %Number of layers of quantum dots
```

```
r_QD = 8e-9*1e6; %Radius of the quantum dots [um]
```

```
V = 2/3 * pi * r_QD^3 * rho_QD * nl * Wcav * Lcav; %Volume  
    of all quantum dots, ie. active area [um^3]
```

```
Gamma = V/Vcav; %Confinement factor
```

```
% Calculate input powers to be solved
```

```
Pin_uW = 10.^(Pin_dBm/10)/1000*1e6; %Input pump power [N  
    .um/s = uW]
```

```
%Pre-allocate the vectors for the output
```

```
N= zeros(1,length(Pin_uW));
```

```
Np= zeros(1,length(Pin_uW));
```

```
Pout= zeros(1,length(Pin_uW));
```

```
Pout_dBm= zeros(1,length(Pin_uW));
```

```

%% Solve the equation
A = vg*g0*tau_p*Gamma/Ntr*((1-beta)/tau_r + 1/tau_nr);
B = -(1/tau_r+1/tau_nr)-vg*g0*tau_p*Gamma/Ntr*(eta_i*
    Pin_uW/(h*nu_p*V)+Ntr*(1-beta)/tau_r+1/tau_nr);
C = eta_i*Pin_uW/(h*nu_p*V)*(1+vg*g0*tau_p*Gamma);
D = B.^2-4*A*C;

%The two solutions
Nplus = (-B+sqrt(D))/(2*A);
Nminus = (-B-sqrt(D))/(2*A);

%Solution is always Nminus
N = Nminus;
Np = tau_p*Gamma*(eta_i*Pin_uW/(h*nu_p*V)-N*((1-beta)/
    tau_r+1/tau_nr));

%% Calculate the output power
Pout = eta_0*h*nu_l*Np*Vcav/tau_p; %This is in uW
Pout_dBm = 10*log10(Pout*1e-3);

```

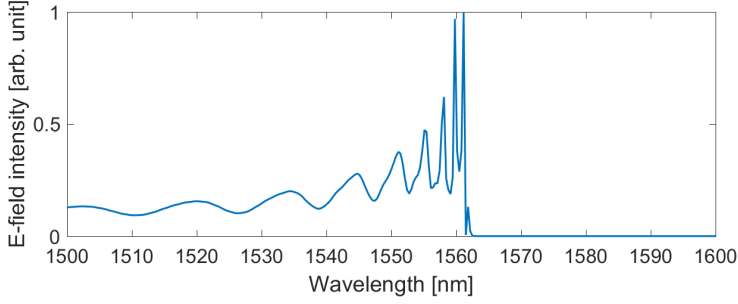
APPENDIX D

MORE SIMULATION RESULTS ON PHOTONIC CRYSTALS WITH EMBEDDED BH

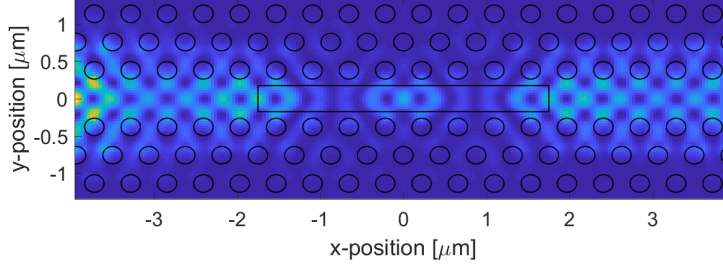
For some readers the figures with mode profiles from the different simulation might merit a closer inspection and are thus included in this appendix chapter.

D.1 Transmission through a waveguide with embedded BD

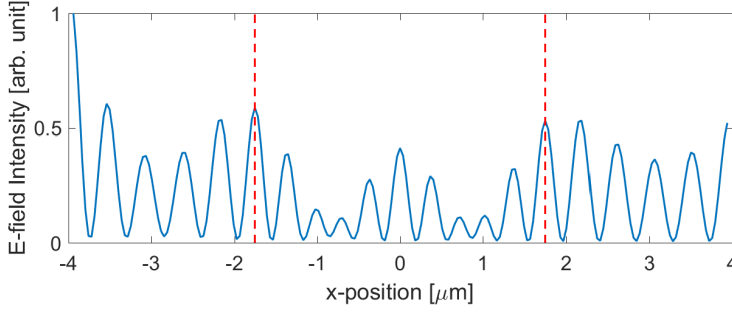
The following is based on the transmission through an open waveguide with a BH embedded of some length. Figure [D.1](#) shows the result for an $8a$ long BH. Figure [D.1a](#) shows the electric field intensity measured by a time monitor placed in the center of the BH. The intensity peaks close to the bandedge of the passive photonic crystal waveguide. The electric field intensity for the peak in intensity at 1561.2 nm is seen in 2D in figure [D.1b](#) and in 1D through the horizontal cavity midline in figure [D.1c](#). The field intensities are stronger outside the BH and the observed field profile can not be described as field confinement. This is explained by the light source being in the waveguide far away from the BH. The light source can efficiently couple wavelengths longer than the open waveguide bandgap into the waveguide, so it is most likely caused by simple reflection at the BH edge.



(a) Field intensity from the time monitor embedded in the BH.



(b) Normalized electric field intensity at 1561.2 nm



(c) Electric field intensity through the horizontal cavity midline.

Figure D.1: Transmission simulations of an open waveguide with an embedded BH of length $8a$. The electric field intensities in (b) and (c) are recorded at at the wavelength 1561.2 nm. Red dashed lines indicate the BH edge.

D.2 BH in a waveguide excited with dipoles

The results in the following section are based on the simulations with the BH embedded in a photonic crystal waveguide, where the modes are excited by dipole sources. The mode profile and field intensity along the waveguide for a completely open waveguide, i.e. no BH, can be seen in figure D.2. The figure shows that the mode eventually confined to the BH is originally a standing wave in the entire waveguide, which must occur close to the bandedge for the reflections at the waveguide ends to be strong enough to form a cavity. Figure D.3 shows the mode profile when sweeping across BH from $1a$ to $8a$.

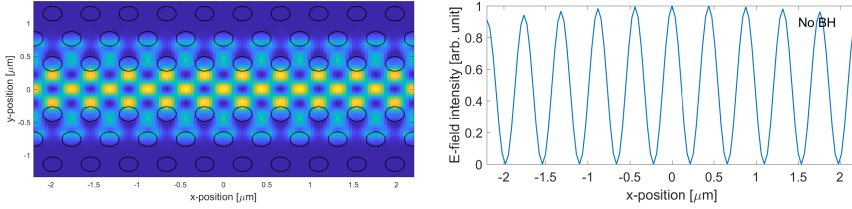


Figure D.2: Mode profile and field intensity along the waveguide in the simulation without the BH.

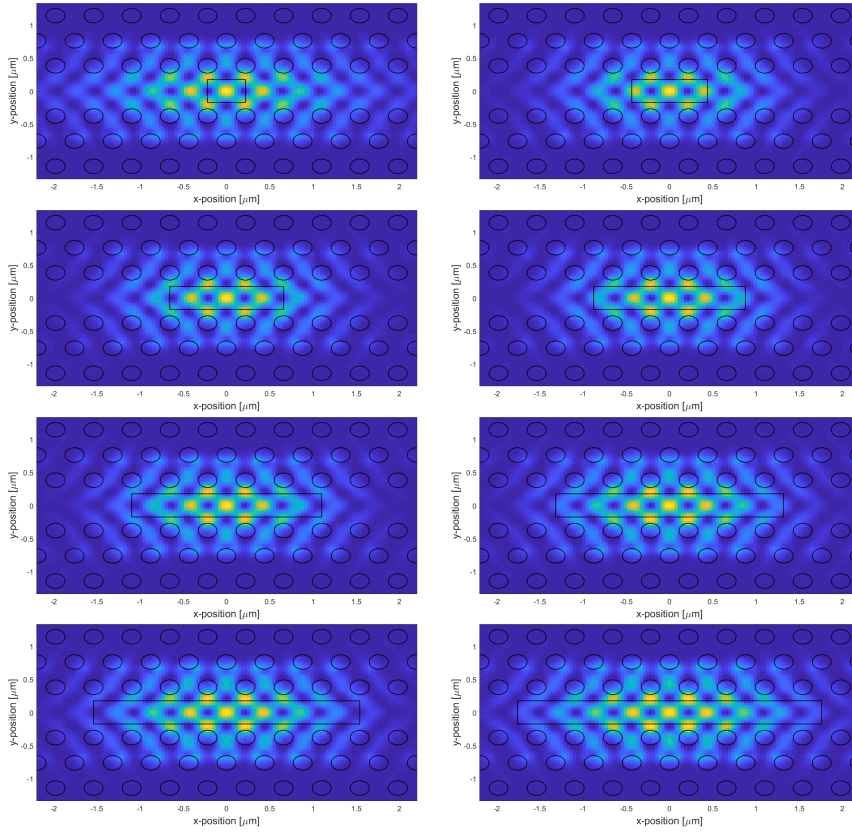


Figure D.3: Mode profile for varying BH lengths from $1a$ to $8a$.

D.3 L7 cavity with embedded BH

The results in the following section are based on simulations on the L7 cavity with embedded BH of varying lengths. Figure D.4 shows the difference in field intensities $|E|^2$, between the cavity without any BH and the cavities with varying lengths of BH highlights the effect. It is an extension of Figure 5.10 in the main text, here with more steps in the BH length. Figure D.5 shows the 2D mode profile of the dominant mode for BH varying from no BH to $7a$, and figure D.6 shows the 1D intensity through the center of the cavity for the same BH range. Similar plots can be found in figures D.7 and D.8 for the 2nd order mode, where a similar pattern is seen.

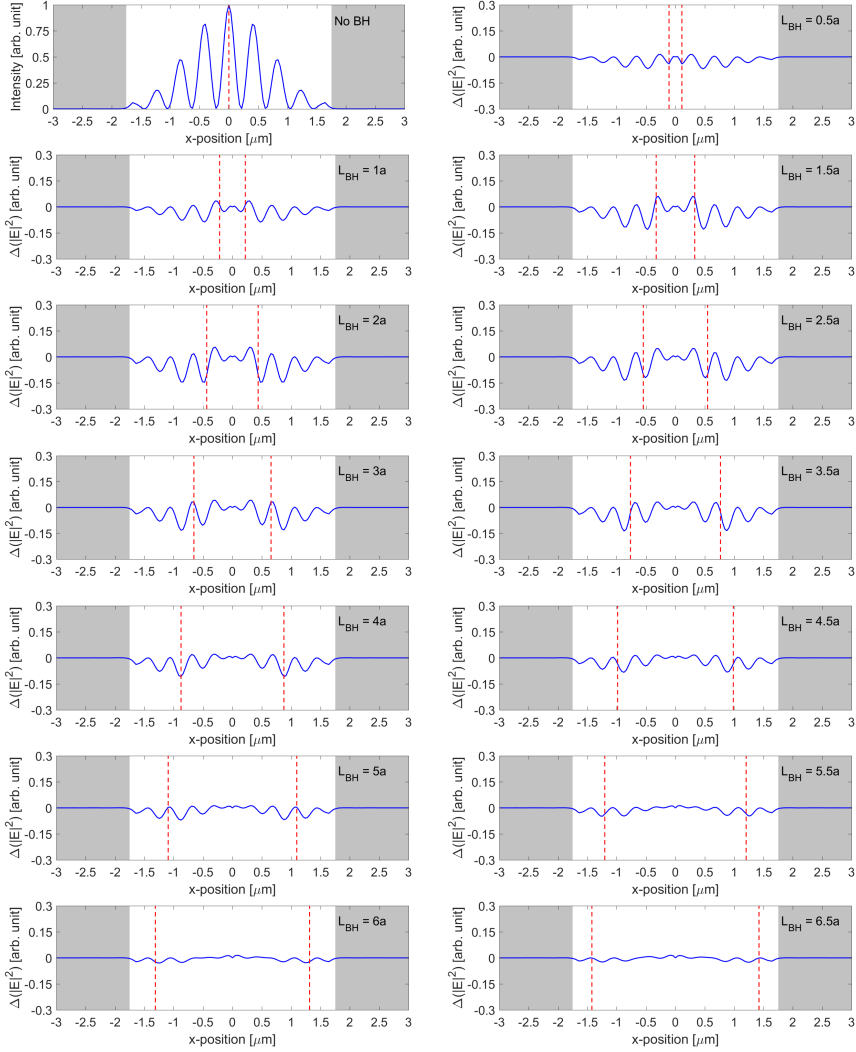


Figure D.4: Top left: E-field intensity $|E|^2$ for the L7 cavity without BH. Rest: Difference in normalised E-field intensity $\Delta(|E|^2)$, between the cavity without BH and the cavity with varying lengths of BH embedded. The red dotted lines indicate the edges of the BH and the grey shaded area indicates the edge of the cavity. The addition of the BH perturbs the field, close to the edges of the BH. As the BH fills the L7 cavity, the effect diminishes.

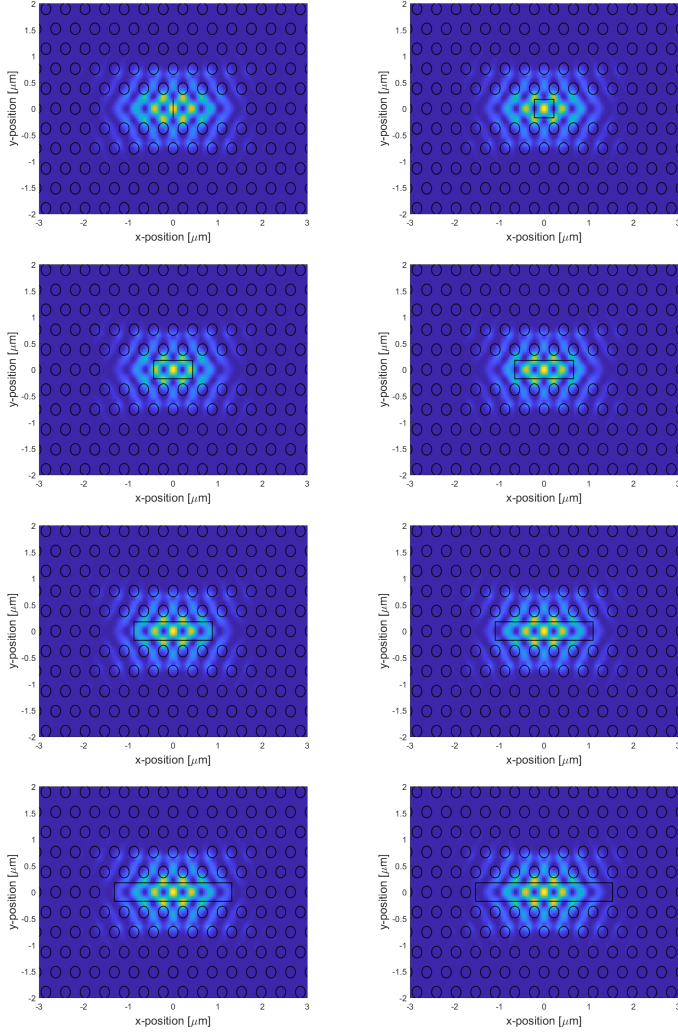


Figure D.5: Mode field profiles for the strongest resonance in the L7 cavities with embedded BH for varying lengths of BH.

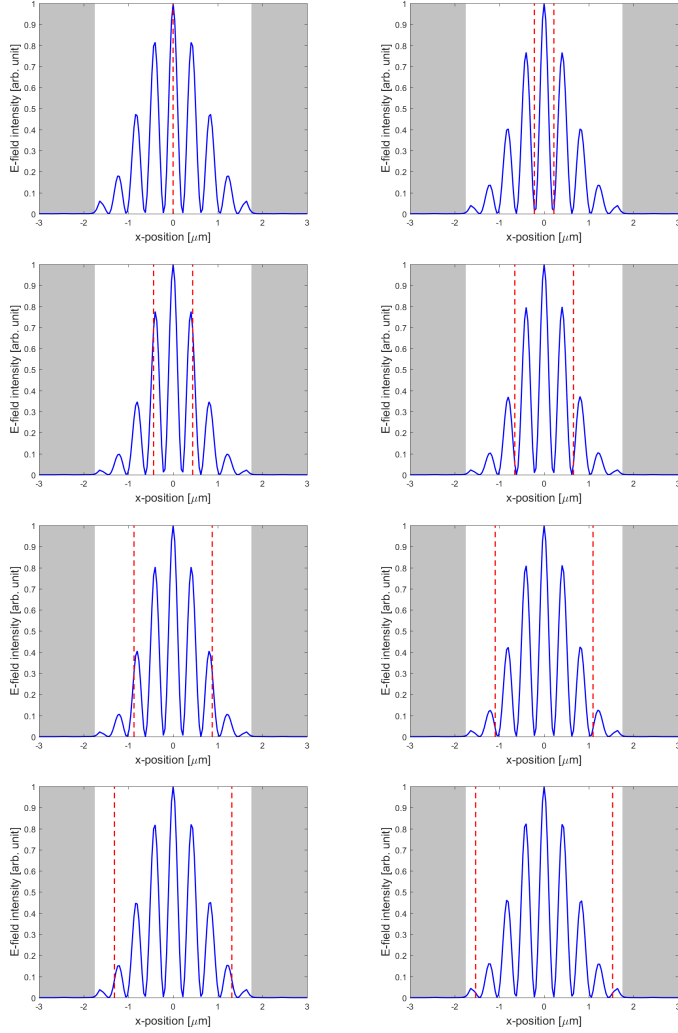


Figure D.6: Field intensity along the LD for the strongest resonance in the L7 cavities with embedded BH for varying lengths of BH.

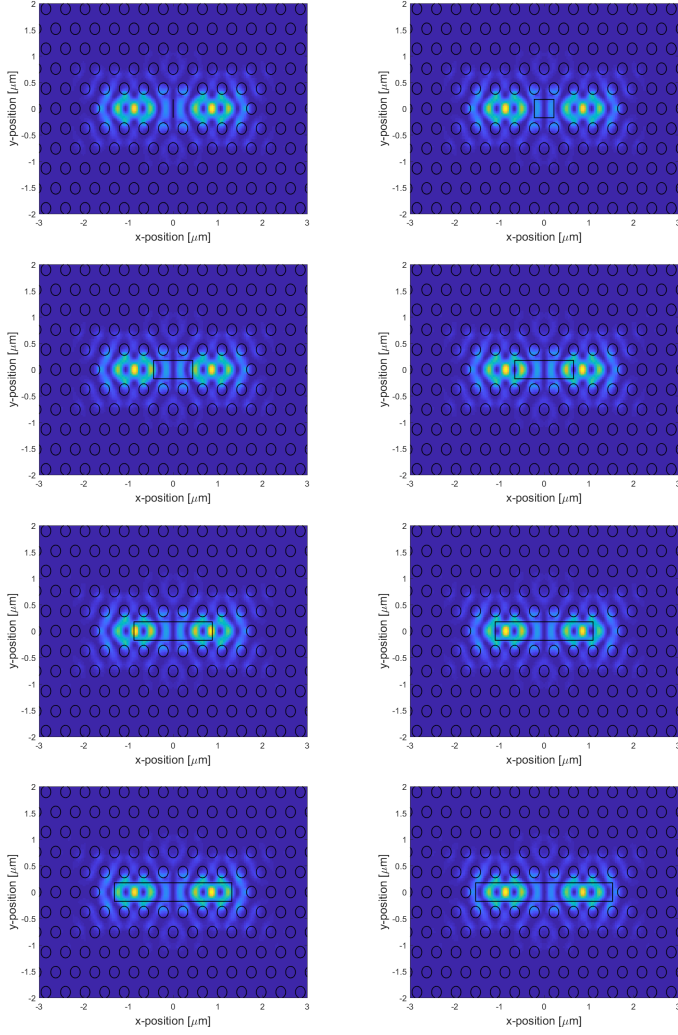


Figure D.7: Mode field profiles for the 2nd order mode in the L7 cavities with embedded BH for varying lengths of BH.

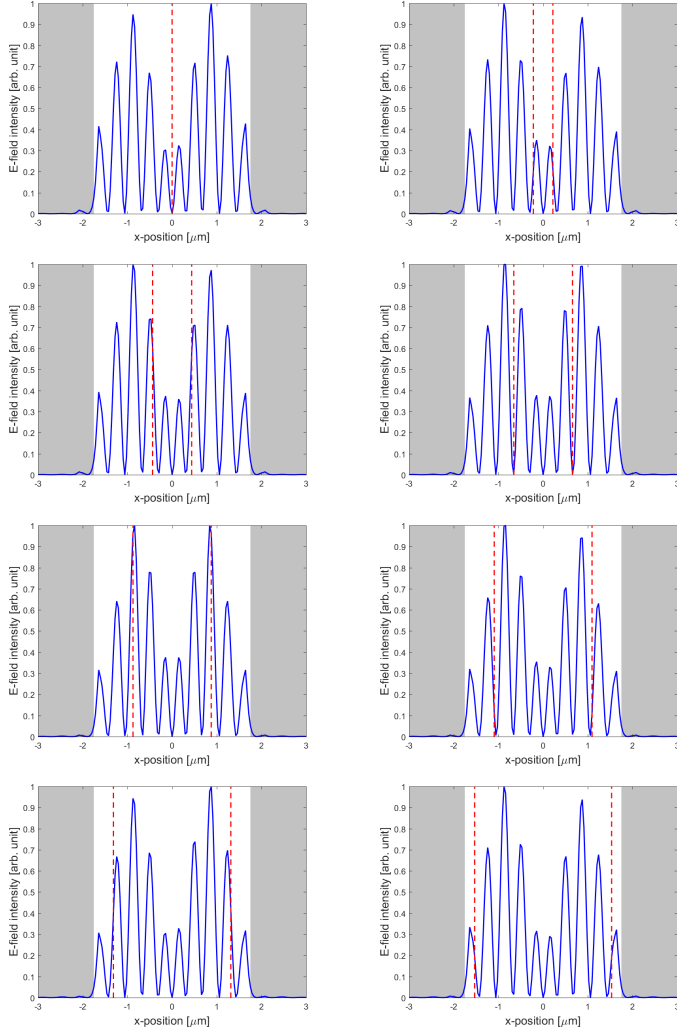


Figure D.8: Field intensity along the LD for the 2nd order mode in the L7 cavities with embedded BH for varying lengths of BH.

Bibliography

- [1] D. Miller. "Device Requirements for Optical Interconnects to Silicon Chips". *Proceedings of the IEEE* 97.7 (July 2009), pp. 1166–1185.
- [2] Greg Astfalk. "Why optical data communications and why now?" *Applied Physics A* 95.4 (June 2009), pp. 933–940.
- [3] David A. B. Miller. "Attojoule Optoelectronics for Low-Energy Information Processing and Communications". *Journal of Light-wave Technology* 35.3 (2017), pp. 346–396.
- [4] G M Moore. "Moore's Law ,Electronics". *Electronics* 38.8 (1965), p. 114.
- [5] Robert H. Dennard et al. "Design of Ion-Implanted MOSFET's With Very Small Physical Dimensions". *IEEE Journal of Solid-State Circuits* 9.5 (1974), pp. 256–268.
- [6] M. Mitchell Waldrop. "More Than Moore". *Nature* 530.7589 (Feb. 2016), pp. 144–147.
- [7] Nir Magen et al. "Interconnect-power dissipation in a microprocessor". *Proceedings of the 2004 international workshop on System level interconnect prediction - SLIP '04*. ACM Press, 2004, p. 7.
- [8] ITRS 2.0. "International Technology Roadmap for Semiconductors, Executive Report" (2015).
- [9] Wolfgang Arden et al. "More-than-Moore" White Paper. ITRS, 2010.
- [10] IRDS. "International Technology Roadmap for Devices and Sytems" (2018).

- [11] Vignesh Adhinarayanan et al. "Measuring and modeling on-chip interconnect power on real hardware". *Proceedings of the 2016 IEEE International Symposium on Workload Characterization, IISWC 2016*. Institute of Electrical and Electronics Engineers Inc., Oct. 2016, pp. 23–33.
- [12] Sandvine Incorporated ULC. *The Global Internet Phenomena Report: October 2018*. October. 2018, p. 23.
- [13] Gary Cook et al. *CLICKING CLEAN : WHO IS WINNING THE RACE TO BUILD A GREEN INTERNET ?* Ed. by Nancy Bach and Elizabeth Jardim. Greenpeace Inc., 2017.
- [14] Lasse Foghsgaard. "Hvis Netflix var et køleskab, skulle det have energimærke D". *Politiken* (Dec. 2018).
- [15] Reality Check Team. "Climate change: Is your Netflix habit bad for the environment?" *BBC News* Oct (2018).
- [16] Miyuru Dayarathna, Yonggang Wen, and Rui Fan. "Data center energy consumption modeling: A survey". *IEEE Communications Surveys and Tutorials* 18.1 (2016), pp. 732–794.
- [17] Anders Andrae and Tomas Edler. "On Global Electricity Usage of Communication Technology: Trends to 2030". *Challenges* 6.1 (Apr. 2015), pp. 117–157.
- [18] Cisco Systems Inc. "Cisco Visual Networking Index: Forecast and Trends, 2017–2022 White Paper". *Cisco Forecast and Methodology* (2019).
- [19] Ward Van Heddeghem et al. "Trends in worldwide ICT electricity consumption from 2007 to 2012". *Computer Communications* 50 (Sept. 2014), pp. 64–76.
- [20] Erol Gelenbe and Yves Caseau. "The impact of information technology on energy consumption and carbon emissions". *Ubiquity* June (2015), pp. 1–15.
- [21] *ATAG.org Facts & figures*. (Visited on 02/07/2020).
- [22] David A. B. Miller. "Physical reasons for optical interconnection". *International Journal of Optoelectronics* 11.3 (1997), pp. 155–168.

- [23] Ashok V. Krishnamoorthy et al. "Progress in low-power switched optical interconnects". *IEEE Journal on Selected Topics in Quantum Electronics* 17.2 (2011), pp. 357–376.
- [24] Joseph W. Goodman. "Optical Interconnections for VLSI Systems". *Proceedings of the IEEE* 72.7 (1984).
- [25] P.R. R. Haugen et al. "Optical Interconnects For High Speed Computing". *Optical Engineering* 25.10 (Oct. 1986), pp. 1076–1085.
- [26] L. D. Hutcheson. "High Speed Optical Interconnect Development". *High Frequency Optical Communications*. Vol. 0716. February 1987. 1987, p. 32.
- [27] Paolo Minzioni et al. "Roadmap on all-optical processing". *Journal of Optics* 21.6 (June 2019), p. 063001.
- [28] Masaya Notomi et al. "Toward fJ/bit optical communication in a chip". *Optics Communications* 314 (2014), pp. 3–17.
- [29] Keren Bergman et al. *Photonic Network-on-Chip Design*. Ed. by Anantha P. Chandrakasan. Vol. 68. Springer, 2014.
- [30] Shinji Matsuo and Takaaki Kakitsuka. "Low-operating-energy directly modulated lasers for short-distance optical interconnects". *Advances in Optics and Photonics* 10.3 (Sept. 2018), p. 567.
- [31] Shinji Matsuo et al. "Ultralow operating energy electrically driven photonic crystal lasers". *IEEE Journal on Selected Topics in Quantum Electronics* 19.4 (2013).
- [32] Werner H. Hofmann, Philip Moser, and Dieter Bimberg. "Energy-efficient VCSELs for interconnects". *IEEE Photonics Journal* 4.2 (2012), pp. 652–656.
- [33] Gyeong Cheol Park et al. "Hybrid vertical-cavity laser with lateral emission into a silicon waveguide". *Laser & Photonics Reviews* 9.3 (May 2015), pp. 11–15.
- [34] Martin T. Hill and Malte C. Gather. "Advances in small lasers". *Nature Photonics* 8.12 (2014), pp. 908–918.
- [35] A. Polman et al. "Ultralow-threshold erbium-implanted toroidal microlaser on silicon". *Applied Physics Letters* 84.7 (2004), pp. 1037–1039.

- [36] J. Liu et al. "Random nanolasing in the Anderson localized regime". *Nature Nanotechnology* 9.4 (2014), pp. 285–289.
- [37] Myung-Ki Kim, Amit M. Lakhani, and Ming C. Wu. "Efficient waveguide-coupling of metal-clad nanolaser cavities". *Optics Express* 19.23 (2011), p. 23504.
- [38] Soon Hong Kwon, Hong Gyu Park, and Yong Hee Lee. "Photonic Crystal Lasers". *Semiconductors and Semimetals*. Ed. by James J. Coleman, A. Catrina Bryce, and Chennupati Jagadish. Vol. 86. 2012. Chap. 8, pp. 301–333.
- [39] O. Painter et al. "Two-dimensional photonic band-gap defect mode laser". *Science* 284.5421 (1999), pp. 1819–1821.
- [40] Fabrice Raineri, Alexandre Bazin, and Rama Raj. "Optically Pumped Semiconductor Photonic Crystal Lasers". *Compact Semiconductor Lasers*. Ed. by Richard M. De La Rue, Siyuan Yu, and Jean-Michel Lourtioz. 2014. Chap. 2, pp. 33–90.
- [41] Xavier Checoury, Raffaele Colombelli, and Jean Michel Lourtioz. "Electrically Pumped Photonic Crystal Lasers: Laser Diodes and Quantum Cascade Lasers". *Compact Semiconductor Lasers*. Ed. by Richard M. De La Rue, Siyuan Yu, and Jean-Michel Lourtioz. 2014. Chap. 3, pp. 91–148.
- [42] Dimitris Fitsios and Fabrice Raineri. "Photonic Crystal Lasers and Nanolasers on Silicon". *Semiconductors and Semimetals*. Ed. by Sebastian Lourdudoss, Ray T. Chen, and Chennupati Jagadish. 1st ed. Vol. 99. Elsevier Inc., 2018. Chap. 5, pp. 97–137.
- [43] Shinji Matsuo. "Heterogeneously integrated III–V photonic devices on Si". *Semiconductors and Semimetals*. Ed. by Sebastian Lourdudoss, John E. Bowers, and Chennupati Jagadish. 1st ed. Vol. 101. Elsevier Inc., 2019. Chap. 2, pp. 43–89.
- [44] Shinji Matsuo et al. "High-speed ultracompact buried heterostructure photonic-crystal laser with 13 fJ of energy consumed per bit transmitted". *Nature Photonics* 4.9 (2010), pp. 648–654.
- [45] Shinji Matsuo et al. "20-Gbit/s directly modulated photonic crystal nanocavity laser with ultra-low power consumption". *Optics Express* 19.3 (2011), p. 2242.

- [46] Chin-hui Chen et al. "40-Gb/s directly-modulated photonic crystal lasers under optical injection-locking". *Optics Express* 19.18 (2011), pp. 17669–17676.
- [47] Shinji Matsuo et al. "Room-temperature continuous-wave operation of lateral current injection wavelength-scale embedded active-region photonic-crystal laser". *Optics Express* 20.4 (2012), p. 3773.
- [48] Koji Takeda et al. "Few-fJ/bit data transmissions using directly modulated lambda-scale embedded active region photonic-crystal lasers". *Nature Photonics* 7.7 (2013), pp. 569–575.
- [49] Koji Takeda et al. "Reduction of Cavity Length in λ -Scale Embedded Active-region Photonic Crystal (LEAP) Lasers". *2018 IEEE International Semiconductor Laser Conference (ISLC)*. IEEE, 2018, pp. 1–2.
- [50] Koji Takeda et al. "1-fJ / bit Direct Modulation of Photonic-Crystal Lasers". *2018 European Conference on Optical Communication (ECOC)*. IEEE, 2018, pp. 1–3.
- [51] Koji Takeda et al. "Heterogeneously integrated photonic-crystal lasers on silicon for on/off chip optical interconnects". *Optics Express* 23.2 (2015), p. 702.
- [52] Koji Takeda et al. "Si Nanowire Waveguide Coupled Current-Driven Photonic-Crystal Lasers". *2017 European Conference on Lasers and Electro-Optics and European Quantum Electronics Conference*. Optical Society of America, 2017, CK_9_4.
- [53] Hidetaka Nishi et al. "Low-Operating Energy Heterogeneously Integrated Photonic-Crystal Laser on Si Waveguide". *2018 IEEE International Semiconductor Laser Conference (ISLC)*. IEEE, 2018, pp. 1–2.
- [54] Kohei Ashida et al. "Ultrahigh-Q photonic crystal nanocavities fabricated by CMOS process technologies". *Optics Express* 25.15 (2017), p. 18165.
- [55] Delphin Dodane et al. "Fully embedded photonic crystal cavity with $Q=0.6$ million fabricated within a full-process CMOS multiproject wafer". *Optics Express* 26.16 (2018), p. 20868.

- [56] Kengo Nozaki et al. "Femtofarad optoelectronic integration demonstrating energy-saving signal conversion and nonlinear functions". *Nature Photonics* 13.7 (2019), pp. 454–459.
- [57] John D. Joannopoulos et al. *Photonic crystals: Molding the flow of light*. 2nd ed. Princeton University Press, Oct. 2008.
- [58] Lord Rayleigh Sec. R. S. "XVII. On the maintenance of vibrations by forces of double frequency, and on the propagation of waves through a medium endowed with a periodic structure". *The London, Edinburgh, and Dublin Philosophical Magazine and Journal of Science* 24.147 (1887), pp. 145–159.
- [59] R.W. Wood. "XLII. On a remarkable case of uneven distribution of light in a diffraction grating spectrum". *The London, Edinburgh, and Dublin Philosophical Magazine and Journal of Science* 4.21 (1902), pp. 396–402.
- [60] Eli Yablonovitch. "Inhibited spontaneous emission in solid-state physics and electronics". *Physical Review Letters* 58.20 (May 1987), pp. 2059–2062.
- [61] Sajeev John. "Strong localization of photons in certain disordered dielectric superlattices". *Physical Review Letters* 58.23 (1987), pp. 2486–2489.
- [62] V. P. Bykov. "Spontaneous Emission From a Medium With a Band Spectrum." *Sov J Quantum Electron* 4.7 (1975), pp. 861–871.
- [63] Richard M. De La Rue and Christian Seassal. "Photonic crystal devices: Some basics and selected topics". *Laser and Photonics Reviews* 6.4 (2012), pp. 564–597.
- [64] E. Yablonovitch. "Photonic crystals: Semiconductors of light". *Scientific American* 285.6 (2001), pp. 34–41.
- [65] Pete Vukusic and J Roy Sambles. "Photonic structures in biology". *Nature* 424 (2003), pp. 852–855.
- [66] Pete Vukusic. "Natural photonics". *Phys. World* 17.2 (2004), p. 35.
- [67] Jean Pol Vigneron and Priscilla Simonis. "Natural photonic crystals". *Physica B: Condensed Matter* 407.20 (2012), pp. 4032–4036.

- [68] Jian Zi et al. "Coloration strategies in peacock feathers". *Proceedings of the National Academy of Sciences* 100.22 (2003), pp. 12576–12578.
- [69] Jean Pol Vigneron et al. "Structural origin of the colored reflections from the black-billed magpie feathers". *Physical Review E* 73.2 (2006), p. 021914.
- [70] Robert W Corkery and Eric C Tyrode. "On the colour of wing scales in butterflies : iridescence and preferred orientation of single gyroid photonic crystals". *Interface Focus* 7 (2017).
- [71] Maria E Mcnamara et al. "Cryptic iridescence in a fossil weevil generated by single diamond photonic crystals". *J. R. Soc. Interface* 11.100 (2014), p. 20140736.
- [72] Jérémie Teyssier et al. "Photonic crystals cause active colour change in chameleons". *Nature Communications* 6 (2015), p. 6368.
- [73] Masayuki Fujita et al. "Simultaneous Inhibition and Redistribution of Spontaneous Emission from Perovskite Photonic Crystals". *Science* 308.5726 (May 2005), pp. 1296–1298.
- [74] S. Olivier et al. "Mini-stopbands of a one-dimensional system: The channel waveguide in a two-dimensional photonic crystal". *Physical Review B* 63.11 (2001), pp. 1–4.
- [75] M. Notomi et al. "Extremely large group-velocity dispersion of line-defect waveguides in photonic crystal slabs". *Physical Review Letters* 87.25 (Dec. 2001), pp. 253902–253902–4.
- [76] Takuya Tamura et al. "Silica-Clad Silicon Photonic Crystal Waveguides for Wideband Dispersion-Free Slow Light". *Journal of Light-wave Technology* 33.14 (2015), pp. 3034–3040.
- [77] Weiqi Xue et al. "Threshold Characteristics of Slow-Light Photonic Crystal Lasers". *Physical Review Letters* 116.6 (2016), pp. 1–5.
- [78] M Okano et al. "Analysis of two-dimensional photonic crystal L-type cavities with low-refractive-index material cladding". *Journal of Optics* 12.7 (July 2010), p. 075101.

- [79] Yoshihiro Akahane et al. "High-Q photonic nanocavity in a two-dimensional photonic crystal". *Nature* 425.6961 (2003), pp. 944–947.
- [80] E. Kuramochi et al. "Systematic hole-shifting of L-type nanocavity with an ultrahigh Q factor". *Optics Letters* 39.19 (2014), pp. 5780–3.
- [81] Yoshinori Tanaka, Takashi Asano, and Susumu Noda. "Design of Photonic Crystal Nanocavity With Q-Factor of $\sim 10^9$ ". *Journal of Lightwave Technology* 26.11 (June 2008), pp. 1532–1539.
- [82] Y. Lai et al. "Genetically designed L3 photonic crystal nanocavities with measured quality factor exceeding one million". *Applied Physics Letters* 104.24 (2014), pp. 1–5.
- [83] Tatsuya Nakamura et al. "Improvement in the quality factors for photonic crystal nanocavities via visualization of the leaky components". *Optics Express* 24.9 (2016), p. 9541.
- [84] Kenichi Maeno et al. "Analysis of high-Q photonic crystal L3 nanocavities designed by visualization of the leaky components". *Optics Express* 25.1 (Jan. 2017), p. 367.
- [85] Bong Shik Song et al. "Ultra-high-Q photonic double-heterostructure nanocavity". *Nature Materials* 4.3 (Feb. 2005), pp. 207–210.
- [86] Snjezana Tomljenovic-Hanic et al. "High-Q cavities in photosensitive photonic crystals". *Optics Letters* 32.5 (Mar. 2007), p. 542.
- [87] Bong-Shik Song et al. "Ultrahigh-Q nanocavity based on photonic-crystal double heterostructure". *2005 Quantum Electronics and Laser Science Conference*. Vol. 1. May 2005, pp. 407–409.
- [88] Yasushi Takahashi et al. "High-Q nanocavity with a 2-ns photon lifetime". *Optics Express* 15.25 (2007), p. 17206.
- [89] Masaya Notomi and Hideaki Taniyama. "On-demand ultrahigh-Q cavity formation and photon pinning via dynamic waveguide tuning". *Optics Express* 16.23 (2008), p. 18657.
- [90] J. Mørk, Y. Chen, and M. Heuck. "Photonic crystal fano laser: Terahertz modulation and ultrashort pulse generation". *Physical Review Letters* 113.16 (Oct. 2014), pp. 1–5.

- [91] Yi Yu et al. "Fano resonance control in a photonic crystal structure and its application to ultrafast switching". *Applied Physics Letters* 105.6 (Aug. 2014).
- [92] Andreas Dyhl Østerkryger et al. "Spectral symmetry of Fano resonances in a waveguide coupled to a microcavity". *Optics Letters* 41.9 (May 2016), p. 2065.
- [93] Thorsten S. Rasmussen, Yi Yu, and Jesper Mørk. "Modes, stability, and small-signal response of photonic crystal Fano lasers". *Optics Express* 26.13 (June 2018), p. 16365.
- [94] Aref Rasoulzadeh Zali et al. "Small and large signal analysis of photonic crystal fano laser". *Journal of Lightwave Technology* 36.23 (2018), pp. 5611–5616.
- [95] Yi Yu et al. "Demonstration of a self-pulsing photonic crystal Fano laser". *Nature Photonics* 11.2 (Feb. 2017), pp. 81–84.
- [96] Thorsten S. Rasmussen, Yi Yu, and Jesper Mørk. "Theory of Self-pulsing in Photonic Crystal Fano Lasers". *Laser & Photonics Reviews* 11.5 (Sept. 2017), p. 1700089.
- [97] Jesper Mørk et al. "Semiconductor Fano Lasers". *IEEE Journal of Selected Topics in Quantum Electronics* 25.6 (Nov. 2019).
- [98] S. J. Lee et al. "Density of states of quantum dots and crossover from 3D to Q0D electron gas". *Semiconductor Science and Technology* 7.8 (1992), pp. 1072–1079.
- [99] Yasuhiko Arakawa, Takahiro Nakamura, and Jinkwan Kwoen. "Quantum dot lasers for silicon photonics". *Semiconductors and Semimetals*. Ed. by Sebastian Lourdudoss, John E. Bowers, and Chennupati Jagadish. 1st ed. Vol. 101. Elsevier Inc., 2019. Chap. 3, pp. 91–138.
- [100] Takahiro Nakamura et al. "Fingertip-Size Optical Module, "Optical I/O Core", and Its Application in FPGA". *IEICE Transactions on Electronics* E102.C.4 (Apr. 2019), pp. 333–339.
- [101] Weiqi Xue et al. "Thermal analysis of line-defect photonic crystal lasers". *Optics Express* 23.14 (2015), p. 18277.
- [102] Aurimas Sakanas. "Buried Heterostructure Photonic Crystal Lasers". PhD thesis. Technical University of Denmark, 2019.

- [103] Mark A. McCord and Michael J. Rooks. "Electron Beam Lithography". *Handbook of Microlithography, Micromachining, and Microfabrication. Volume 1: Microlithography*. Ed. by P. Rai-Choudhury. SPIE PRESS, Mar. 1997. Chap. 2, pp. 142–249.
- [104] S. A. Rishton. "Point exposure distribution measurements for proximity correction in electron beam lithography on a sub-100 nm scale". *Journal of Vacuum Science & Technology B: Microelectronics and Nanometer Structures* 5.1 (1987), p. 135.
- [105] D. Schefzyk, D. E.F. Biesinger, and D. A. Wharam. "Extraction of the point-spread function in electron-beam lithography using a cross geometry". *Microelectronic Engineering* 87.5-8 (2010), pp. 1091–1094.
- [106] Yuki Atsumi et al. "Loss reduction of Si optical waveguides by beam step-size fracturing technique in electron beam lithography". *Japanese Journal of Applied Physics* 53.6S (2014), 06JB04.
- [107] S. Hughes et al. "Extrinsic Optical Scattering Loss in Photonic Crystal Waveguides: Role of Fabrication Disorder and Photon Group Velocity". *Physical Review Letters* 94.3 (Jan. 2005), p. 033903.
- [108] Takashi Asano, Bong-shik Song, and Susumu Noda. "Analysis of the experimental Q factors (~1 million) of photonic crystal nanocavities". *Optics Express* 14.5 (2006), pp. 1996–2002.
- [109] Yoshinori Tanaka et al. "Theoretical investigation of a two-dimensional photonic crystal slab with truncated cone air holes". *Applied Physics Letters* 82.11 (2003), pp. 1661–1663.
- [110] Momchil Minkov et al. "Statistics of the disorder-induced losses of high-Q photonic crystal cavities". *Optics Express* 21.23 (2013), p. 28233.
- [111] Larry A. Coldren, Scott W. Corzine, and Milan L. Mašanović. *Diode Lasers and Photonic Integrated Circuits*. John Wiley & Sons, Inc., Mar. 2012.
- [112] Peter Blood. "On the dimensionality of optical absorption, gain, and recombination in quantum-confined structures". *IEEE Journal of Quantum Electronics* 36.3 (Mar. 2000), pp. 354–362.

- [113] Masahiro Nomura et al. "Highly efficient optical pumping of photonic crystal nanocavity lasers using cavity resonant excitation". *Applied Physics Letters* 89.16 (2006).
- [114] Yasutomo Ota et al. "Thresholdless quantum dot nanolaser". *Optics Express* 25.17 (2017), p. 19981.
- [115] D. M. Kane and Joshua P. Toomey. "Precision Threshold Current Measurement for Semiconductor Lasers Based on Relaxation Oscillation Frequency". *Journal of Lightwave Technology*, Vol. 27, Issue 15, pp. 2949-2952 27.15 (Aug. 2009), pp. 2949–2952.
- [116] Ryan L. Woodham. *ReliaTest L/I Threshold Calculations. Understanding the First and Second Derivative Threshold Algorithms*. 2006. (Visited on 01/15/2020).
- [117] Zijun Chen et al. "Intensity noise and bandwidth analysis of nanolasers via optical injection". *Opt. Express* 27.6 (2019), pp. 8186–8194.
- [118] Molly Piels, Idelfonso Tafur Monroy, and Darko Zibar. "Laser characterization with advanced digital signal processing". *Proc. SPIE 9388, Optical Metro Networks and Short-Haul Systems VII*. February 2015. 2015, p. 938809.
- [119] Darko Zibar, Christian Schaeffer, and Jesper Mork. "Learning of Laser Dynamics using Bayesian Inference". *Conference on Lasers and Electro-Optics*. 2018, paper STh1C.1.
- [120] G. Brajato and D. Zibar. "Joint Learning of Laser Relative Intensity and Frequency Noise from Single Experiment and Single Detected Quadrature". *2018 European Conference on Optical Communication (ECOC), Rome*. IEEE, 2018, pp. 1–3.
- [121] Murray W. McCutcheon et al. "Resonant scattering and second-harmonic spectroscopy of planar photonic crystal microcavities". *Applied Physics Letters* 87.22 (2005), pp. 1–3.
- [122] M. Galli et al. "Light scattering and Fano resonances in high-Q photonic crystal nanocavities". *Applied Physics Letters* 94.7 (2009), p. 071101.

- [123] Simone L Portalupi et al. "Planar photonic crystal cavities with far-field optimization for high coupling efficiency and quality factor". *Optics Express* 18.15 (2010), p. 16064.
- [124] S. L. Portalupi et al. "Deliberate versus intrinsic disorder in photonic crystal nanocavities investigated by resonant light scattering". *Physical Review B - Condensed Matter and Materials Physics* 84.4 (2011), pp. 1–9.
- [125] G. D. Pettit and W. J. Turner. "Refractive index of InP". *Journal of Applied Physics* 36.6 (1965), p. 2081.
- [126] Jakob Rosenkrantz de Lasson et al. "Benchmarking five numerical simulation techniques for computing resonance wavelengths and quality factors in photonic crystal membrane line defect cavities". *Optics Express* 26.9 (Apr. 2018), p. 11366.
- [127] Akihiro Fushimi et al. "Fast calculation of the quality factor for two-dimensional photonic crystal slab nanocavities". *Optics Express* 22.19 (2014), p. 23349.
- [128] Kristoffer S. Mathiesen et al. "Optimization of the threshold pump power of a photonic crystal nanolaser: experiment and theory". SPIE-Intl Soc Optical Eng, Apr. 2019, p. 15.
- [129] Philippe Lalanne, Christophe Sauvan, and Jean Paul Hugonin. "Photon confinement in photonic crystal nanocavities". *Laser and Photonics Reviews* 2.6 (2008), pp. 514–526.
- [130] Stephen A. Moore et al. "Reduced surface sidewall recombination and diffusion in quantum-dot lasers". *IEEE Photonics Technology Letters* 18.17 (Sept. 2006), pp. 1861–1863.
- [131] Sara Ek et al. "Slow-light-enhanced gain in active photonic crystal waveguides". *Nature Communications* 5.May 2016 (2014), pp. 1–8.
- [132] W. W. Chow and H. C. Schneider. "Theory of laser gain in InGaN quantum dots". *Applied Physics Letters* 81.14 (2002), pp. 2566–2568.
- [133] Zhihua Huang et al. "Optical Gain and Lasing Properties of InP/AlGaInP Quantum-Dot Laser Diode Emitting at 660 nm". *IEEE Journal of Quantum Electronics* 55.2 (2019), pp. 2–8.

- [134] Justin C. Norman et al. "Perspective: The future of quantum dot photonic integrated circuits". *APL Photonics* 3.3 (2018).
- [135] Yating Wan, Justin Norman, and John Bowers. "Quantum dot microcavity lasers on silicon substrates". *Semiconductors and Semimetals*. Ed. by Sebastian Lourdudoss, John E. Bowers, and Chennupati Jagadish. 1st ed. Vol. 101. Elsevier Inc., 2019. Chap. 9, pp. 305–354.
- [136] Eiichi Kuramochi et al. "Room temperature continuous-wave nanolaser diode utilized by ultrahigh-Q few-cell photonic crystal nanocavities". *Optics Express* 26.20 (2018), p. 26598.
- [137] Matthew Pelton and Yoshihisa Yamamoto. "Ultralow threshold laser using a single quantum dot and a microsphere cavity". *Physical Review A - Atomic, Molecular, and Optical Physics* 59.3 (Mar. 1999), pp. 2418–2421.
- [138] Vadim A. Markel. "Introduction to the Maxwell Garnett approximation: tutorial". *Journal of the Optical Society of America A* 33.7 (July 2016), p. 1244.
- [139] Andrei Andryieuski, Andrei V. Lavrinenko, and Sergei V. Zhukovsky. "Anomalous effective medium approximation breakdown in deeply subwavelength all-dielectric photonic multilayers". *Nanotechnology* 26.18 (May 2015), pp. 1–11.
- [140] Shousaku Kubo, Daisuke Mori, and Toshihiko Baba. "Low-group-velocity and low-dispersion slow light in photonic crystal waveguides". *Optics Letters* 32.20 (Oct. 2007), p. 2981.
- [141] Toshihiko Baba. *Slow light in photonic crystals*. Aug. 2008.
- [142] Lars H. Frandsen et al. "Photonic crystal waveguides with semi-slow light and tailored dispersion properties". *Opt. Express* 14.20 (2006), pp. 9444–9450.
- [143] Thomas F. Krauss. "Why do we need slow light?" *Nature Photonics* 2.8 (2008), pp. 448–450.
- [144] Bong Shik Song et al. "Transmission and reflection characteristics of in-plane hetero-photonic crystals". *Applied Physics Letters* 85.20 (Nov. 2004), pp. 4591–4593.

- [145] P. D. García et al. "Two mechanisms of disorder-induced localization in photonic-crystal waveguides". *Physical Review B* 96.14 (Oct. 2017).
- [146] Juan Pablo Vasco and Stephen Hughes. "Anderson Localization in Disordered LN Photonic Crystal Slab Cavities". *ACS Photonics* 5.4 (2018), pp. 1262–1272.
- [147] Ugo Fano. "Effects of configuration interaction on intensities and phase shifts". *Physical Review* 124.6 (1961), pp. 1866–1878.
- [148] Dagmawi Alemayehu Bekele. "Photonic crystal Fano structures for all-optical signal processing". PhD thesis. Technical University of Denmark, 2018.
- [149] D von der Linde. "Characterization of the Noise in Continuously Operating Mode-Locked Lasers". *Applied Physics B* 39 (1986), pp. 201–217.
- [150] Shinji Matsuo and Koji Takeda. " λ -scale embedded active region photonic crystal (LEAP) lasers for optical interconnects". *Photonics* 6.3 (2019).
- [151] Yi Yu. "Photonic Crystal Nanocavity Devices for Nonlinear Signal Processing". PhD thesis. Technical University of Denmark, 2014.